Image processing techniques in nuclear medicine

Thesis

Image Processing Techniques

in

Nuclear Medicine

by D R Whalley B.Sc., M.Sc.

Submitted for the Degree of Doctor of Philosophy

in the Physics Discipline

of the Open University

September, 1989.

Volume 1 of 2

Contents

Table of illustrations

The illustrations in the thesis are numbered consecutively by Chapter. Line illustrations are bound with the text in Volume 1 of the thesis on the pages indicated below. Photographic plates are identified by the letter P preceding the Chapter number, i.e. figure P2.9 is the ninth illustration in Chapter 2 and is a photographic plate. The plates are bound separately and form Volume 2 of the thesis.

Line illustrations (Volume 1)

Plates (Volume 2)

Acknowledgements

I would like to acknowledge the assistance, advice and encouragement given to me throughout this work by my supervisors, Dr JG Hardy and Dr S Freake.

I would also like to thank the following staff of the Medical Physics Department at Queen's Medical Centre, for their invaluable assistance with the patient studies in this work: Mr K Blackband, Miss K Craik, Dr M Frier, Mrs L Iwanejko, Miss A Jarrett, Mr S Lawes, Miss M Oxley and the Radiodiagnosis Section Head, Dr AC Perkins.

I am grateful for the kind assistance with the clinical aspects of the work which was given by Mr KC Ballantyne, Mr RM Charnley, Dr K Priestley, Dr RG Wilcox and Dr ML Wastie. Mrs J Howard kindly provided the left ventriculographic ejection fractions and, together with the other technicians of the Cardiac Department, assisted in the performance of the exercise tests.

Thanks are also due to Mr PH Riley for his advice on statistical methods and to Miss C Parr for her assistance with word-processing during the drafting of this thesis.

Finally, I would like to acknowledge the unfailing support given by Hilary, my wife, and my children, James and Peter.

Abstract

The application of image processing techniques to radionuclide images acquired on a gamma camera - computer system has been investigated.

Hepatic perfusion imaging studies with $^{99}Tc^{m}$-tin colloid were performed in patients with primary colorectal carcinoma. The hepatic perfusion index performed poorly in the detection of those patients with occult or overt hepatic metastastes, as did mean transit times of liver colloid flow derived from deconvolution analysis. A discriminant function was developed which separated those patients with occult metastases from those without liver disease.

A fully automatic algorithm to derive a left ventricular edge from each frame of an ECG gated cardiac blood pool study was developed and validated in patient studies. Left ventricular ejection fractions calculated from count rates within the edge were reproducible and correlated well with ejection fractions derived from the same images by a manual technique, and with ejection fractions derived from left ventricular cineangiography.

Studies were performed in patients to evaluate the effectiveness of tomographic imaging of the myocardial perfusion imaging agent $^{99}Tc^{m}$-tBIN for detection of ischaemic heart disease. Tomographic reconstructions in the planes of the axes of the left ventricle gave better results than transaxial reconstructions or planar imaging. Choice of the optimum reconstruction filter for use in tomography using $^{99}Tc^{m}$-tBIN was examined by means of patient and phantom studies. These showed that more accurate diagnoses and better reconstructions were obtained with smoothing filters than by the use of sharp reconstruction filters.

This work shows that optimum image processing techniques must be established to attain the best possible results with new radiopharmaceuticals for nuclear medicine investigations.

1. Introduction

Almost since its inception, nuclear medicine has been concerned with the images that are formed to show the distributions of radioactive materials in-vivo. Ansell and Rotblat (1948) obtained isocount contour plots of the thyroid by manually scanning over a series of measurement points with a spacing of 1cm using a Geiger-Müller detector. This technique was refined by replacing the G-M tube with a collimated scintillation detector and arranging an automated scanning mechanism. Such devices, called rectilinear scanners (Cassen et al, 1951), were the mainstay of nuclear medicine imaging for many years, and remained in routine use in some centres into the present decade.

Rectilinear scanners had poor sensitivity and poor spatial resolution, no better than 13-15 mm in the focal plane of the collimator. The poor sensitivity of the device was inherent in the use of a small (12.5 cm diameter, 5cm thick) scintillation detector crystal with mechanical scanning. Fifteen to twenty minutes was required to scan a patient and acquire a useful number of events in the final image (e.g. 3×10^5 counts in a liver scan using 80 MBq $^{99}Tc^m$-labelled colloid). This meant that rectilinear scanners were incapable of recording rapidly changing activity distributions. Image processing techniques to reduce noise and improve resolution were applied to computer recorded rectilinear scanner images (Brown et al, 1973) and these techniques are now also applied to images from gamma cameras (see Chapter 2).

Gamma cameras, first described by Anger (1958), use a single, large (typically 40 cm diameter, 12.5 mm thick), collimated scintillation crystal which enables most organs to be recorded rapidly in a single image. The liver scan mentioned above could be recorded in less than one minute using a modern gamma camera. This means that, at some penalty in terms of counts in each recorded image, very rapidly changing activity distributions may be recorded. Examples of such distributions

are the flow of tracer in the blood along arteries and the rapid clearance of tracer from the kidneys. The spatial resolution of the gamma camera is somewhat better than that of the rectilinear scanner (8-10 mm at a depth of 10 cm in the body) but resolution recovery methods are often used to obtain the best performance from the system. These methods give reasonable results even in images acquired over short periods of time, due to the increased count rates obtained with the gamma camera compared with the rectilinear scanner. However, the use of a thin detector crystal in the gamma camera results in a reduction in counting efficiency at higher gamma ray energies. The optimum energy for gamma camera imaging lies between 100 and 200 keV.

The images described above are two dimensional representations of three dimensional activity distributions. Tomographic slices, showing distributions free from overlapping activity, may be produced from a set of gamma camera images recorded at different angles over a longer period of time (typically 20-30 minutes). These increase the contrast in images of deep sources surrounded by activity, and thus make diagnosis easier.

The object of the work described in this thesis was to investigate a number of processing techniques in different types of nuclear medicine study. Chapter 2 reviews the literature relating to image processing of gamma camera images. Chapters 3 and 4 relate to studies of the liver, with Chapter 3 reviewing the applications of nuclear medicine in diagnosis of liver disease. Chapter 4 describes the development of a discriminant function to identify patients harbouring occult liver metastases from primary colorectal carcinoma. The function uses data acquired from hepatic perfusion imaging using $^{99}Tc^{m}$-tin colloid.

The next four chapters relate to studies of the heart. Chapter 5 describes the heart and cardiac circulation and reviews the literature relating to nuclear medicine imaging of the heart. Chapter 6 describes

a new edge detection algorithm to identify the left ventricular boundary in ECG gated images of the heart for calculation of the left ventricular ejection fraction. Chapters 7 and 8 describe studies using data acquired from patients and from simulation phantoms to find the best reconstruction filter for emission tomography of myocardial perfusion imaging using $^{99}Tc^{m}$-tertiary butyl isonitrile.

2. Gamma camera imaging

The gamma camera was developed by Anger (1958) and is the major imaging device used in nuclear medicine. The purpose of the gamma camera is to produce images representing the in-vivo distributions of gamma ray emitting radionuclides. The theory of operation of the gamma camera, and its performance, has been surveyed in a Topic Group Report of the Hospital Physicists' Association (HPA, 1978) and by Elliott and Short (1981).

2.1 Gamma camera design, theory and performance

The construction of the gamma camera is illustrated in figure 2.1. Gamma rays from a source, S, pass through a collimator and are absorbed by a large, thin thallium-activated sodium iodide crystal (typically 450 mm in diameter, 12.5 mm thick). The light photons emitted by the crystal are detected by an array of photomultiplier tubes which are optically coupled to the transparent rear face of the crystal. The output signals from the photomultiplier tubes are routed to a pulse arithmetic circuit which produces signals which may be displayed on an oscilloscope, or recorded on a computer. The detector head assembly is housed in a protective shield made from lead and steel, which serves as a mechanical framework and as shielding against unwanted radiation.

2.1.1 Collimators

Since gamma rays cannot be focussed, image formation in the gamma camera is achieved by means of absorptive collimation. Only those rays travelling in certain directions can pass through the collimator, reach the detector and be recorded to form an image. Gamma rays travelling in other directions are absorbed by the collimator. Absorptive collimation is inherently inefficient because much of the potentially useful radiation is stopped before reaching the detector; typically only

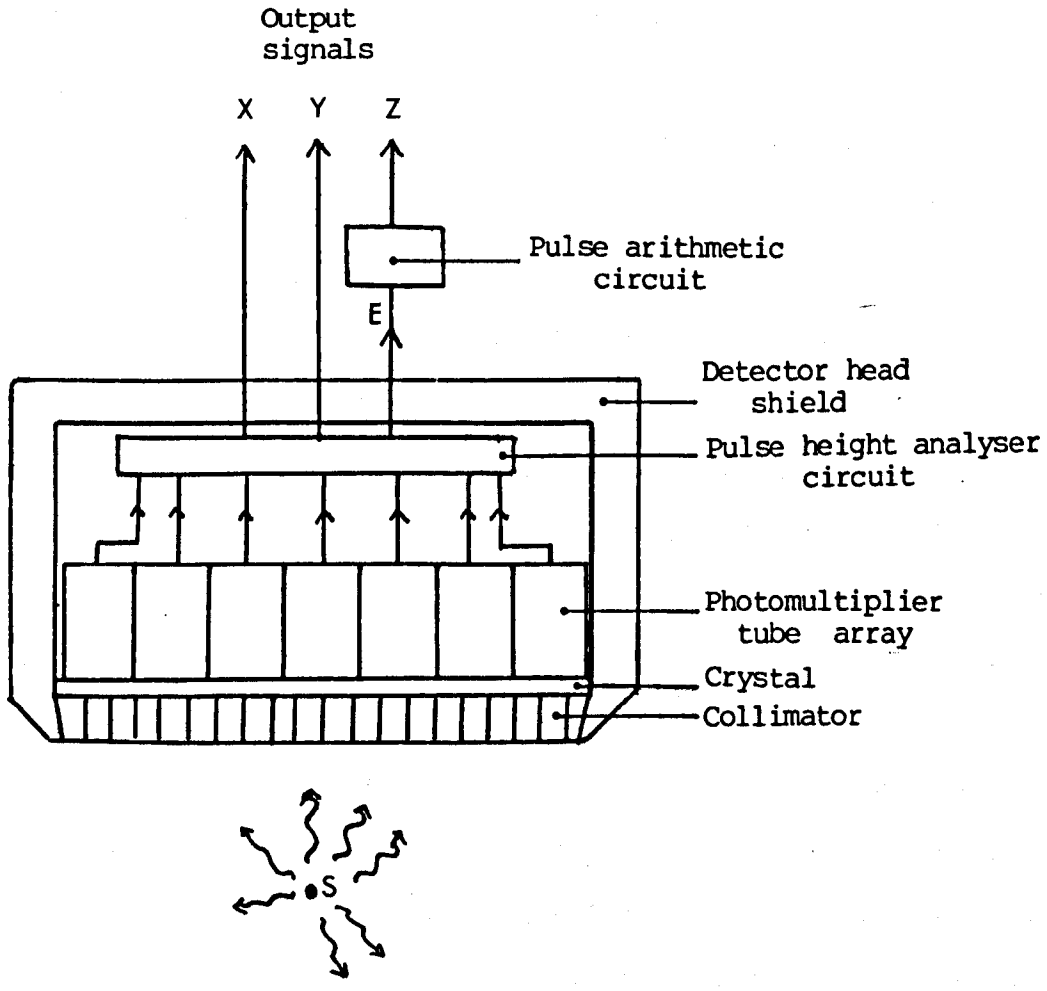

Figure 2.1 Schematic cross section of a gamma camera detector head.

between 0.02% and 2% of the gamma rays striking the collimator face reach the crystal, depending on collimator design and source geometry. This results in a relatively poor information density in nuclear medicine imaging; typically 100-3000 events/cm^2 compared with about 10^6 photon events/mm^2 in X-ray or conventional photographic imaging. There are three main collimator types, the pinhole collimator, the parallel hole collimator and the converging/diverging hole collimator (figure 2.2).

The pinhole collimator consists of a small aperture positioned about 30cm from the crystal face at the apex of a cone of a heavy metal absorber, such as lead or tungsten. Large magnifications of small source distributions can be achieved, although the images from distributed sources are distorted since sources at greater depths produce smaller images. In general, pinhole collimators give higher spatial resolution than other types of collimator at the expense of poor sensitivity. A set of pinhole inserts of differing diameters is usually available; larger pinholes give higher sensitivity at the expense of poorer spatial resolution.

The parallel hole collimator consists of an array of parallel holes, normal to the crystal face, usually drilled or cast in lead, or shaped from lead foils. This array of holes permits the preferential detection of gamma rays travelling in directions approximately normal to the crystal face. The thickness of lead between the holes (septa) is chosen so that some specified fraction (normally 95%) of the gamma radiation of a particular energy is absorbed across the shortest absorber path length. This gamma ray energy is, therefore, the highest normally recommended for use with the collimator.

The converging hole collimator has an array of holes which converge to a point 40 to 50 cm in front of the collimator. Source distributions between the the collimator and the convergence point project a magnified

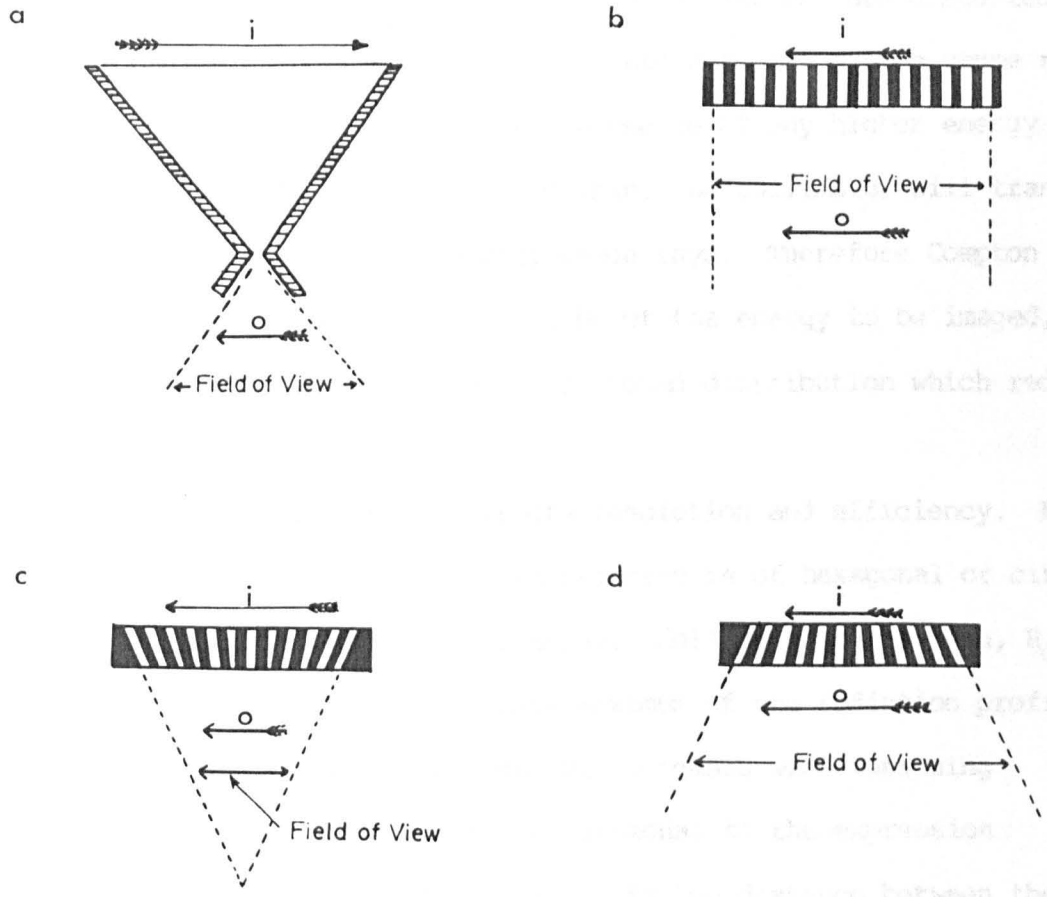

Figure 2.2 Schematic cross sections of collimators. The source distribution o produces an image distribution i in each case. **a:** Pinhole collimator. **b:** Parallel hole collimator. **c:** Converging hole collimator. **d:** Diverging hole collimator

image on the crystal face. The diverging hole collimator has an array of holes which diverge from a point 40 to 50 cm behind the collimator, producing a minified image. The value of the converging and diverging hole collimators lies in the ability to image small organs using large field of view detectors (40 cm) and large organs with small field of view detectors (25 cm) by appropriate choice of collimation. As with the pinhole collimator, images of distributed sources are distorted.

The choice of collimator is determined not only by the gamma ray energy to be imaged, but also by the presence of any higher energy gamma ray emissions. If the septa are too thin, the collimator will transmit a large proportion of higher energy gamma rays. Therefore Compton scattered events, some of which will be of the energy to be imaged, will be produced and recorded giving a background distribution which reduces image contrast.

Collimator hole geometry affects resolution and efficiency. For a parallel hole collimator the normal geometry is of hexagonal or circular holes in a close packed hexagonal array. Collimator resolution, R_c, may be defined as the full width at half maximum of the radiation profile from a line source ($FWHM_1$) and thus R_c increases with worsening resolution. It is approximately proportional to the expression $d(l+b)/l$, where l is the hole length, b is the distance between the source and the collimator entry face and d is the hole diameter (diameter of inscribed circle for hexagonal holes). Collimator efficiency is approximately proportional to $(d/l)^2$, since this quantity is related to the fraction of gamma rays that will reach the crystal. Therefore long, narrow holes give good resolution at the expense of low efficiency. Typically, collimator resolution, for a parallel hole collimator designed for use with the 140 keV emission of technetium-99m, lies in the range 4 to 9 mm, depending on the chosen collimator efficiency.

2.1.2 The crystal

All commercially available Anger-type gamma cameras use thallium doped sodium iodide (NaI(Tl)) as the crystal. The advantages of this material are its high attenuation coefficent and its good light output. For a 12.5 mm thick crystal, conversion efficiency of absorbed energy into light photons is about 90% for 100 keV gamma radiation, dropping to 15% at 511 keV. The disadvantages are, first, NaI(Tl) is hygroscopic and must be hermetically encapsulated and, secondly, it has a high coefficient of thermal expansivity and is fragile and therefore needs to kept in a controlled environment to avoid fracturing.

Only those events within a specified energy range that includes the photopeak are recorded, as gamma photons of lower energy are the result of scattering and thus degrade the image. Crystal thickness affects detection efficiency of incident gamma rays and the light collection characteristics of the photomultiplier tube array. Increasing thickness improves detection efficiency but reduces positional accuracy.

Source distributions containing sharp edges or point objects produce blurred rather than sharply defined images. Part of the blurring is due to the characteristics of the collimator and part arises in the detector and electronics.

The primary limitation on the intrinsic spatial resolution (R_i) of the detector and electronics is the statistical nature of the photon flux on the photomultiplier tubes. The number of photons recorded by a single photomultiplier tube from scintillation events occurring at a particular crystal location follows a Poisson distribution. R_i can be specified as the full width at half maximum of the profile from an image of a line source ($FWHM_l$).

With increasing crystal thickness R_i increases, due to increased spread of light before it reaches the photomultiplier tubes. This

results in the collection of fewer photons per photomultiplier tube and therefore larger statistical fluctuations. R_i also increases with decreasing gamma ray energy, since fewer light photons are produced per event, but decreases with increased light collection and detection efficency of scintillation light.

These factors combine to produce minimum values of R_i for gamma ray energies between 100 and 200 keV. Typical values of R_i in this energy range are 4.5 mm for a 12.5 mm thick crystal, 4 mm for a 9.5 mm thick crystal. Crystal thicknesses of 12.5 mm are most commonly used, but 9.5 mm thick crystals can be used when spatial resolution is considered more important than detection efficiency.

2.1.3 Photomultiplier tubes

In most gamma camera designs, the photomultiplier tubes are placed in a close packed hexagonal array to collect as much light as possible. The tubes are normally optically coupled with silicone fluid or grease to the back plate of the crystal. The faces of the photomultiplier tubes may be round or hexagonal. Modern 40 cm circular field of view cameras normally use 61 or 75 photomultiplier tubes of 50 mm diameter.

2.1.4 Pulse arithmetic

For each gamma ray interaction in the crystal the pulse from each photomultiplier tube contains information on the location and gamma energy of that interaction. Pulse arithmetic circuits comprise electronic analogue mixing circuits which convert the photomultiplier tube outputs into electrical pulse carrying information on the positional coordinates and energy of each scintillation event. The X and Y coordinate voltage pulses are derived as

$$V_x = \sum_i V_i \cdot w_{xi} \quad \text{and} \quad V_y = \sum_i V_i \cdot w_{yi},$$

where V_i is the output of photomultiplier tube i and w_{xi}, w_{yi} are

weighting factors for photomultiplier tube i in the X and Y directions respectively. The weighting factors are chosen to make X and Y independent and to give a linear relationship between voltage and distance in each direction. A sum pulse, E, is generated as

$$E = \sum_i V_i .$$

This pulse, which is proportional to the energy of the interacting gamma photon, is used by the discriminator circuits to determine whether the event shall be recorded in the image. Generally, when an energy pulse falls within a selected range (the analyzer window) a logic signal, the Z pulse, is generated.

It is apparent that the coordinate voltages are energy dependant since the V_i are proportional to incident photon energy. Therefore, the outputs are modified by dividing by the energy signal, E. The use of such signals makes possible the simultaneous imaging of multiple gamma ray energies.

The energy resolution of a gamma camera is expressed as the full width at half maximum of the photopeak of the 140 keV emission of technetium-99m. Typical values for modern gamma cameras range from 10 to 13% at this energy, which compares well with a standard 50mm NaI(Tl) crystal and single photomultiplier tube. Selection of the window for the generation of the Z pulse is a compromise between spatial resolution and sensitivity. If a narrow window is selected then fewer counts are accepted into the final image, but a wider window includes more scattered radiation with degraded positional information. Imaging is normally performed with a window setting in the range 15-25% of photopeak energy.

2.1.5 Image recording

Two basic methods of recording the images exist. The first is to output the images to a cathode ray tube (CRT). To achieve this the X

and Y coordinate voltages are continuously applied to the X and Y deflection plates of a CRT. Each pair of pulses, V_x and V_y, causes the electron beam to move to the point on the CRT screen corresponding to the point in the crystal at which the original gamma ray interaction was located. The CRT is unblanked only when a Z pulse is received. By use of an appropriate camera the scintillations of the CRT phosphor may be recorded photographically.

The second method of recording is to digitize the coordinate voltages and to store the images in a computer. The digitization may be performed either within the gamma camera electronics or by analogue to digital conversion in the computer. This will be discussed in Section 2.2.

2.1.6 Performance characteristics

(a) Image linearity

Distortions in the linearity of the image result when the X and Y position signals do not change linearly with displacement of a gamma ray source across the detector face. For example, when a source is moved across the face of a photomultiplier tube from edge to centre, the light collection efficiency rises more rapidly than the distance the source is moved. The result is pincushion distortion in areas lying in front of photomultiplier tubes, and barrel distortion between them. Differences in output gain between photomultiplier tubes also causes nonlinearity.

Nonlinearities, in themselves, rarely interfere with image interpretation but can have a marked effect on image uniformity. In cameras which operate using digitized signals it is possible to store images of line sources from which corrections to incoming positional signals may be made during data acquisition.

(b) Image uniformity

Exposing the detector to uniform radiation flux does not produce a perfectly uniform image. The variations observed are normally of the order of 10% deviations from the mean count rate.

The most important cause of nonuniformity is the image nonlinearity discussed above. This results in mottled image appearance. Variations in photomultiplier tube performance over time also give rise to nonuniformity. Modern gamma cameras use correction circuitry which reduces observed nonuniformity, either by use of correction factors derived from a stored image of a uniform source, or by electronic monitoring of photomultiplier tube gain shifts, with appropriate corrections. The latter method is preferable as it goes some way towards reducing the underlying nonlinearities which cause the nonuniformity. By these means image uniformity may be improved to give deviations from the mean count rate of less than 5%.

(c) System resolution

The overall system resolution, R_S, is that which can be measured in the final images. It is limited by several factors including collimator resolution and intrinsic resolution of the detector and electronics, scattered radiation and collimator septal penetration. In terms of $FWHM_1$ it is given approximately by the square root of the sum of the squares of the collimator and intrinsic resolutions.

(d) System sensitivity

System sensitivity depends on the collimator efficiency and the detector sensitivity and is expressed as observed count rate per unit activity in the source. The collimator used, the source distance, the radionuclide imaged and the analyzer window must be specified. Using a technetium-99m source, system sensitivity is typically around 150 counts

per second per MBq at the entry face of a low energy, general purpose collimator, with a 20% window centred on 140 keV.

2.2 The nuclear medicine computer

The acquisition and storage of gamma camera data by a computer system allows considerable flexibility in further processing of the images. Such flexibility includes the ability to alter the image display (i.e. perceived brightness and contrast levels within the image) as well as quantitation of uptake of the radiopharmaceutical in specific areas of the image.

The capabilities required of the nuclear medicine computer (Goris and Briandet, 1983) are to:

(i) accept and record gamma camera data

(ii) extract information, both qualitative (visual display) and quantitative (numbers, curves etc.)

(iii) perform image enhancement, for better appearance and improved statistical reliability

(iv) isolate data from the organ under study

(v) output the results of the studies.

It should be noted that in many modern gamma cameras digitization of the coordinate voltage signals takes place within the camera itself, and this greatly simplifies the connection of the camera and computer.

2.2.1 Data acquisition

The acquisition process can be of two basic types, list mode or frame mode. In list mode, events are stored as they occur, as a stream of coordinate pairs (X,Y), interrupted by time markers. This gives maximum time and space resolution until processing. The drawback of this mode is the requirement for a large, fast disk. Frame mode is a short cut whereby an image is built up directly in computer memory,

saving disk space and processing time. Either mode can be controlled by an external sychronizing signal to form images related to a physiological process, such as an ECG to image the beating of the heart.

(a) Hardware

The parts of the computer relevant to the acquisition of gamma camera images are the acquisition interface, the central processing unit (CPU) and the disk.

The output of the analogue circuitry of a gamma camera consists of three electrical pulses. Two of these represent, by their voltage level, the X and Y coordinates and the third (Z) is a 'strobe' specifying the time at which X and Y are measured. The X, Y coordinate pairs must be digitized before they can be handled by a computer. This may be performed either by the gamma camera electronics or within the acquisition interface itself. The digitization of the incoming coordinate pairs is accomplished by analog to digital converters (ADCs).

At the other end of the acquisition chain is the magnetic disk, a mass storage device where all data are saved for further processing. Disk performances vary widely from one type to another. Floppy disks (generally 8") are too slow to be used as the sole storage device on a general nuclear medicine computer system but may be useful in small, inexpensive systems with restricted usage requirements (eg. mobile systems for ward use). The amount of data (~640 kbyte) that can be stored on one disk is particularly restricting, corresponding to only about 70 frames of 64*64 word mode data, assuming a 16 bit word length (ie. 2 byte). This is smaller than is required for many dynamic image sequences.

Hard disks are generally faster and larger than floppy disks. A typical useable transfer rate is equivalent to a 64*64 word mode frame every 40 ms. A typical disk capacity is 85 Mb which is equivalent to

over 6000 64*64 word images, assuming that about one third of the disk is occupied by software, records etc.

(b) Acquisition mode (list or frame)

The data needed for the various clinical procedures are of different kinds; bone, liver and lung studies usually require static images, while renal function and cardiac blood pool studies require dynamic series of frames. Spatial resolution is usually more important for static studies than for dynamic studies, whereas the time resolution needed for the latter varies from milliseconds to minutes. In addition dynamic cardiac studies often use an ECG signal to synchronize framing.

To keep the acquisition hardware and software as simple as possible and retain maximum versatility then list mode is the method of choice; an easily implemented hardware design and a single program will perform all studies. The main advantage of list mode is the retention of maximum resolution in both space and time. An 8 bit digitization of X and Y gives a spatial resolution of 256*256, while time markers can be recorded every millisecond. With a high recorded resolution the final image can be adjusted to suit the needs of the study, which is particularly valuable in studies of small organs or in studies of children.

The main reasons why list mode acquisition is not more widely used are both technical and economic. List mode requires a large and fast disk, which is more expensive than the combination of a small, slower disk and more memory (in either the acquisition interface or main memory). While Winchester technology disks are adequate, simpler systems having smaller disks do not have the required speed or capacity. Floppy disks are an order of magnitude slower than hard disks and cannot be used for list mode acquisition. Therefore, most manufacturers, faced with the problem of offering a range of systems with different disk

capabilities, choose to emphasize frame mode acquisition.

Frame mode acquisition is a process by which an image is built up directly, in either main memory or in dedicated acquisition interface memory. This image is stored on the disk when a preset stop condition is reached. Normally a series of memory banks are used to allow acquisition to continue during disk writing. Frame mode acquisition requires the specification of spatial resolution (matrix size) a priori. A compromise between resolution and processing speed must be established. For a 40 cm field of view gamma camera, a 128*128 matrix gives an effective pixel dimension of about 3 mm. Since information theory requires a sampling distance of half the system spatial resolution (typically more than 6 mm) this is acceptable if there are sufficient counts to give a high signal to noise ratio. When the image counts are low (such as in dynamic studies), Poisson noise may necessitate the use of a coarser, 64*64 image matrix in order to increase the statistical reliability of each pixel count. This has the advantage of reducing the time taken to perform any image processing routine by a factor of four.

In summary, list mode, although theoretically the method of choice, is generally viewed as a luxury and used almost exclusively for certain sophisticated cardiac first pass studies or for refined a posteriori framing of gated blood pool studies. Frame mode is used for static and slow to moderately fast dynamic studies (frame times in the range seconds to minutes) in which the frame time can be determined a priori.

2.2.2 Display

In image processing a great deal of the operator interaction and most of the output involves a TV display.

The simplest objects to be displayed on screen are character strings. In contrast to a VDU terminal the characters are positionable

anywhere on screen and, normally, can be of various colours, so that they are associated with specific image features.

Points and vectors can be used to generate on screen any curves, regions of interest, profiles, contours etc. For such graphics to be indistinguishable from continuous line drawn graphics a resolution of 1024*1024 is required, which is very expensive. Most current systems use 256*256 on economic grounds, although 512*512 is becoming more common.

For display of an image frame two factors need to be considered: X,Y resolution as above, and the intensity resolution. In a monochrome display a trained observer can detect intensity differences of 5-10% (on film, resolution is poorer). Thus in a monochrome display more than 32 levels of grey are unnecessary: each frame to be displayed is scaled to a maximum of 31 and each of its elements is represented by a dot the brightness of which is proportional to the scaled value of this element. In practice the relationship between brightness and pixel content is not very linear (totally non-linear if transposed to film), and the eye/brain system is unable to measure absolute brightness levels, or even to recognize the equality of brightness of two zones if they have different surroundings. These problems have two solutions. The first, non-linear scaling is now common in systems which only offer a monochrome display; most systems offer the second solution, pseudo-colour display, as well as non-linear scaling in some cases.

In pseudo-colour, brightness modulation is replaced by hue modulation; each level of intensity is represented by a given colour, arbitrarily assigned to this level of intensity. In order to be easy to read, a colour scale must progress smoothly through tints in a sequence resembling familiar conventions (eg. rainbow scale, heated object scale, four colour geographic scale) or must have some purpose in its discontinuities (eg. display of two images superimposed, identification

of features in functional images). A colour representation is superior to grey-scale only if more levels of intensity can be seen; between 64 and 128 is reasonable. Most modern systems allow the operator to choose from a range of available colour scales.

The display of a single image may only require a quarter or a sixteenth of the screen, depending on its resolution, which permits the simultaneous display of several images or of a mixture of images, curves and text in a 'page' of results. Such screen-splitting can be used to view a sequence of dynamic frames , for example, 16 64*64 frames. But useful as this is, a 'cine' display of a rapid succession of frames gives a much better idea of motion. This is achieved by loading a series of frames in a dedicated memory, which is partitioned in blocks presented successively to the screen.

A TV monitor is the only type of instrument that is capable of producing the required images, because of its ability to represent a large range of intensities or colours. Since such a monitor does not have a memory a 256*256 location image memory is needed to store the images, curves etc. The number of bits per memory location must be at least 6 to support a 64 level display, and more if alphagraphics are displayed as overlays as is normal. Eight bit memory is commonly used and this allows text or cursors to be moved across the image without destroying the data in memory.

Since the images acquired may be of different resolution to the display memory, images must be interpolated or reduced for display. For instance, a 64*64 frame must be interpolated to 128*128 if it is to be displayed occupying one quarter of a 256*256 screen, while a 256*256 image must be reduced, by summing blocks of four cells, if it is to be similarly shown. Interpolation is necessary since the alternative is to display blocks of cells to represent each pixel, which is extremely disturbing to the viewer. However, interpolation acts as a smoothing

function and in frames with poor statistics the interpolation gives noise more 'respectability' by creating intermediate values around it. The display software achieves the required interpolation or reduction on transfer of the images to the memory.

2.2.3 Processing software

Once an acquisition has been performed and the images stored on disk, and possibly archived on magnetic tape, they may be analyzed by the image processing software.

Almost always the organ under study is not the only feature of the acquired data. Generally other tissues and background are seen, so that there is unwanted information superimposed on the useful portion of the image. To isolate the area under study, a region of interest (ROI) is often drawn on the image and used by the processing programs. For example, evaluation of the sum of those counts within the ROI removes the unwanted data from outside the ROI. Measuring the count rate inside a common ROI for a series of dynamic frames results in a series of values that can be presented as a time-activity curve. Such a curve may represent, for example, the renal clearance of a tracer or a ventricular volume function. Other curves, such as count profiles, may be obtained from images. These curves are sets of values of a function of the type:

$$A = f(\text{position}) \quad \text{or} \quad A = f(\text{time});$$

and are not to be confused with geometrical curves such as an isocount contour line, which is the locus of points in an image at a given count level.

The image processing software available on most nuclear medicine computers falls into one of four basic categories; noise reduction, data compression, image enhancement and feature detection. Image processing techniques are discussed more fully in Section 2.4.

2.3 Gamma camera emission tomography

Conventional gamma camera imaging produces images that are two dimensional representations of three dimensional distributions. Tomography is a method for producing images (tomograms) showing the activity distribution in one or more thin slices through an object. This removes the confusion due to superposition of images of radiation sources at different depths within the object and increases image contrast.

In order to produce tomograms, multiple views of the object from different angles are required. These views are called projections and the tomograms are produced by the process of reconstruction of these projections. The greater the number of such projections and greater the range of viewing angles, the better the depiction of the structure of the distribution.

In the absence of gamma ray attenuation, the logical extreme of the concept of projections from multiple angles is to record views from around a 180^{o} angle. However, the object imaged and its surroundings generally attenuate gamma radiation and projections recorded around 360^{o} are required to compensate.

2.3.1 Data acquisition devices

(a) Limited angle techniques

Limited angle tomography is the process of producing tomographic slices from data acquired from projections over less than a 180^{o} viewing angle (Keyes, 1982). All limited angle tomography systems produce images which are not well defined with regard to depth (distance from the imaging device) and therefore there is considerable crosstalk between successive tomograms. Out of focus data from the other planes is never completely removed from the tomograms and thus image contrast and quantitative accuracy are reduced.

The two most widely used methods of limited angle gamma camera tomography employ special collimators; the seven pinhole collimator, and the rotating slant hole collimator. These have been used primarily for thallium-201 myocardial perfusion tomography.

The seven pinhole technique uses a collimator with seven small holes in a hexagonal array (Vogel et al, 1978). The hole size and spacing determine the size and position of the object volume. Each hole produces a projection of the object on a different part of the gamma camera crystal. A single acquisition consisting of seven projection images is recorded and the tomograms are produced by an iterative image shift and add algorithm. Data points from a particular depth plane are made to coincide while those from other depths are dispersed and thus out of focus. The main disadvantages of the technique are caused by the physical limitations imposed by the collimator. The effective viewing angle is limited by the need to keep the seven projections separated on the crystal, but since this angle gets less for deeper parts of the body the effective slice thickness progressively increases with depth. The change in magnification with depth may also cause image distortion. These factors make positioning of the collimator relative to the patient critical and in myocardial imaging only views of the heart with the central pinhole aligned on the long axis of the left ventricle are satisfactory.

The rotating slant hole collimator technique (Shosa et al, 1980; Muellhener, 1971) has many of the features of the seven pinhole system for myocardial imaging while eliminating some of the problems of that approach. Positioning of the collimator is less critical than that of the seven pinhole collimator and there is much less variation of image size, resolution, and effective slice thickness with depth.

There are three forms of the rotating slant hole collimator. The simplest is merely a parallel hole collimator with all the holes

inclined at the same angle (60^{o}) to the face of the collimator. It is mounted on the gamma camera such that it may be rotated about the detector axis during imaging. Projections are formed by rotating the collimator to obtain several (usually 6 to 8) views of the heart without movement of the patient. The other two forms of the collimator have the working area of the collimator divided into either halves or quarters, with the holes in each segment parallel to each other and oriented toward the centre of the collimator (Chang et al, 1980b). The advantage of the multi-segment collimators is the increase in efficiency which results in shorter acquisition times. Reconstruction techniques for rotating slant hole collimators are similar to those used for seven pinhole systems.

(b) Rotating gamma camera tomography

A linear projection profile may be otained from a gamma camera image by considering only the data in a single row of pixels across the image. By rotating the camera around the object projections may be acquired from a number of angular positions, if the axis of rotation is made parallel with the columns of pixels in the images.

A single transverse (transaxial) slice through the object may be reconstructed from these projections by the methods described below (section 2.3.2). Data from many adjacent pixel rows are acquired simultaneously by the gamma camera and, therefore, multiple adjacent transverse slices may be reconstructed.

2.3.2 Reconstruction methods

In rotating gamma camera tomography the objective is to reconstruct a transaxial image of a source distribution from a set of projection profiles acquired at various angles around the distribution. This may be achieved either analytically, by 'filtered back projection' of the

projection data, or by treating the projection data as a set of linear equations which may be solved iteratively (Brooks and Di Chiro, 1976; Williams, 1985)

(a) Filtered back projection

The reconstruction problem is solved as follows. As a first step consider the result of the direct back projection of the projection data from a point source into the transaxial image matrix. In this case, back projection means taking the value of a profile element acquired at a given angle and adding that value to each element along a line at that angle in the matrix (figure 2.3). This is repeated for all profile elements and for each angle. The result is that the back projected values reinforce each other at the location of the source and an approximation of the source distribution is generated. Unfortunately a significant star like 'background' is also generated due to the extra counts entered along each back projection line. Therefore, before back projection, the projection profiles are convolved with a one-dimensional, symmetric digital filter having positive values at the centre and negative values on each side. The result is that the negative values cancel out the positive background everywhere in the image except at the true source location (figure 2.4).

The required filter is derived by consideration of the back projection process. The result of the back projection of a point source is a star like point spread function, $i(x,y)$, with as many spokes as there are projections. As the number of projections tends to infinity then $i(x,y)$ tends to a 'spokeless' spread function, $1/r$, where $r^2=x^2+y^2$. Thus the back projected estimate $b(x,y)$ is given by,

$$b(x,y) = g(x,y) * i(x,y)$$

where $g(x,y)$ is the true object distribution and * denotes the convolution operator. To obtain the object distribution it is therefore

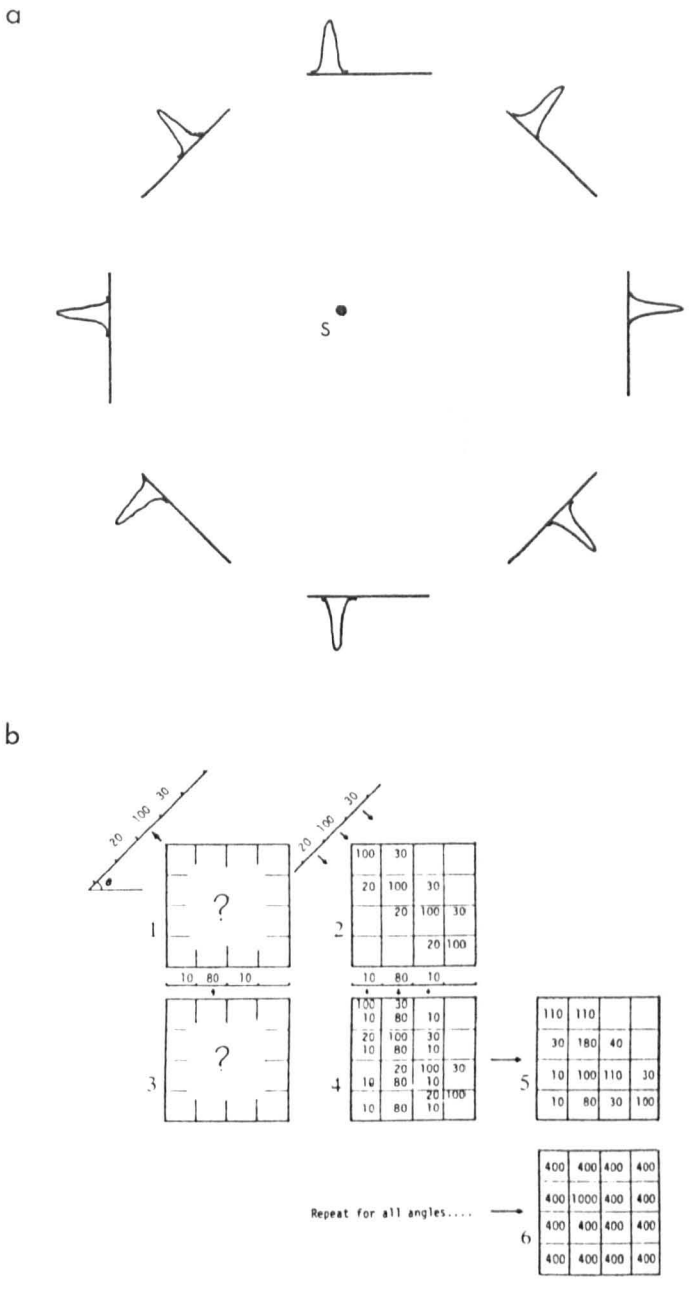

Figure 2.3 Back projection. **a:** Eight projection profiles acquired at equal angles around a source S. **b:** Numerical illustration of the backprojection process. Counts in an observed profile (1) are projected into the matrix (2). The process is repeated for the next profile, at a different angle, (3,4) and the results added (5). After repetition of this process for all data profiles the axial image matrix (6) has a high count at the source location and a 'background' level elsewhere (Williams, 1985).

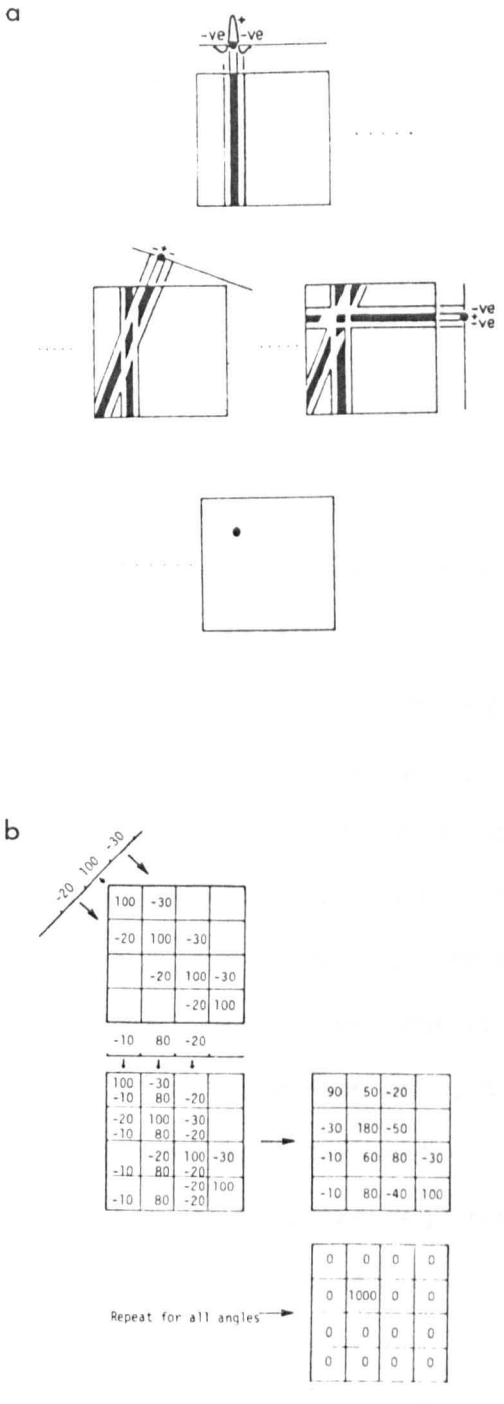

Figure 2.4 Filtered back projection (Williams, 1985). **a:** To remove unwanted 'background' contributions from the final reconstructed axial image matrix each data point has associated negative parts projected into the image. **b:** Numerical demonstration of this process for a small image matrix.

necessary to deconvolve the point spread function from the back projected estimate. Taking the Fourier tranformations of the functions (represented by upper case characters, with spatial frequency arguments x',y') and applying the convolution theorem gives:

$$B(x',y') = G(x',y') \cdot I(x',y')$$

Hence:

$$G(x',y') = B(x',y') \,/\, I(x',y')$$

Now, $i(x,y) = 1/r$ and its Fourier transform, $I(x',y')$, is $1/R$, where R is spatial frequency, that is a ramp function. Therefore:

$$G(x',y') = B(x',y') \cdot R$$

Applying the inverse Fourier transformation (IFT) we obtain:

$$g(x,y) = b(x,y) * k$$

where $k = IFT\{R\}$. Thus the object distribution may be obtained either by multiplying the Fourier transform of the back projected estimate by a ramp function or by convolving the back projected image with k. It is more convenient computationally to use the fact that back projection (ie summation) and convolution are linear operators to permit the reversal of the order of the operations. This means that the convolution operation may be performed in one dimension only, on the projection profiles. Hence, the projection profiles are first <u>filtered</u> then <u>back projected</u>. The one dimensional form of the required symmetrical convolution kernel, $k(na) = IFT\{R\}$, is given by:

$$\begin{aligned} k(na) &= 1/4a^2 && \text{for } n = 0 \\ &= -1/(\pi na)^2 && \text{for } n \text{ odd} \\ &= 0 && \text{for } n \text{ even} \end{aligned}$$

where n is the pixel number and a the pixel dimension (Ramachandran and Lakshminarayanan, 1971).

Considering the ramp in the spatial frequency domain once more, it is clear that the upper limit of meaningful data is given by the Nyquist frequency, 1/2a, and this is chosen as the upper limit of frequency in

the implementation of the filter. The convolution filter is terminated at the point at which the odd terms contribute essentially nothing to the reconstruction. Practically, limitations of noise in the data combined with the tendency of a sharp frequency cut-off to produce oscillations in the data (ringing) force the use of some form of smoothing function, the window, to obtain a smooth transition at the cut-off (figure 2.5).

(b) Iterative methods

If the slice imaged is considered as an array of M pixels, with each pixel, i, containing g(i) counts, and the projection data are considered as a set of N rays p(j) then:

$$p(j) = \sum_{i}^{M} w(i;j).g(i)$$

where the w(i;j) are a set of weighting factors defining the relative contribution of each pixel i to the j.th ray (figure 2.6). Note that most w(i;j) are zero; most pixels contribute nothing to any given ray.

The equation above represents a system of N simultaneous linear equations. If a sufficient number of projections are recorded and the w(i;j) are calculated from geometrical considerations it is possible to solve the equations for g(i) by inversion of the matrix w(i;j). There are three reasons why this is not done (Brooks and DiChiro, 1976).

(i) Noise in the projection data renders the equation system inconsistent and thus impossible to solve exactly.

(ii) The size of the required inversion matrix is very large. For a square 64*64 image matrix covering a circular field of view M is over 3000. The inversion matrix must therefore contain over 9×10^6 elements but this need be calculated only once and may be stored for future use.

(iii) Even when the inversion matrix has been previously stored, iterative procedures to solve the equations are actually faster.

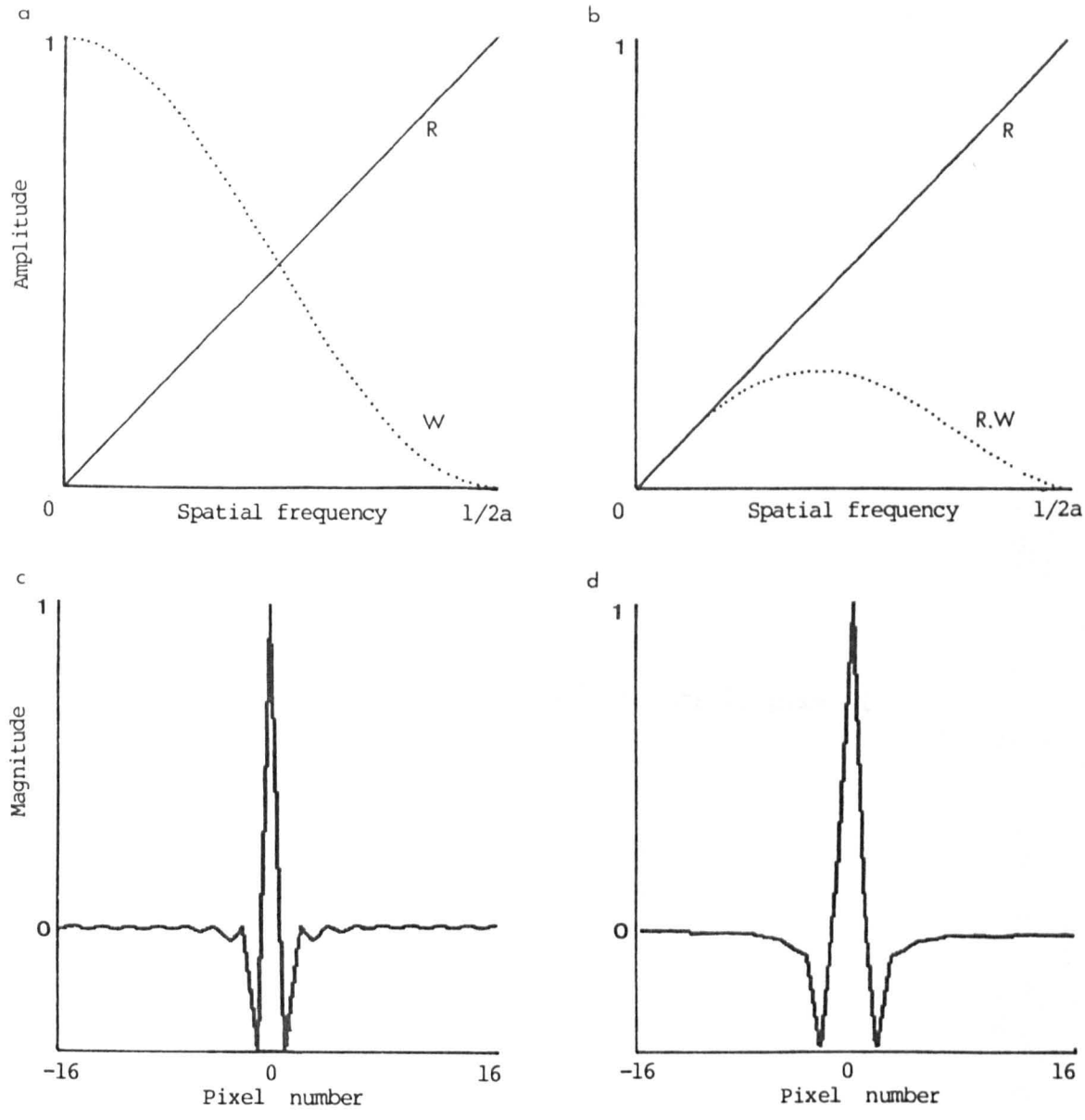

Figure 2.5 Back projection filters. **a:** Frequency domain representations of a ramp function (R) and a typical window function (W). The window shown has the form $W(f) = (1+\cos 2\pi fa)/2$, where f is the spatial frequency. This is the Fourier transform of a 1-2-1 convolution kernel. **b:** Frequency domain representations of a ramp function and the product of the ramp and the window function (R.W). **c:** Spatial representation (convolution kernel) of the ramp filter (R). **d:** Spatial representation (convolution kernel) of the windowed ramp filter (R.W).

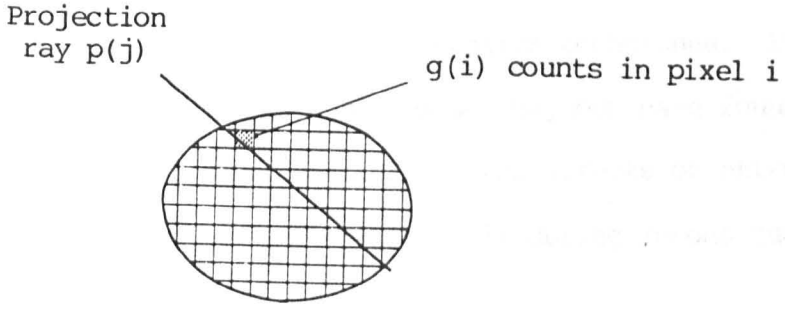

Figure 2.6 Iterative reconstruction: the projection data points are considered as rays p(j) equal to the sum of the counts g(i) in each pixel along the ray (Williams, 1985).

The basic strategy of iterative methods is to apply corrections to a matrix with arbitrary initial pixel count values in an attempt to match the measured projections. This procedure is repeated until the calculated projections agree with the measured ones to within the desired accuracy. Typically five to ten iterations are required.

Several correction schemes have been developed with differing sensitivities to noise or artefacts as a result of the differences in the sequence of application of the corrections. However, each iteration of these techniques is, effectively, the back projection of a set of correction values into a matrix with a pre-existing estimate of the count distribution. If the initial estimate is a matrix with zero in each pixel then the first iteration is simple back projection. For this reason, filtered back projection tends to be more efficient, in the presence of noise, than any of the iterative techniques. Iterative techniques are not, therefore, in common use, but have found application in certain algorithms which correct for the effects of attenuation and/or Compton scatter (see section 2.3.3) during reconstruction.

2.3.3 Attenuation compensation

The reconstruction theory above assumes that the count recorded in any projection pixel is directly proportional to the sum, along the ray, of the underlying count distribution (which is assumed in turn to be proportional to the activity distribution). In general this is not true and the projection counts are modified by the effects of attenuation processes (Moore, 1982). A beam of photons within the energy range used in gamma camera emission tomography (~80-400 keV) is primarily attenuated by photoelectric absorption and Compton scattering. The contributions of each of these processes depend on the composition, size and shape of both the radioactive source distribution and the medium in which the radioactivity is contained.

The effect of these processes is to degrade the reconstructed images in two ways. First, the images are distorted by undue weight being given to spatially more superficial, less attenuated sources. This results in a 'hot rim' artefact in the reconstructed tomograms, and reduced contrast at the centre of the slice. Secondly, true quantitation of the underlying activity distribution is lost, due to loss of counts from deep structures and the presence of an unknown contribution from Compton scattered photons in each projection pixel.

The principal assumption made at the time of reconstruction by most attenuation correction algorithms is that the object volume is homogeneous with regard to its absorption and scattering properties. Most methods require that a body contour for each slice be supplied. This may be manually input (usually as an ellipse) or may be determined automatically by edge detection in an initial reconstruction.

Many attenuation correction algorithms have been described, and they may be divided into three main groups.

(a) Preprocessing correction

The simplest approach is to attempt to correct the projection data before back projection. This is done by multiplying each element in the projection by a factor related to the length of the corresponding ray within the body contour (figure 2.7a). Activity is assumed to be uniformly distributed along the ray. Therefore, although preprocessing works for uniform distributions, or those consisting of small defects in a uniform background (~10% errors), it fails for small sources distributed in an inactive attenuating medium (Webb et al, 1983).

(b) Postprocessing correction

In this correction method, also known as the 'first order Chang method', a compensation matrix is built up from the expected point

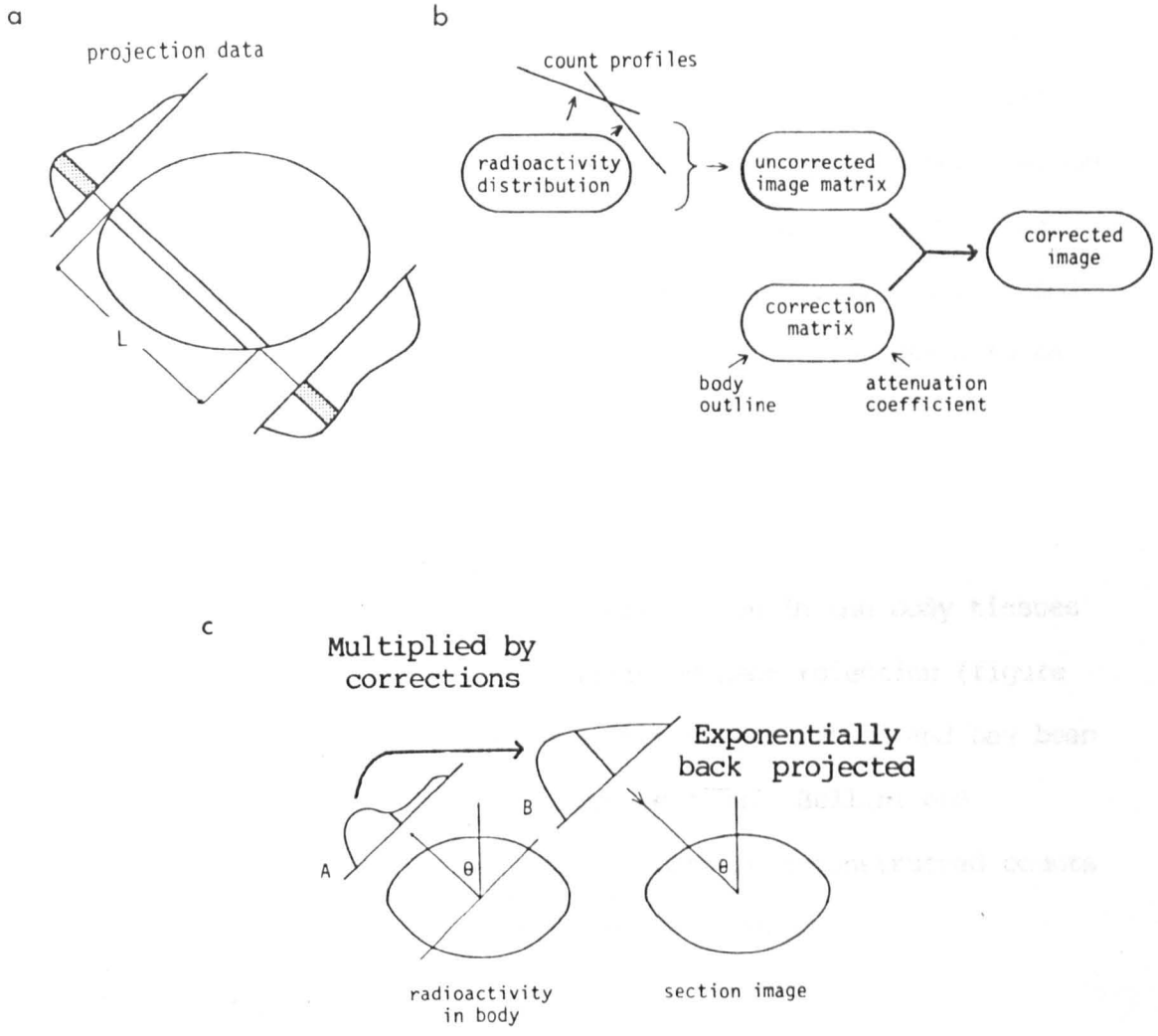

Figure 2.7 Attenuation correction (Williams, 1985). **a:** Pre-processing correction: the mean of counts in corresponding opposed projection points (shaded) is corrected for the attenuation expected in a column of uniformly attenuating material of length L lying between them. **b:** Post-processing correction: a transverse section image is formed and each pixel of the correction matrix generates an attenuation correction for the corresponding image pixel. **c:** Intrinsic correction: each data point in projection A is multiplied by attenuation correction factors derived from the ray path lengths from the mid-plane, producing the corrected projection B. After filtering the corrected projections are back projected with exponential weighting.

source detection efficiency for each pixel inside the body contour (Chang, 1978). The transverse section image is then reconstructed and corrected with the compensation matrix (figure 2.7b). A particular advantage of this method is that the linear attenuation coefficient can be variable with position in the body. For a uniformly attenuating phantom containing 'hot' spheres in a 'cold' background, Jaszczak and colleagues (1981) have shown accuracy of contrast reproduction to be about 10%.

(c) Intrinsic correction

These methods assume exponential attenuation in the body tissues and correct the projections prior to filtered backprojection (figure 2.7c). This is mathematically the most attractive method and has been shown to be more accurate than the above methods. Bellini and co-workers (1979) obtained deviations <4% between reconstructed counts in three equally active vials in a 'cold' background.

2.3.4 Quantitation

The methods of attenuation compensation described above assume that the attenuation can be described as a single exponential function. The situation is more complex than this due to Compton scattering processes and the relatively poor energy resolution of the detector. The energy resolution is such that when setting the analyzer window to obtain reasonable detection efficiency a range of incident gamma photon energies will be accepted. At a typical imaging energy of 140 keV the angle between a primary and scattered photon is large for a small energy change. For example, a 45^{o} scattered photon has an energy of 129 keV. Since a typical analyzer window (20%) accepts all energies in the range 126-154 keV, some scatter events, carrying degraded spatial information, will be recorded. By using an asymmetric energy window,

that is one centred above the photopeak, the number of scattered photons detected is reduced in relation to the number of unscattered photons. Unfortunately this is achieved at some loss in both detection efficiency and uniformity of detector response.

Alternatively, an approximation to overcome the problem may be included in the attenuation compensation scheme adopted. An 'effective' attenuation coefficient determined experimentally from a fitted mono-exponential function is used instead of the narrow beam (i.e.scatter excluded) linear attenuation coefficient. For 140 keV photons the true coefficient in tissue equivalent material is 0.15 cm^{-1}, but a value of 0.12 cm^{-1} is commonly used as an effective coefficient (Williams, 1985).

Attempts have been made to estimate the scatter contribution and to remove it from the images. One method is to subtract an experimentally determined fraction of an image acquired in a second energy window positioned in the Compton scatter region of the energy spectrum (Jaszczak et al, 1984). Alternatively, the spatial distribution of the scatter contribution relative to the response to unscattered photons may be deconvolved and subtracted from the image data (Axelsson et al, 1984). An attractive feature of this method is its ability to combine the deconvolution and subtraction with the filtered back projection during reconstruction (Floyd et al, 1985) and to compensate for non-uniform distributions of attenuation (Mukai et al, 1988). When these methods are used, attenuation compensation using the narrow beam attenuation coefficient is appropriate.

The corrections described, for attenuation and Compton scatter, enable reasonably accurate quantition of source activity, even in the presence of heterogeneous tissues. That is, after calibration of the imaging system, the counts contained within a given volume of the tomogram may be expressed in activity units (MBq). However, problems

arise when activity concentration is required.

The volume of a region imaged tomographically may be estimated by counting pixels. By system calibration using phantoms a cut-off, above which pixels are counted, is estimated. Assuming a fairly smooth point spread function for the system and a uniform distribution of activity in the volume to be estimated, this will be of the order of 50% of the maximum pixel count in the volume. When the target volume contains a heterogeneous activity distribution, an edge detection process, such as a gradient operator, yields better results.

For large volumes these methods work well, but for source distributions with dimensions comparable to the spatial resolution of the system the partial volume effect leads to volume over-estimation, and therefore activity concentration under-estimation. This sets the lower limit on the size of region within which quantitation may be performed tomographically.

2.4 Nuclear medicine image processing

Unprocessed gamma camera images tend to be of inferior quality, i.e. they have relatively poor resolution and a noisy appearance. The objectives of image processing as applied to images from gamma cameras are twofold. First, to improve the image quality so that abnormalities within the image are more readily observed, without an increase in the false detection rate. Secondly, to improve the quality so that the structures imaged are more easily recognized. This type of quality improvement is of particular value when it is desired to define regions of interest in dynamic function studies.

Before any image processing technique is applied routinely to clinical images the diagnostic improvement due to the processing must be evaluated by observer testing experiments. Clinical images in which the correct interpretation is known must be examined and reported by

observers. However, it is impossible to ascertain the location of all anomalies in clinical images. On the other hand, computer-simulated images and images of phantoms may not be realistic models of the clinical images. Therefore, it is best to evaluate performance of an image processing technique by both examination of clinical images and images of phantoms.

2.4.1 The gamma camera image

An image produced by a gamma camera is the convolution of the image expected from the source distribution with the point source image distribution (point spread function, PSF), with Poisson distributed noise added to each pixel in the resulting image (Evans, 1981). Therefore, the basic processing techniques applicable to the images are noise suppression and image enhancement to compensate for the PSF. Certain feature detection methods may also be applied.

2.4.2 Noise suppression

Noise is mainly found in the high spatial frequency part of the Fourier transform of the image. Thus noise suppression is achieved by multiplying the transformed image by a filter, the amplitude of which smoothly decreases with increasing spatial frequency, and then taking the inverse transform of the result. Assuming an isotropic imaging system (i.e. with a radially symmetric PSF) the filter which produces the maximum signal to noise ratio is the transform of the PSF and is therefore called the matched filter (Houston, 1981). From the convolution theorem it follows that convolution of the image with the PSF gives an identical result. The PSF of the gamma camera varies with depth in the object imaged and therefore an approximate 'average' PSF must be used when sources distributed in three dimensions are imaged. A commonly used adaptation is obtained by application of nine-point

smoothing with weights: $(1/16) \cdot \begin{bmatrix} 1 & 2 & 1 \\ 2 & 4 & 2 \\ 1 & 2 & 1 \end{bmatrix}$.

This filter may be implemented in a form which is executed very rapidly by replacing multiplications by bit shifts. A greater degree of smoothing can be achieved efficiently by application of the filter as many times as necessary, rather than by the use of a more complicated filter kernel.

Filters of this type degrade resolution and become less useful at high count densities. Filters which change according to the properties of the image can be more useful, i.e. non-stationary filters (Pizer and Todd-Pokropek, 1978). Areas of the image with low count density and thus low signal-to-noise ratio are smoothed heavily while high count density areas receive less smoothing. Smoothing is performed only across regions of approximately uniform density to avoid the averaging of signal and noise.

It is also possible to apply data bounding to the image data. The value of each pixel is compared with the mean of its neighbours and replaced when a significant difference is found. The replacement value chosen depends on the implementation but is normally either the mean of the neighbours or the limit of the confidence interval (calculated from the neighbours) which is closest in value to the original value of the pixel examined.

2.4.3 Image enhancement

Attempts have been made to construct resolution recovery filters, to compensate for the PSF of the gamma camera, i.e. to deconvolve the PSF from the image. This can best be appreciated in the Fourier domain since, in the absence of noise, the relationship G = I / MTF (where G and I are the transforms of the object and image distributions) follows

from the convolution theorem and the definition of modulation transfer function (MTF) as the transform of the PSF. However, 1/MTF (the inverse filter) magnifies the effect of high frequency noise to an unacceptable level and it is necessary to roll-off the filter to zero at the higher frequencies. This is equivalent to following the inverse filter, for deconvolution of the PSF, up to some cut-off frequency and applying smoothing at higher frequencies. Assuming radial symmetry, and for spatial frequency w with cut-off c, Tanaka and Iinuma (1970) have defined a filter, F, as

$$F(w) = 1/MTF(w) \qquad \text{for } w \leq c$$
$$= MTF(w)/\{MTF(c)^2\} \qquad \text{for } w > c.$$

It can be seen that for w>c the filter shape is that of the matched filter (figure 2.8a). The value of c is chosen from consideration of the image noise and from examination of side effects, such as 'ringing' or noise 'blobs', produced by the filter. The 'sharpness' of the change from inverse to matched filter tends to produce ringing in the filtered image.

A more generally useful filter has been defined (Metz, 1970) as

$$F = [1 - (1 - \{MTF^2\})^{n+1}] \; / \; MTF$$

(omitting w from both F(w) and MTF(w)). The transition of the Metz filter from inverse filter to matched filter is much smoother (figure 2.8b) and depends upon choice of n. When n=0 the filter is identical to the matched filter and for infinite n a pure inverse filter is obtained. Thus by decreasing n the filter may be adapted to increasingly noisy images. A non-stationary version of the Metz filter may be obtained by taking the inverse Fourier transforms of a 'family' of filters with different n, and applying them directly to the image as convolution kernels (King et al, 1988). Choice of the filter kernel to apply to a particular image pixel then depends on the pixel count.

Other filters which explicitly include the object and noise power

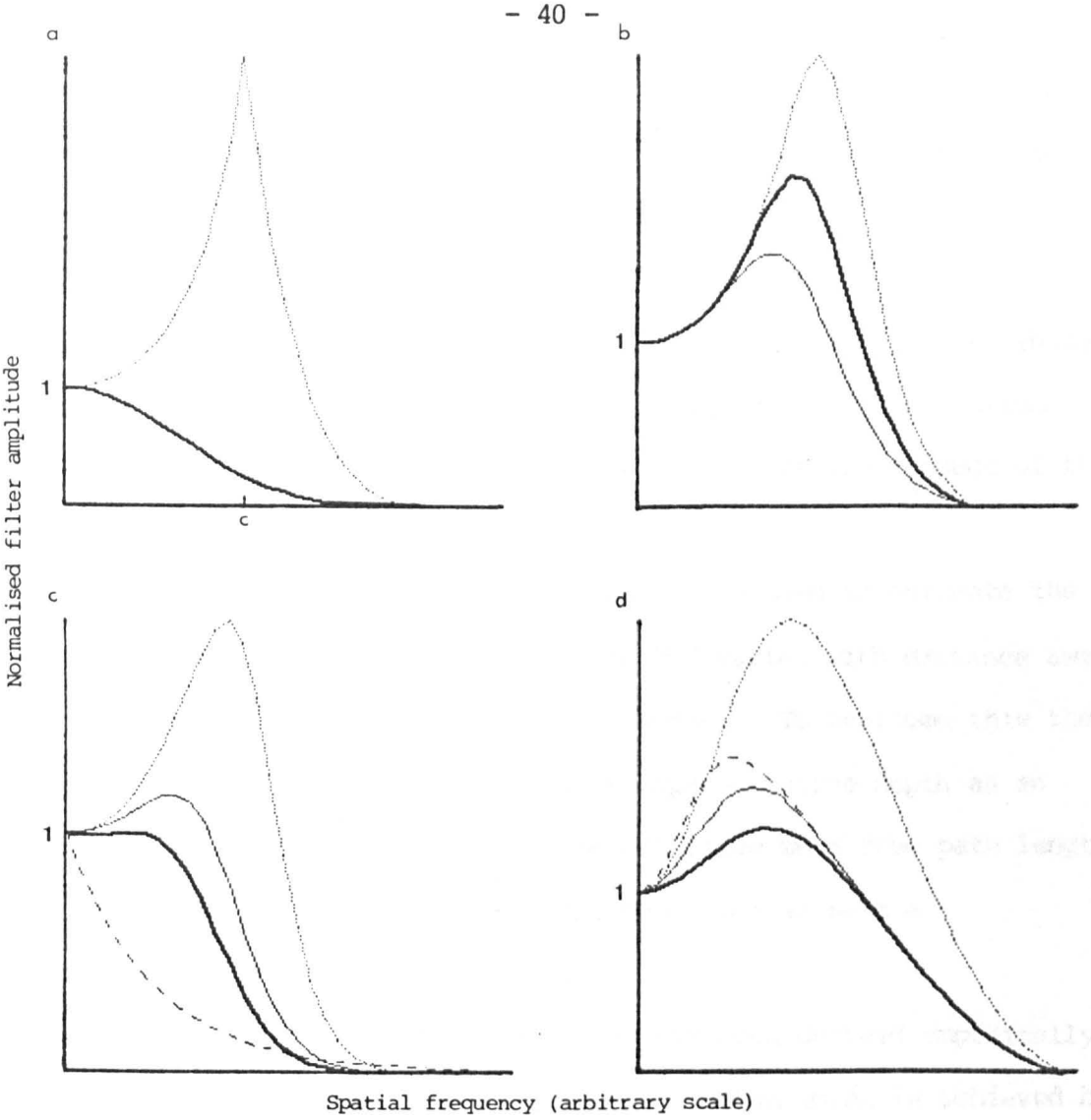

Figure 2.8 Image enhancement filters. Filter amplitude versus spatial frequency (arbitrary scale). Amplitude scale sets first point on each curve equal to 1.0. **a:** Tanaka/Iinuma function with cut-off frequency c (dotted), calculated for an assumed MTF (solid). **b:** Metz filters for the same MTF curve as in a. Curves show effect of varying the filter parameter n; from lowest to highest peak amplitude n = 4, 8, 16. **c:** Wiener filters for the same MTF curve as in a with an assumed object power spectrum (dashed curve). Total image count increases from lowest to highest peak amplitude. **d:** Amplitude functions for unsharp masking. One nine point smoooth was used as a light smooth and the number of nine point smooths for heavy smoothing was defined by a parameter s. Curve details are: dotted, s = 6, k = 0.75; heavy solid, s = 6, k = 0.5; light solid, s = 12, k = 0.5; dashed, s = 24, k = 0.5.

spectra have been applied (Houston, 1981; King et al, 1984; Webb et al, 1985). An example is the Wiener filter (figure 2.8c) which, for planar images, may be expressed (King et al, 1984) as

$$F = MTF^{-1} \cdot MTF^2 / \{MTF^2 + N/P\}$$

where P is the object power spectrum and N the total image count, which is equal to the average value of the noise power spectrum for Poisson noise. As with the Metz filter, the Wiener filter is the product of the inverse filter with a low pass filter.

One disadvantage of the above filters is the need to estimate the system MTF. For a gamma camera the system MTF varies with distance away from the collimator face (resolution gets worse). To overcome this the MTF is normally measured in water at some representative depth as an estimate of the depth averaged MTF. The effective mean free path length of photons of the energy of interest has been used as such a representative depth (King et al, 1986).

The final filter type to be discussed has been defined empirically (Corfield, 1975). The required mid-frequency enhancement is achieved by the subtraction of a fraction of a heavily smoothed image from a less smoothed version of the same image, i.e.

$$Mp = Ms - k.Ms'$$

where Mp is the processed image, Ms and Ms' are the least and most smoothed images and k is a constant, usually less than 1. Unsharp masking or 'Canterbury filtration', as the technique is called, can be performed very efficiently using the nine-point smoothing kernel given above. The effects of the filtration in the frequency domain are shown in figure 2.8d.

2.4.4 Feature detection

Certain image processing methods have been applied which attempt to enhance structures of particular interest selectively, rather than to

present accurately the activity distribution imaged. Neill and Hutchinson (1971) used a routine to detect 'cold' lesions (areas with reduced counts) in liver images. The local 'concavity' of each pixel was computed but the print-out only showed those pixels deviating from the mean by three or more standard deviations. Such methods can also be used to localise 'hot' lesions in images (convexity imaging).

Edge detection methods can be applied to the images in order to define the boundaries of structures of interest. This is of particular value when a region of interest must be defined, for example in dynamic imaging (see below). Methods which have been applied include isocount contours, gradient operators, second derivative and Laplacian operators (Davis, 1975; Chang et al 1980a; Goris and Briandet, 1983). The application of edge detection methods to the problem of the identification of the left ventricular boundary in equilibrium gated cardiac blood pool studies is addressed in detail in Chapter 6.

Certain radiopharmaceuticals localise in more than one organ or have a high residual blood pool activity. In order to identify the uptake in the sites of interest an image of the distribution of a second radiopharmaceutical may be subtracted from the primary image. For example, in parathyroid gland adenoma imaging, thallium-201 uptake in the thyroid may be superimposed on any uptake of this radionuclide in parathyroid adenomas. Therefore, an image of the thyroid recorded using technetium-99m in the form of pertechnetate, which localises only in the thyroid tissue, may be subtracted from the thallium image in order to highlight abnormal parathyroid uptake.

2.5 Dynamic image processing

The gamma camera may be used to record a series of images showing the change in activity distribution with time. Any of the processing methods already described may be applied to the individual images.

However, two further considerations in dynamic imaging are to identify variations in count rate with time within specific regions of the images (curve processing) and to produce images reflecting the distribution of such variations (data compression).

2.5.1 Curve processing

Time-activity curves derived from regions of interest within the images may be processed in a variety of ways. Two of the more commonly used methods are model fitting and deconvolution analysis.

The underlying physiology may be mathematically modelled. Such a model will predict the form which the time-activity curve may take. The parameters of the equation may be estimated for a given curve by least-squares fitting and their diagnostic value tested.

It is uncommon for the administered radiopharmaceutical to arrive as a bolus in the organ of interest. If it desired to examine the impulse response of an organ it is necessary to deconvolve a curve representing the arrival of tracer in the organ from the time-activity curve derived from the organ itself. For example, to examine renal tracer clearance, deconvolution of the renogram (Kenny et al, 1975) is widely used. Other applications of the deconvolution technique are found in first-pass nuclear angiocardiography (Chapter 5) and for the assessment of liver perfusion (Chapters 3, 4).

2.5.2 Data compression

In the context considered here, data compression may be considered as the extraction, from a series of dynamic images, of a set of images and/or curves which show some feature(s) of the data in a more easily assimilated form.

The series of images may be considered as an array of time-activity curves derived from the individual pixels. Measurements of parameters

for each of the curves may be made and formed into images which show the spatial distribution of each parameter. Such images are, therefore, called parametric images. A commonly used example of this type of image is the regional ventricular ejection fraction image derived from cardiac blood pool studies (figure P2.9b). Images may also be produced from the parameters of fitted curves, such as the amplitude and phase images of first harmonic Fourier analysis of cardiac blood pool studies (figure P2.9c,d).

2.6 Image processing and emission tomography

The noise in reconstructed tomograms, unlike that in the projection data, does not follow the Poisson distribution. The noise power spectrum for tomograms reconstructed with the ramp filter is itself a ramp function, i.e. the reconstruction amplifies high frequency noise. The noise power spectrum for tomograms reconstructed with a windowed ramp is a ramp function multiplied by the square of the chosen window (Todd-Pokropek and Jarritt, 1982). Therefore, the window function chosen should be of the types discussed above (2.4.2, 2.4.3).

The window function is typically applied in one of three ways, as a 1-dimensional projection data filter, as a 2-dimensional projection data filter or by post-reconstruction 3-dimensional filtering, and the application may be either in the Fourier domain or as convolution filters in the image space. Filtering the projections in one dimension gives a speed advantage over the other methods, since the required window can be convolved once with the ramp and the resulting filter used in the back projection. The major disadvantage of the technique is the resulting anisotropy in the reconstructions, i.e. the window is applied in the transaxial planes and sections formed at other angles are filtered only in the direction of these planes and streak artefacts are generated. Applying an equivalent filter in the axial direction prior

to reconstruction can eliminate streaks but does not result in a three dimensionally isotropic point source response (Gullberg, 1983).

Post-reconstruction filtering may be applied 1-dimensionally, in the axial direction to eliminate streak artefacts after reconstruction with the ramp convolved with a window, but is subject to the same limitations as axial pre-filtering. Two dimensional post-reconstruction filtering gives results which are inferior to two dimensional pre-filtering, due to the contributions of the data in adjacent transaxial planes to the final reconstructed value at any point with the latter method (King et al, 1984). Three dimensional post-reconstruction filtering gives an isotropic point source response. Also, there is less variation of MTF within a tomographic slice than with depth in a planar image and, therefore, the use of a single MTF for 3-dimensional post-reconstruction enhancement filtering is appropriate (King et al, 1984). However, this method is the slowest in practice, and has not received wide use.

The use of a two-dimensional radially symmetric filter kernel applied to the projection images prior to transaxial reconstruction with the ramp filter gives a three dimensionally isotropic point source response (Gullberg, 1983) and better image quality than the same filter applied in 1-dimension (King et al, 1987). The same filters as are used for processing of planar images may be applied, and execution times are conveniently short compared to 3-dimensional filtering.

2.6.1 Reconstruction filters

Chapters 7 and 8 of this thesis describe experimental work to determine the optimum reconstruction filter, from those implemented on the nuclear medicine computer at University Hospital, Nottingham, for myocardial perfusion tomography. The work was performed using a Nodecrest V76 computer running Micas III nuclear medicine software

(Nodecrest Medical Systems Ltd., Byfleet). Using this software tomographic projection data are reconstructed by filtered back projection using a 1-dimensional convolution kernel. The frequency representations of the filters available are given in Table 2.1 and are illustrated in figure 2.10. In addition to these filters, the effects of pre-reconstruction and post-reconstruction smoothing were also examined. The smoothing filters used are defined on pages 161 and 196.

Table 2.1 One dimensional back projection filters

Details of the tomographic reconstruction filters available in the Nodecrest Micas III nuclear medicine software package. These filters are plotted in figure 2.10.

Filter number	Filter amplitude equation	Name of filter	Reference
1	$A(w) = \left\lvert \frac{\sin \pi w a}{a} \right\rvert$	Shepp-Logan, sharp	Larsson, 1980
2	$A(w) = \left\lvert \frac{\sin \pi w a}{a} \right\rvert \lvert 0.4 + 0.6 \cos 2\pi w a \rvert$	Shepp-Logan, soft	Larsson, 1980
3	$A(w) = \lvert w \rvert$	Ramp	Ramachandran & Lakshminarayanan, 1980
4	$A(w) = \lvert w \rvert (1 - \lvert aw \rvert)$	Parabolic	Supplied by Nodecrest without reference
5	$A(w) = \lvert 0.5w \rvert \lvert 1 + \cos 2\pi w a \rvert$	Ramp Hann+	Chesler & Riederer, 1975
8	$A(w) = \frac{1.}{4a}\left[1 + \frac{\sinh\{2\pi^2 a(w - 1/4a)\}}{\sinh\{\pi^2/2\}}\right]$	Modified ramp	Supplied by Nodecrest without reference

Spatial frequency is given by w, with pixel size a, and cut-off, w_c, at the Nyquist frequency, i.e. 1/2a.

+ In the literature, the Hann filter is often referred to as the Hanning filter.

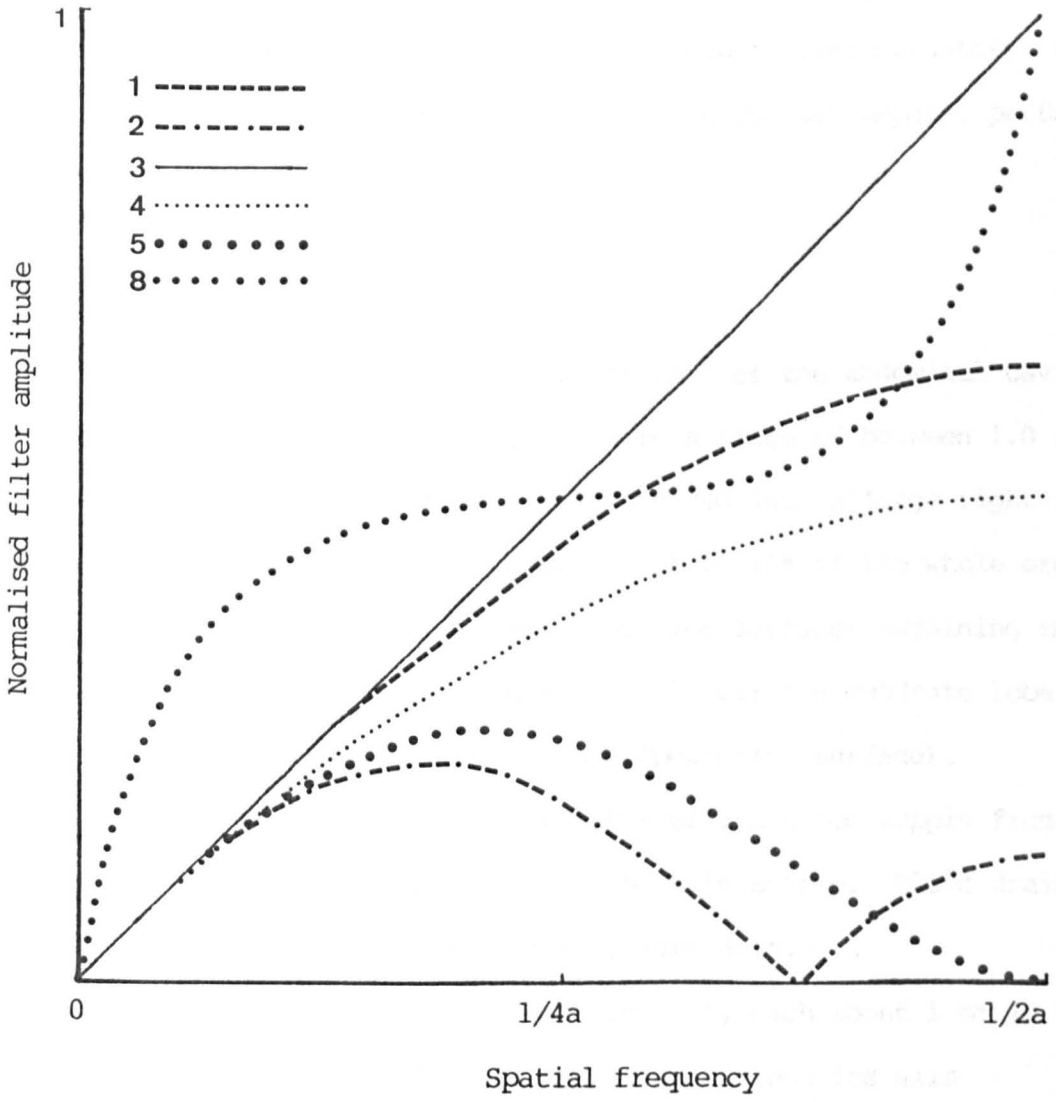

Figure 2.10 Spatial frequency representations of back projection filters. Filter amplitude versus spatial frequency (for pixel size a) for the six one dimensional back projection filters in the Nodecrest Micas III nuclear medicine software package. Table 2.1 specifies the functional form of these filters.

3. The liver

The measurement of hepatic blood flows has received attention from many groups of workers recently (see Section 3.5.3) in efforts to diagnose the presence of liver metastases from primary malignancy elsewhere in the body. This chapter describes the structure and function of the liver, and reviews the literature relating to nuclear medicine imaging of the liver. Chapter 4 describes experimental work performed to identify patients harbouring occult liver metastases from primary colorectal carcinoma, using $^{99}Tc^{m}$-tin colloid hepatic perfusion images.

3.1 Liver structure

The liver occupies the upper, right part of the abdominal cavity. Its mass is approximately 1.5 kg, but with a range of between 1.0 and 2.5 kg in normal adults. The liver is divided into a large right lobe and a smaller left lobe, which comprises about 15% of the whole organ. The right lobe, on the inferior and posterior surfaces adjoining the left lobe, is subdivided into two smaller lobes; the quadrate lobe (inferior surface) and the caudate lobe (posterior surface).

The liver receives approximately 80% of its blood supply from the portal vein and the remainder from the hepatic artery. Blood drains from the liver via the hepatic veins (figure 3.1a,b).

The liver consists of polyhedral lobules, each about 1 mm in diameter and having a small intralobular vein along its axis (figure 3.1c). Each lobule is surrounded at its edges by groups of three tubes, known as portal triads. Each portal triad contains a branch of the portal vein, a branch of the hepatic artery and a bile ductule. Blood from the interlobular vessels passes through venous sinusoids into a central vein. The central veins unite to form hepatic veins, which drain into the inferior vena cava.

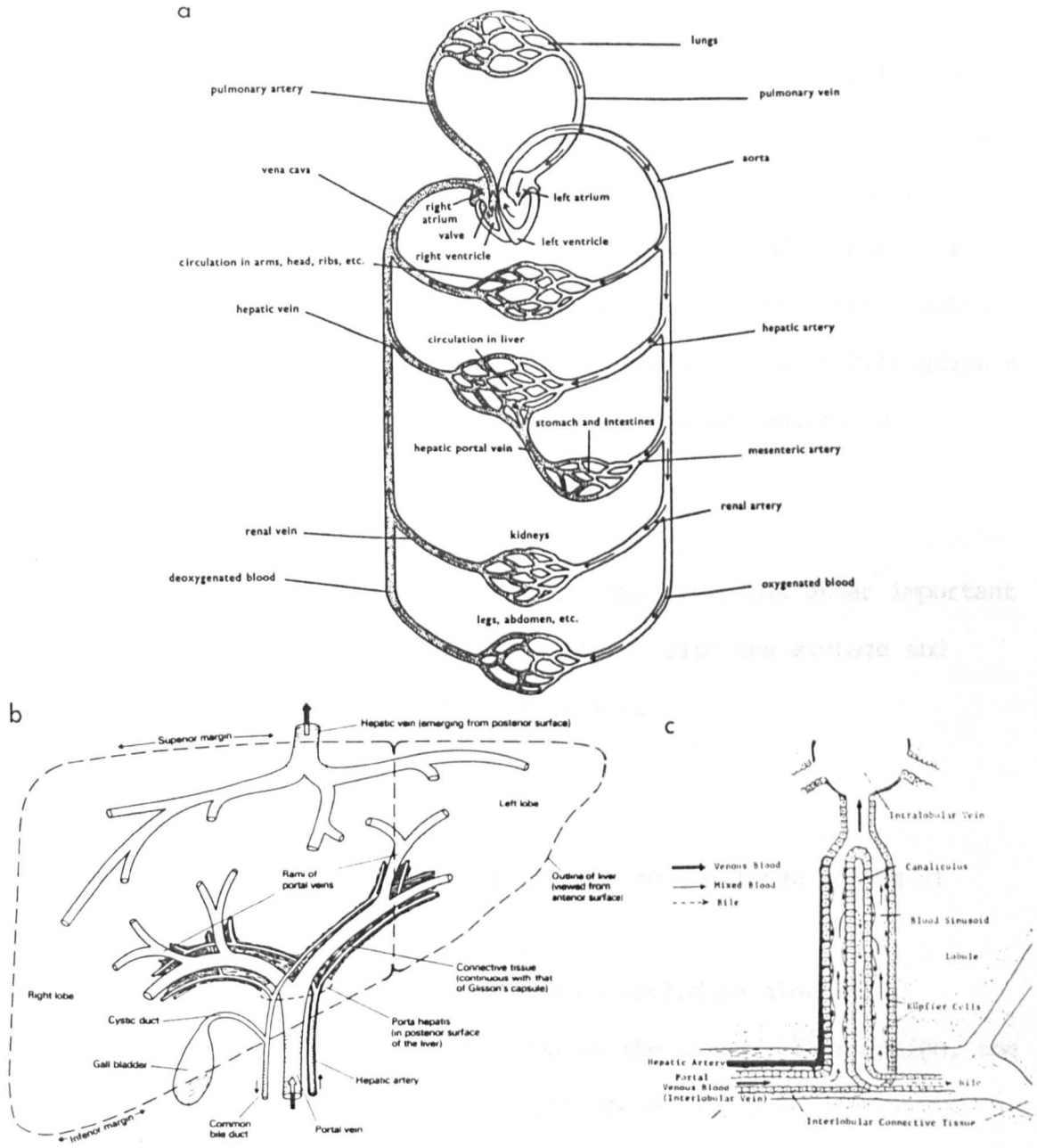

Figure 3.1 The flow of blood and bile in the liver. **a:** The circulation of blood (Mackean DG, 1973. Introduction to Biology, p95. John Murray, London). **b:** The main blood and bile vessels of the liver. The portal veins, hepatic artery and bile duct divide into branches until their terminal portions, the portal triads. The hepatic veins arise from the confluence of the intralobular veins. (Bowman WC and Rand MJ, 1980. Textbook of Pharmacology, 2nd. edition, p26.2. Blackwell Scientific Publications, Oxford). **c:** Blood and bile flow within a lobule (Bowman WC, Rand MJ and West GB, 1968. Textbook of Pharmacology, p326. Blackwell Scientific Publications, Oxford).

The sinusoids are arranged approximately radially in the lobule. The walls of the sinusoids are lined with hepatocytes: these form bile, which is secreted into a bile canaliculus from which it drains into the bile ductule of a portal triad. The biliary vessels join together to form the hepatic duct which runs to the gall bladder and common bile duct. The walls of the sinusoids also contain phagocytic Kupffer cells which form part of the reticulo-endothelial system. Figure 3.1c gives a diagrammatic representation of a sinusoid and a bile canaliculus.

3.2 Liver function

In addition to the formation of bile, the liver has other important functions. These are concerned with the blood, with the storage and release of nutrients, and with detoxification.

3.2.1 Blood

The liver acts as a blood reservoir due to the large volume of blood in its sinusoids and veins.

Essentially all of the plasma proteins including albumin, fibrinogen and some globulins are formed in the liver. In addition, the liver is one of the sites of foetal erythropoiesis.

Old erythrocytes may be trapped and destroyed in the liver as well as the spleen, the porphyrins derived from red cell destruction in the spleen reaching the liver via the portal vein.

3.2.2 Bile

Bile is produced in the liver at a rate of 500 to 1000 ml per day and is stored and concentrated in the gall bladder, from which it is discharged at intervals through the common bile duct into the duodenum. Bile is an alkaline fluid consisting principally of bile salts and bile pigments. Bile salts are salts of fatty acids which reduce surface

tension and emulsify fats. Additionally they increase the lipolytic activity of pancreatic juice in the duodenum. The bile pigments are bilirubin and its oxidised form, biliverdin. Bilirubin is metabolysed by the liver from porphyrin and is excreted in the faeces. Porphyrins are derived from the diet and as products of red cell destruction.

Most bilirubin appears in the bile but a little is absorbed into the blood and binds to α-globulin. An excess of blood borne bilirubin gives the characteristic yellow skin colour of jaundice.

3.2.3 Nutrients

The liver stores vitamins, notably vitamins A, D2 and K. It is the site of glycogenesis, in which monosaccharides, absorbed from the small bowel, are carried by the portal venous blood to the liver where they are synthesized into glycogen. Glycogen is stored in the liver. Neoglycogenesis, in which glycogen is synthesized from non-carbohydrate sources, including amino acids, also takes place in the liver. The liver is the most important site for β-oxidation of fatty acids and for maintaining the balance of the metabolic conversions of fatty acids and carbohydrates.

3.2.4 Detoxification

Potentially toxic products of metabolism are converted into non-toxic substances in the liver prior to excretion. For example, urea is produced from the ammonia formed in deamination of amino acids.

Substantial metabolism of certain orally administered drugs takes place in the liver. The drugs are absorbed from the gut and pass in the portal vein to the liver. Hence, hepatic perfusion may have a significant effect on drug metabolism and elimination.

3.3 Liver blood flow

Liver blood flow may be defined as the amount of blood which perfuses the liver per unit time. Most blood entering the liver through the hepatic artery and the portal vein passes through the sinusoids into the hepatic veins, as described above. However, small amounts of blood bypass the sinusoids through intrahepatic and extrahepatic arteriovenous and venovenous anastamoses. These shunts may become quite enlarged and new ones may be formed due to pathological conditions such as cirrhosis of the liver (McIndoe, 1928). Therefore, a fraction of the total liver flow is non-functional, and the size of this fraction depends on the severity of the pathological condition.

The estimation of liver blood flow by quantification of dye extraction or colloid clearance rates is described below.

3.3.1 Dye extraction method

Parenchymal cells are capable of extracting certain dyes from the blood in the sinusoids. The dyes, however, are not cleared completely from the blood and therefore a fraction appears in the hepatic veins.

The classic method of estimating hepatic blood flow (Bradley et al, 1952) employs bromosulphalein (BSP) and uses the Fick principle to calculate liver plasma flow (LPF) from the equation:

$$LPF = q/(C_a - C_v)$$

where q is the rate of dye removal and C_a and C_v are the dye concentrations in the plasma entering and leaving the liver. Since the hepatic arterial and portal venous blood entering the liver cannot be sampled directly, peripheral arterial or venous blood samples are taken.

To perform the measurement, an hepatic vein is catheterised and the BSP is supplied by continuous infusion. Peripheral dye concentration is kept constant, so the rate of removal by the liver, q, is equal to the rate of infusion, assuming that only the liver removes the dye. Dye concentrations are determined colorimetrically. The liver blood flow is

calculated from the equation:

$$LBF = LPF/(1 - H/100)$$

where H = the percentage haematocrit. The method is invasive and time consuming and is only rarely performed more than once in the same patient.

3.3.2 Colloid extraction method

Dobson et al (1953) first described the colloid extraction method of determing LBF. This method used a single injection of radiolabelled colloidal material. Colloidal material of suitable particle size (range 0.02 to 10 μm) is extracted from the sinusoids by the Kupffer cells, and the extraction rate is determined by measuring the rate of disappearance of colloid from the peripheral blood. The method assumes the complete removal of the colloid during a single passage through the liver. Liver blood flow is thus given by:

$$LBF = k_c V$$

where k_c is the rate constant of clearance of colloid from the circulation and V is the blood volume (determined by an independent method). The rate constant is calculated as the rate constant of the first exponential component of a plot of count rate of peripheral blood samples against time.

Some of the material appearing in the hepatic veins bypasses the sinusoids, as mentioned previously, and therefore, is not extracted by the Kupffer cells. Hence, clearance is not complete in a single passage, so the calculated LBF represents the blood perfusion of the sinusoids. This functional blood flow is the quantity of most direct clinical interest.

The efficiency of hepatic removal of colloidal particles is dependent on their size, the half time of their disappearance from the blood increasing with decreasing particle size. Particles with a

diameter greater than 10 μm, are predominantly trapped in the lungs, during the first pass following intravenous injection, while particles less than 0.02 μm in diameter are removed by the reticulo-endothelial cells of the bone marrow, in addition to liver and spleen uptake. Nearly all colloidal preparations contain particles of different sizes, and the analysis described gives the rate constant of the fastest component of disappearance, i.e. of the largest particles. The effect of slow removal of particles at sites other than the liver is thus corrected for.

Nevertheless, it should be noted that this method results in a value of liver blood flow which will always be an over-estimate, since there is always some clearance of colloidal material by the spleen and bone marrow.

Radiolabelled colloidal materials may be used for liver imaging and these images can provide quantitative measurements of liver blood flow. These uses are described in Sections 3.4 and 3.5 respectively.

3.4 Radionuclide imaging of the liver

Liver morphology, liver function and liver blood flow may be evaluated by radionuclide imaging.

3.4.1 Liver morphology

Imaging the distribution of $^{99}Tc^{m}$-labelled colloid using a gamma camera can provide useful diagnostic information relating to the size and position of the liver and of space occupying lesions within the liver. It may also be helpful in the evaluation of diffuse hepatic disease. Drum (1982) and Waxman (1982) reviewed the literature relating to colloidal imaging of space occupying lesions and diffuse disease, respectively.

Space occupying lesions, such as benign and malignant tumours,

abscesses and cysts are seen as focal areas of decreased tracer uptake in the liver. Diffuse hepatic disease, such as cirrhosis results in a number of patterns, depending on the stage and severity of the disease. Early cirrhosis is often marked by a diffuse reduction of uptake of tracer in the liver, with slightly increased uptake in the spleen and bone marrow. As the disease progresses the liver tends to be reduced in size and the spleen may become enlarged. Redistribution of activity to spleen and bone marrow becomes marked.

It should be noted that the relative distribution of colloid between liver and bone marrow, in the normal subject, is dependent on the particle size distribution, as discussed in Section 3.3.2.

3.4.2 Hepatobiliary function

Hepatobiliary function may be evaluated by dynamic imaging of an agent that is rapidly extracted by the hepatocytes and excreted into the bile ducts.

Radiopharmaceuticals having these properties include $^{99}Tc^{m}$-labelled iminodiacetic acid (-IDA) analogues, $^{99}Tc^{m}$-labelled pyridoxylideneglutamate (-PG) and ^{123}I-rose bengal (-RB) (Hardy and Wilson, 1981). Hepatobiliary scintigraphy with IDA analogues is the procedure of choice in the evaluation of patients with suspected biliary tract disease (Gliedman and Wilk, 1982). It is also particularly useful in cases of acute cholecystitis, when failure to visualize the gall bladder within four hours on IDA imaging in a fasted patient with normal biliary to bowel flow has proved 98% accurate in establishing the diagnosis (Weissmann et al, 1981). Imaging with ^{123}I-RB has been shown to be of value in distinguishing between causes of neonatal jaundice (Minford et al, 1984). In particular differentiation between biliary atresia and other causes of jaundice is possible by imaging over a 48 hour period, since radioactivity in the bowel is an indication of the

absence of biliary atresia. This is of great value as early surgical intervention is essential in cases of biliary atresia, but is contra-indicated otherwise.

3.4.3 Liver blood flow

Large liver tumours receive their blood supply mainly, if not exclusively from the hepatic artery rather than the portal vein (Breedis and Young, 1954; Ackerman et al, 1969). Therefore, a dynamic series of images recorded over the liver following a bolus i.v. injection of radiopharmaceutical shows the tumours as areas of high arterial but low portal flow (Waxman et al, 1972; De Nardo et al, 1974; Stadalnik et al, 1975; Witek and Spencer, 1975). This procedure can be carried out using $^{99}Tc^{m}$-labelled colloids, and it may then be followed by static imaging to show liver morphology. Waxman et al (1972) reported that this technique could not differentiate between cirrhosis, lymphoma or diffuse metastatic disease. However, the test was useful in the differential diagnosis of hepatic cysts or abscesses from large tumours, and in distinguishing between normal and pathological livers.

3.5 Quantification of liver blood flow and clearance

It has been suggested that quantitative blood flow studies may give better differentiation of diffuse parenchymal disease from metastatic involvement than visual inspection of the images, as described above (Sarper et al, 1981a).

This differentiation has been attempted by measurement of colloid clearance rates (DeNardo et al, 1976), by measurement of portal flow after rectal administration of tracer (Steinberg et al, 1974) and by measurement of the relative contributions of the hepatic arterial and portal venous flows to the total liver blood flow (Sarper et al, 1981a; Sarper et al, 1981b; Sarper and Tarcan, 1983; Parkin et al, 1983;

Robinson et al, 1983; Fleming et al, 1981a; Fleming et al, 1983; Wraight et al, 1982).

3.5.1 Colloid clearance

DeNardo et al (1976) described a mathematical model of the reticulo-endothelial system. Data from a 25cm field of view gamma camera and a probe detector system were accumulated. The gamma camera, with diverging collimator, was positioned anteriorly over the liver and spleen, while the probe was positioned posteriorly so as to detect counts from bone marrow and the aortic arch. Colloid clearance rate constants for the liver, spleen and bone marrow were derived in normal volunteers and in patients with diffuse hepatic disease. The authors showed that the rate constants derived could differentiate between cirrhosis, hepatitis, fatty infiltration of the liver and normal livers.

However, there was an implicit assumption in the model that any changes in liver clearance rates were due to changes in liver perfusion. Fleming et al (1981b) were able to show that extraction efficiency of the liver falls by at least 15% in rats with carbon tetrachloride induced cirrhosis. Since De Nardo and colleagues (1976) did not apply corrections for changing extraction efficiencies the clearance rates of livers with metastatic deposits could not be differentiated from rates measured for normal livers.

3.5.2 Rectal administration

Another approach to the use of liver blood flow studies in diagnosis employs the rectal administration of tracers. An absorbable tracer will pass from the intestines via the portal vein to the liver. Rectal instillation of ^{131}I-sodium iodide solution was performed in 38 patients by Steinberg et al (1974). By monitoring time-activity curves from the liver and plasma two patterns of flow were identified. Type I

indicated a direct return to the liver via the portal vein, while type II indicated significant porto-systemic collateral flow. Normal volunteers, patients with metastatic disease, and patients with chronic liver disease without portal hypertension, showed type I flow patterns. Patients with chronic liver disease and portal hypertension showed type II flow patterns. This renders the technique of little value in the differential diagnosis of diffuse metastatic disease.

3.5.3 Relative flow measurement

Several groups have examined the possibility of assessing the relative hepatic arterial and portal venous contributions to total hepatic blood flow. Three methods have been used; the basis of all methods is as follows. A time activity plot of the arrival of a bolus of activity in the liver can be considered as two linear phases (figure 3.2a); the first may be considered as due solely to the hepatic arterial flow, and the second to portal venous flow. The magnitude of the slope of each line is proportional to the flow by the particular route. The assumptions in this model will be discussed below.

(a) Method 1

Sarper et al (1981a) calculated a liver 'arterialization index' (AI) from the slopes of the time-activity curves. This index was defined as the ratio of the slope over the 8 seconds immediately before the portal venous flow to the slope over 8 seconds after the start of portal venous flow (figure 3.2b). The time at which portal venous flow began was defined as corresponding to the time of peak activity in a curve derived from a region of interest over the right kidney. An 'arterialization index' greater than 0.5 had a predictive value of 98% for hepatic metastases, in a study of 228 patients with suspected metastases. Diagnoses were confirmed by biopsies.

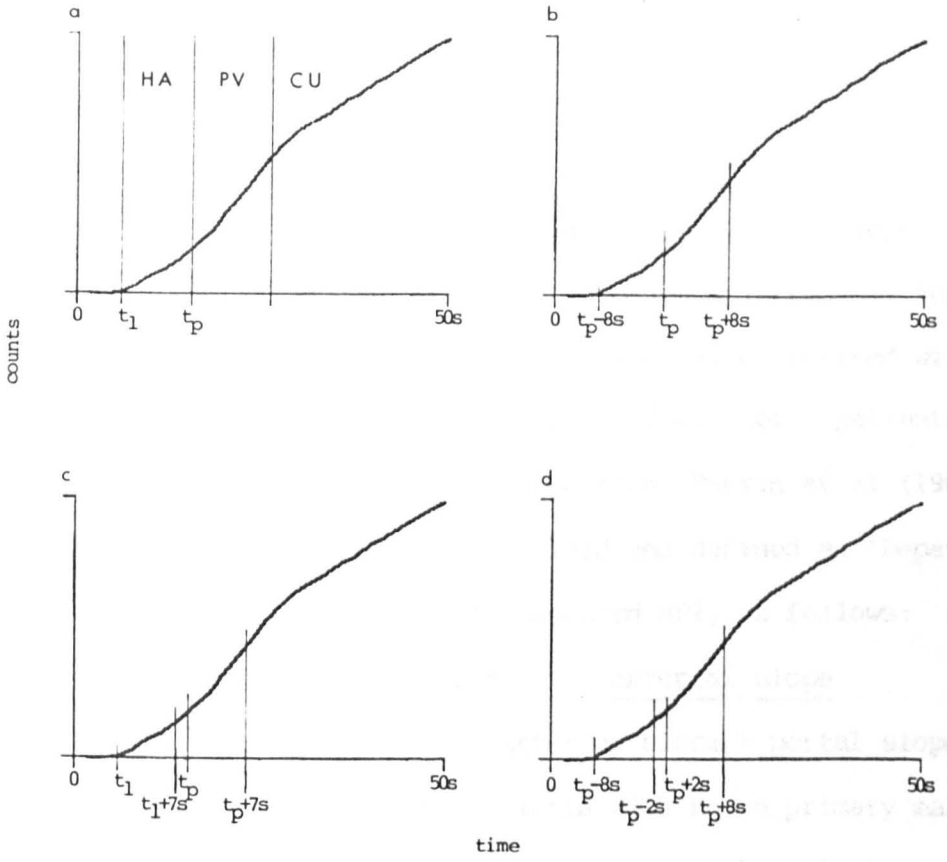

Figure 3.2 Colloid dynamics of the liver.

HA = Hepatic arterial phase t_1 = time activity first seen in liver

PV = Portal venous phase t_p = time of peak renal activity

CU = Colloid uptake phase b(i,j) = slope of liver curve between times i and j.

a: Liver uptake curve

b–d show times used in the definition of three liver blood flow indices.

b: Arterialization index, AI (Sarper et al, 1981a).

$$AI = b(t_p\text{-}8s, t_p)/b(t_p, t_p\text{+}8s)$$

c: Hepatic-portal index, HPI (Sarper et al, 1981b; Sarper and Tarcan, 1983)

$$HPI = \frac{b(t_p, t_p\text{+}7s)}{b(t_1, t_1\text{+}7s) + b(t_p, t_p\text{+}7s)} \times 100\%$$

d: Hepatic perfusion index, HPI (Parkin et al, 1983).

$$HPI = \frac{b(t_p\text{-}8s, t_p\text{-}2s)}{b(t_p\text{-}8s, t_p\text{-}2s) + b(t_p\text{+}2s, t_p\text{+}8s)}$$

A similar method was used (Sarper et al, 1981b; Sarper and Tarcan, 1983) to calculate an 'hepatic-portal index' (figure 3.2c). This was defined as follows:

$$\text{Hepatic portal index, HPI} = \frac{\text{portal slope}}{\text{arterial slope + portal slope}} \times 100\%$$

HPI was 66 $\pm$ 7% (mean $\pm$ 1SD) in a control group of normals. The degree of reduction of HPI was found to be significantly correlated with the angiographic grade of perfusion in a group of cirrhotic patients.

In a study of liver metastasis detection, Parkin et al (1983) used a bolus injection of $^{99}Tc^{m}$-sulphur colloid and defined an 'hepatic perfusion index' (figure 3.2d), also denoted HPI, as follows:

$$\text{Hepatic perfusion index, HPI} = \frac{\text{arterial slope}}{\text{arterial slope + portal slope}}$$

Robinson et al (1983) studied 80 patients with known primary malignancy and 20 normal volunteers using this technique. All patients proceeded to laporotomy which provided confirmation of the diagnosis. Conventional static colloid scintigraphy was abnormal in 67% of patients with positive laparotomies (18/27), while HPI was abnormal (>0.46) in 96% (26/27) of these patients. Several patients with normal static scintigrams and abnormal HPI had small tumour nodules (<2cm diameter). The findings indicated that the presence of metastatic disease in the liver increased the arterial perfusion with respect to portal perfusion.

(b) Method 2

A variation in this technique was reported by Fleming et al (1981a, 1983). This method, using a $^{99}Tc^{m}$-sulphur colloid bolus and dynamic images over 40 seconds, resulted in a calculation of the mesenteric fraction of total liver perfusion (i.e. the fraction of blood supply from the gut) and a portal fraction (the fraction of blood supply from the spleen and the gut).

These values were calculated as follows:

Mesenteric fraction, $MF = 1 - [L(t_a)/L(t_r)]$,

where $L(t_a)$ = liver count rate at the time of the end of the hepatic artery phase (t_a),

$L(t_r)$ = liver count rate at the time of the end of the portal venous phase (t_r),

assuming that the splenic extraction efficiency is 100% and the hepatic arterial extraction efficiency is equal to portal venous extraction efficiency.

Portal fraction, $PF = (B - AB + 1)/(1 + B)$,

where $A = L(t_a)/L(t_r)$,

$B = L/S$,

L = liver count rate at 15 minutes

and S = spleen count rate at 15 minutes,

with both L and S computed as the geometric mean of count rates in anterior and posterior images. This expression assumes that all extraction efficiencies are equal.

The time t_a was estimated by taking the mean of (i) the time at which half the peak left ventricular counts were recorded (after the peak), (ii) the time of peak renal activity (ie t_p in figure 3.2), and (iii) the time at which 85% of the mean splenic plateau level was first recorded. The time t_r was the mean of the time of (i) peak recirculation activity in the left ventricle, (ii) minimum renal activity and (iii) minimum splenic activity. Twelve fasted normal volunteers gave values of MF in the range 0.50 to 0.75 (mean 0.57) and PF in the range 0.57 to 0.78 (mean 0.64). The method was validated in a digestion study of the twelve normal volunteers. There was a significant increase ($p < 0.001$) in the means, in all subjects, between fasting and post prandial studies, in both mesenteric (to 0.80) and portal fractions (to 0.81). Additionally, in two patients with known

reduced mesenteric flow (portosystemic shunting of blood and cirrhosis) values of mesenteric fraction were 0.27 and 0.28 respectively.

(c) Method 3

A different approach to the relative measurement of hepatic arterial and portal venous flow was described by Wraight et al (1982). Following a bolus injection of $^{99}Tc^{m}$-sulphur colloid imaged over 5 minutes, they determined the fractional arterial flow, R, defined as the ratio of hepatic arterial flow to the sum of hepatic arterial and portal venous flow. By scaling the splenic curve so that the initial rise of the splenic curve fitted the initial rise of the hepatic curve, while assuming that the splenic uptake curve was of similar shape to the arterial component of the hepatic uptake curve, a curve representing this arterial component was derived (figure 3.3). Fractional arterial flow was derived from the expression:

$$R = \frac{C_a}{C_t} \cdot \frac{L}{L+S} \times 100\ \%$$

where C_a = height of arterial curve at 5 minutes,

C_t = height of total liver curve at 5 minutes

and L, S are as defined for Method 2

In addition an estimate of liver blood flow, F, was made from the rate of clearance of tracer from the cardiac blood pool.

$$F = \frac{C_{30} - C_{120}}{C_{30}} \cdot \frac{L}{L+S}$$

where C_{30} and C_{120} are the count rates of the cardiac blood pool curve at 30 and 120 seconds after the peak count rate, respectively. The value of F is proportional to total liver blood flow if bone marrow uptake and colloid clearance before 30 seconds are assumed to be negligible.

A study of 92 patients was performed, with clinical follow up.

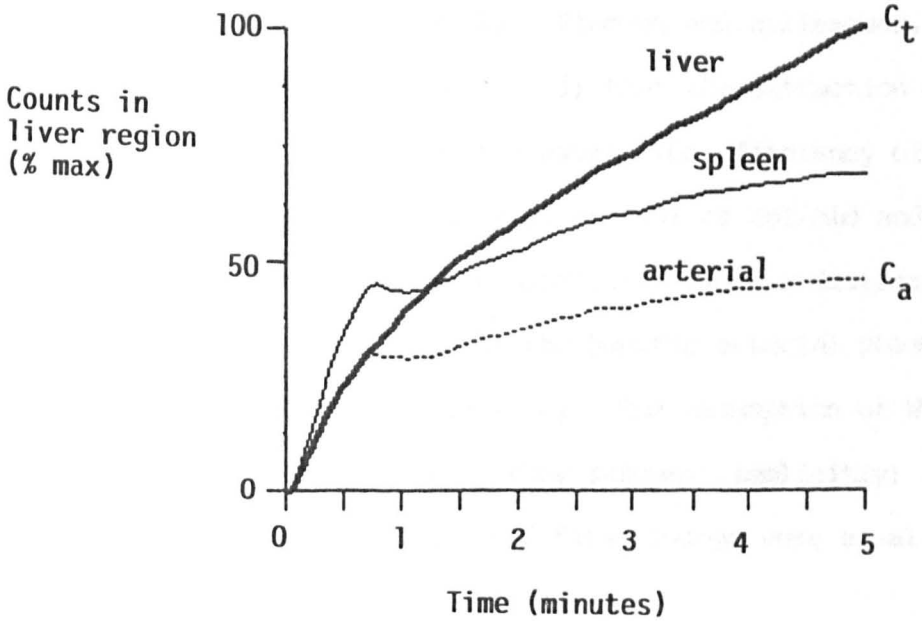

Figure 3.3 Colloid uptake of liver and spleen.

From 24 normal patients an upper limit of normal of R of less than 29% and a lower limit of normal of F of greater than 2.1 were determined. All cirrhotics (13) and 18 of 22 patients with hepatic metastases had values of R greater than 29%. The index of total hepatic flow, F, was normal in most patients with metastases and reduced in most cases of cirrhosis. Hence it was possible to distinguish metastatic disease from cirrhosis.

(d) **Assumptions**

The models of Sarper, Parkin, Fleming and colleagues, make three important assumptions. These are (i) that the extraction efficiency of the spleen is 100%, (ii) that the extraction efficiency of the liver is the same regardless of the route of arrival of colloid and (iii) that by monitoring the kidney and other abdominal organs a distinct portal phase can be identified, separate from the hepatic arterial phase and subsequent recirculation of activity. The assumption of Wraight et al is a variation of this, in that they assumed (implicitly) that liver and spleen extraction efficiencies and flow timings were equal, for arterial flow.

(i) The effect of splenic extraction efficiencies being less than 100% (Fleming et al, 1983) will be to introduce a systematic error into the calculation of hepatic portal index (HPI) or mesenteric fraction (MF) if it is assumed that the extraction efficiency has only a small variation between patients. However, a large and indeterminate error will be introduced if the splenic extraction efficiency varies significantly from patient to patient.

(ii) In the rat, hepatic extraction efficiency has been measured at 81% + 2% s.e.m. (Fleming et al, 1981a). Values obtained after hepatic arterial injection and after portal venous injection were not significantly different. However, in cirrhosis (Fleming et al, 1981b)

or when significant porto-systemic shunting occurs, a large uncertainty in extraction efficiency may be introduced.

(iii) The effect of temporal uncertainty in the hepatic arterial and portal venous phases is reduced by using a set protocol to identify the end of the hepatic arterial phase. Izzo et al (1983) believe that the concept of a division of liver blood supply into arterial and portal venous flow is inadequate. They have proposed three phases of flow. The filling phase, representing both arterial and portal flow, the collateral circulation output phase, representing the shunting of blood out of the liver, and the liver circulation output phase, representing colloid extraction.

(e) Deconvolution

The time-activity curve obtained from the liver may be considered as the convolution of an arterial curve with the sum of two impulse responses (figure 3.4). The first of these impulse responses is the response of the liver to a bolus injection of tracer into the hepatic artery. The second is the response of the liver to the flow through the portal vein. This flow is effectively the mesenteric arterial flow which has been delayed and blurred by passage through the capillary bed of the gut. When a non-extractable tracer is used, the heights of the two impulse response curves are proportional to the hepatic and portal flow. Barber and Tindale (1989) have described a method of constrained deconvolution which derives these heights from the liver and aortic time-activity curves to estimate the liver flow fractions due to the hepatic arterial and portal venous routes.

In the case of an extractable tracer, such as a colloid, the expected impulse responses are of the form shown in figure 3.5. In this case the flow fractions are not easily derived, since any change in extraction efficiency changes the curve shapes. The initial value of

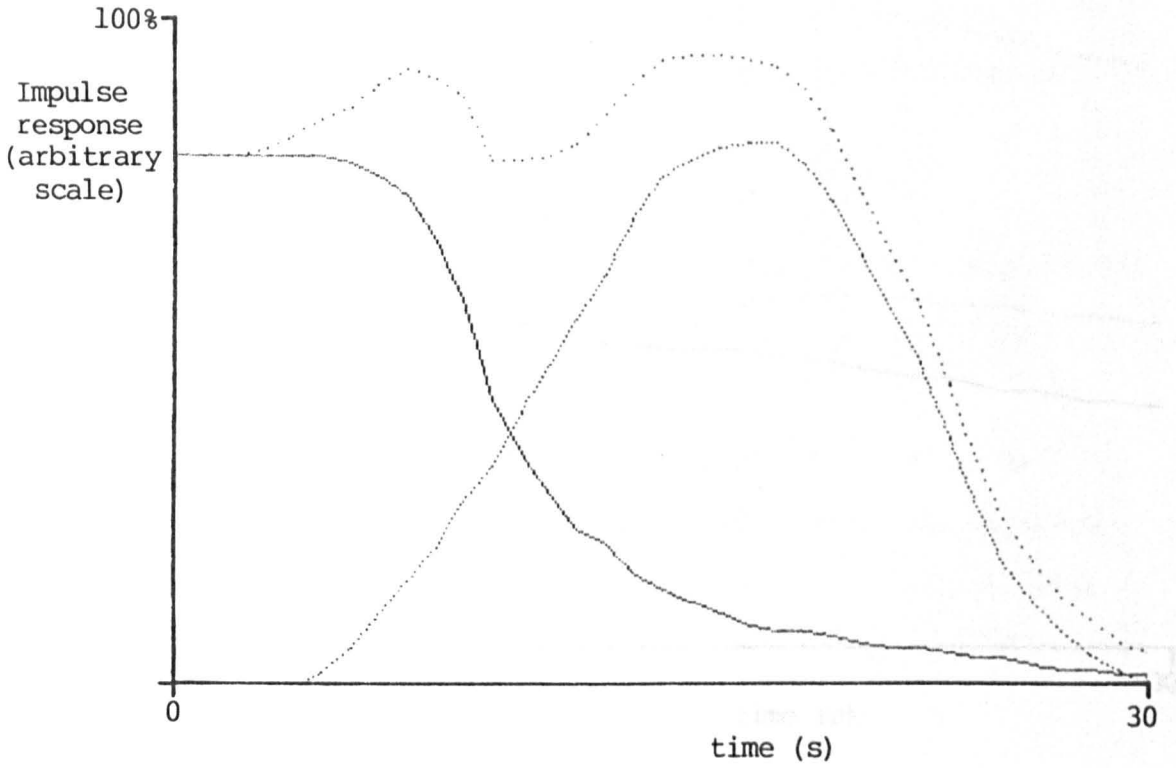

Figure 3.4 Liver blood flow deconvolution, non-extractable tracer. For a non-extractable tracer, deconvolution of an arterial curve from the liver curve produces the impulse response shown by the light dotted curve. This is the sum of the impulse response to an arterial input (solid curve) and a venous input (dotted curve).

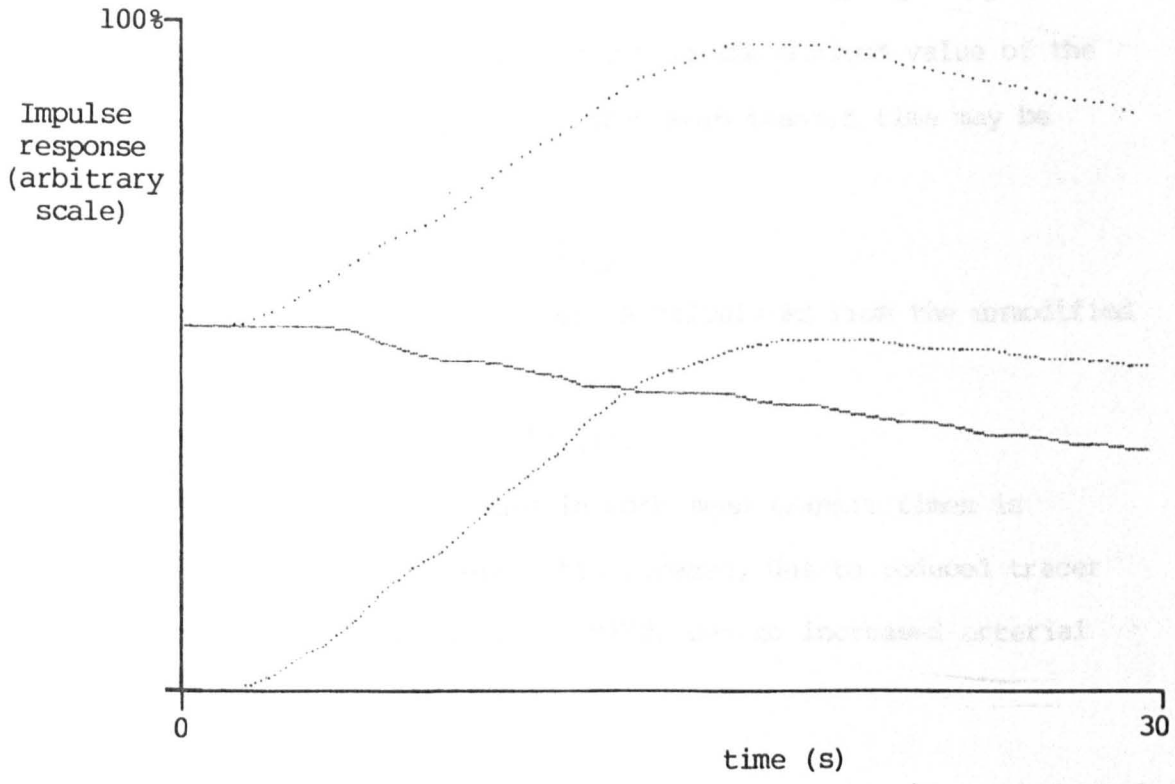

Figure 3.5 Liver blood flow deconvolution, extractable tracer. For an extractable tracer, deconvolution of an arterial curve from the liver curve produces the impulse response shown by the light dotted curve. This is the sum of the impulse response to an arterial input (solid curve) and a venous input (dotted curve).

the sum curve (impulse response) derived from deconvolution of the liver and arterial curves is, as above, proportional to hepatic arterial flow. The maximum height of the curve is related to the portal flow, but is raised by the tracer extracted from the arterial input. The amount of tracer retained by the liver is related to the disease state of the liver, since retention of tracer is decreased by shunting of blood, which increases with disease.

However it is possible to define two mean transit times (MTT1, MTT2), which may be calculated from the sum curve I(j), where j is the frame index. By setting all points prior to the maximum value of the sum curve, I_{max}, equal to I_{max}, the first mean transit time may be calculated as:

$$MTT1 = [\sum_j I(j)]/I_{max}.$$

The second value of mean transit time is calculated from the unmodified sum curve as:

$$MTT2 = [\sum_j I(j)]/I(1).$$

From these definitions, a decrease in both mean transit times is expected in the presence of metastatic disease, due to reduced tracer retention in the liver and also, for MTT2, due to increased arterial blood flow, I(1).

4. Liver perfusion imaging

The different methods of quantitation of relative blood flow via the hepatic artery and the portal vein that were reviewed in Chapter 3 share the same underlying assumptions and are equivalent. Of the studies performed to evaluate the methods, only that of the Leeds group has followed the progression of disease over a long term (Leveson et al, 1985; Cooke et al, 1987), using the 'hepatic perfusion index' (HPI) as defined by Parkin and colleagues (1983).

These data, derived from patients with primary gastrointestinal malignancy, suggest that the HPI may be a useful indicator of those patients harbouring occult metastases at initial presentation. Hepatic metastases develop after resection of the primary colorectal malignancy in 30% of patients (Finlay et al, 1982). It has been suggested that the presence of liver metastases, rather than the local staging of the primary tumour, is more closely related to the long term survival of the patients (Finlay and McArdle, 1986). Since it is assumed that those patients harbouring occult metastases already have micro-metastases at the time of presentation, early identification of these patients enables appropriate management decisions to be made regarding therapy protocols, such as the intra-hepatic arterial infusion of cytotoxic drugs.

In order to measure the HPI a bolus of $^{99}Tc^{m}$-tin colloid is administered and a time-activity curve obtained from the liver. This may be considered as the convolution of an arterial curve with the sum of two impulse responses, the expected shapes of which are shown in figure 3.5. Two mean transit times (MTT1 and MTT2) may be calculated from the sum curve derived from deconvolution of the liver and arterial curves using the definitions in Section 3.5.3(e). From these definitions, a decrease in both MTT1 and MTT2 is expected in the presence of metastatic disease, due to reduced tracer retention in the liver and also, for MTT2, due to increased arterial blood flow.

The aim of the present study was to discriminate between those patients harbouring occult hepatic metastases and those who remain disease free after resection of the primary carcinoma, using data from hepatic blood flow studies.

4.1 Patients

A total of 277 patients with primary colorectal carcinoma was studied (Table 4.1). Of this total, 169 patients were admitted to the study immediately prior to or within 1 month of the resection of the carcinoma (time 0). Ninety four patients were admitted during follow up after resection. Fourteen patients studied had liver metastases at presentation and did not receive resection, for these patients time 0 was defined as the time of diagnosis of the primary disease. Liver perfusion studies were recorded at three to six month intervals following admission to the study. A total of 930 liver perfusion studies were performed.

A clinical diagnosis was established for each patient, independently of the result of the liver perfusion studies, by means of conventional planar liver scintigraphy, abdominal ultrasound and laparotomy at resection. In addition 89 patients had intra-operative ultrasound examinations and 95 patients were examined by X-ray computed tomography. The clinical diagnoses were: (a) normal (no evidence of liver metastases or recurrence of primary carcinoma); (b) local recurrence (of the primary carcinoma); or (c) liver metastases. The times at which liver metastases were first diagnosed (t_{met}) were also recorded.

Table 4.1 Patients with primary colorectal carcinoma

Admission	Clinical diagnosis	Group	Number	
Within 1 month of resection	a normal	1	118	
	c occult metastases	2	9	
	b local recurrence	3	25	
	c overt metastases	4	17	
			Total	169
Later than 1 month after resection	a normal	1	50	
	c occult metastases	2	14	
	b local recurrence	3	11	
	c metastases	4	19	
			Total	94
No resection	c metastases	4	14	
			Grand total	277

A classification of each patient at the time (t) of each liver perfusion recording into one of four diagnosis groups was made, based on the clinical diagnoses. The groups were: (1) normal (i.e. clinical diagnosis (a)); (2) occult metastases (i.e. clinical diagnosis (c) and $t < t_{met}$); (3) recurrence (i.e. clinical diagnosis (b)); or (4) metastases (i.e. clinical diagnosis (c) and $t \geq t_{met}$).

4.2 Imaging and measurement of the hepatic perfusion index

Patients were fasted for 12 hours prior to each HPI study. With the patient supine, a bolus of 80 MBq $^{99}Tc^{m}$-labelled tin colloid was injected into an antecubital vein. As the radiopharmaceutical was administered, a dynamic acquisition of 50 2s frames in a 64*64 matrix was recorded in the 15^{o} right posterior oblique projection. The early frames were examined and the frames in which the lungs and kidneys were best visualised were summed into a single image. Later frames were also summed to show the liver. These images were displayed simultaneously and ROIs defined around the right kidney and over the liver as in the protocol suggested by the Leeds group (Parkin et al, 1983; Leveson et al, 1985). Thus the right kidney ROI enclosed the entire kidney while the liver ROI was defined to exclude all non-liver activity (figure P4.1). A third ROI was also defined over the left kidney (Perkins et al, 1987). When possible the left kidney ROI was defined to exclude all activity from other overlapping organs (figure 4.1). When this was not possible an ROI enclosing the entire left kidney was defined. From each ROI a time-activity curve was generated from the entire raw image data and smoothed once with 1-2-1 weights.

The two kidney curves were displayed and the frame number corresponding to the peak count rate on each curve identified. Care was taken to ensure that the peak count rate corresponded to the renal activity maximum, since frequently the right kidney curve maximum was

due to liver activity within the right kidney ROI. Using the times at which the peak count rates occurred for each of the kidney curves, two linear regression coefficients were calculated from the liver curve. These were the slopes over the four data points (8s) on the liver curve immediately before (slope a) and immediately after (slope b) the peak count rate frame number on each kidney curve (figure 4.2). An hepatic perfusion index was calculated using the peak count rate frame for the right kidney (HPIR) and for the left kidney (HPIL) from the appropriate pair of slopes as HPI = a/(a+b) (Parkin et al, 1983).

The time from half-maximum on the upslope to maximum count rate was computed for each kidney curve (t_h). To exclude the effects of poor bolus injections no value of hepatic perfusion index was recorded for a kidney if t_h for that kidney exceeded 4 frames. Also, no value of HPI for a kidney was recorded if no arterial peak could be identified on that kidney curve.

4.2.1 Deconvolution analysis

The left kidney curve was assumed to have the same shape as the arterial input to the liver, since the left kidney ROI excluded activity from other organs. The frame corresponding to the peak count rate on the unsmoothed left kidney curve was identified and time-activity curves from this frame to frame 50 were generated from the left kidney and liver ROIs. These curves were then smoothed 10 times with 1-2-1 weights. Deconvolution of the left kidney curve from the liver curve was performed and an impulse response curve, I, produced (figure 4.1d,h). From the first 30 points on this curve the mean transit time was calculated in two ways (MTT1, MTT2), using the definitions in Section 3.5.3(e).

Deconvolution analysis was not performed if it was not possible to define the left kidney ROI to exclude activity from overlapping organs.

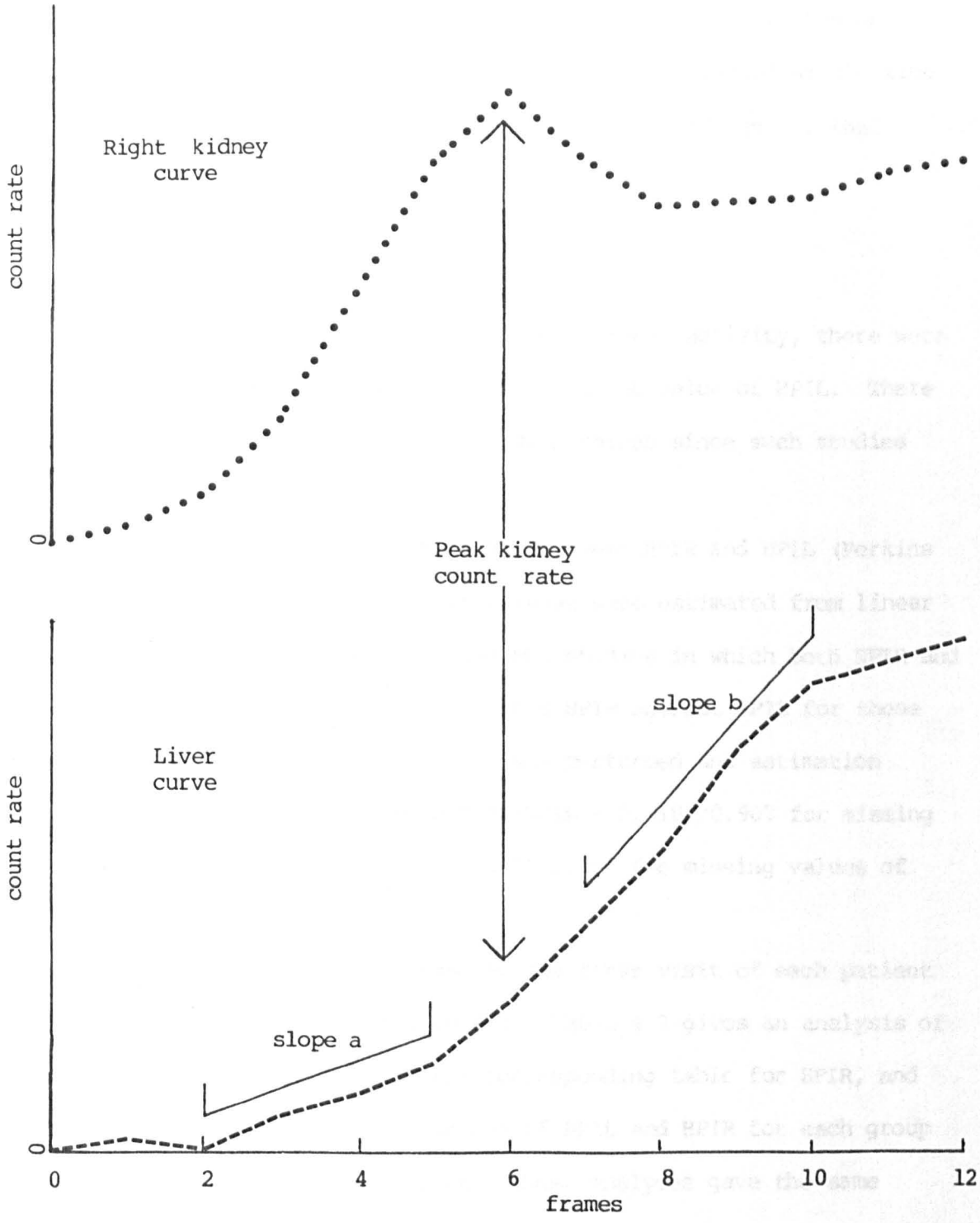

Figure 4.2 Calculation of the hepatic perfusion index (idealized curves). The frame number of the peak arterial flow in the kidney is identified (dotted curve). The two slopes, a and b, are calculated from the liver data (dashed curve) in the four frames (8s) on each side of the peak kidney count rate. Then HPI = a/(a+b).

4.3 Results

Table 4.2 gives a breakdown of the 930 liver perfusion studies recorded by diagnosis group of the patient studied at the time of recording; time of recording; and number of recordings for the patient studied.

4.3.1 Hepatic perfusion index

Due to poor bolus or overlapping liver activity, there were 107 studies with no value of HPIR and 23 with no value of HPIL. There were no studies with neither HPIR nor HPIL values since such studies were not included in the analysis.

In view of the relationship between HPIR and HPIL (Perkins et al, 1987) missing values of either index were estimated from linear regression equations derived from the 800 studies in which both HPIR and HPIL had been recorded. Figure 4.3 plots HPIR against HPIL for those studies. Bivariate linear regression was performed and estimation equations derived. These were HPIR = (HPIL - 0.018)/0.907 for missing values of HPIR and HPIL = (HPIR - 0.072)/0.887 for missing values of HPIL.

The HPIL value recorded at the first visit of each patient is plotted against group in figure 4.4. Table 4.3 gives an analysis of variance table from these data, the corresponding table for HPIR, and also the means and standard deviations of HPIL and HPIR for each group for the first visit by each patient. These analyses gave the same result for both HPIL and HPIR. Using the error mean square to test all pairs of means for each analysis, they demonstrate that the mean HPI of group 4 is significantly higher than the mean HPI of any other group ($p=0.01$), with no other pairs significantly different ($p>0.1$).

Table 4.4 shows the result of classifying patients using the cut-off value of HPIR (0.42) proposed by the Leeds group (Cooke et al,

Table 4.2 Number of patient studies by group and time

Time after resection (months)	Visit number	Group+ 1	2	3	4	Total	Running Total
<1.5	1	118	9	25	31	183	183
	2	1				1	1
<4.5	1	22	4	2	1	29	212
	2	62	6	16	14	98	99
<7.5	1	9	3	2	3	17	229
	2	42	2	4	7	55	154
	3	43	4	8	3	58	58
<10.5	1	6	2	2	2	12	241
	2	9	3	3	2	17	171
	3	38	2	6	6	52	110
	4	24	1	7	2	34	34
<13.5	1	3	2	1	2	8	249
	2	9	1	1		11	182
	3	10	1	2	5	18	128
	4	29		3	4	36	70
	5	6		3	1	10	10
<16.5	1	2		2	1	5	254
	2	5			1	6	188
	3	10		1	1	12	140
	4	14	1	1	4	20	90
	5	18		2	3	23	33
	6	3		2	1	6	6
<19.5	1	3			1	4	258
	2	2	1	1	2	6	194
	3	3		1	1	5	145
	4	3		1	3	7	97
	5	14	1	2	2	19	52
	6	8		1		9	15
<22.5	1	2	1	1	5	8	266
	2	2	1			3	197
	3	4		1	1	6	151
	4	5		1		6	103
	5	9			1	10	62
	6	10		1		11	26
	7	1		1	1	3	3
<25.5	1				2	2	268
	2	1	1		2	4	201
	3	3				3	154
	4	5		1	2	8	111
	5	2		2	1	5	67
	6	5	1		1	7	33
	7	6		1		7	10
	8			1		1	1
>25.5	1	3	2	1	3	9	277
	2	3	2	2	5	12	213
	3	6	3	2	6	17	171
	4	7	2	2	5	16	127
	5	5	2	2	4	13	80
	6	6	1		1	8	41
	7	6		1	2	9	19
	8			1		1	2

+ Group 1 = normal, group 2 = occult metastases, group 3 = local recurrence, group 4 = metastases.

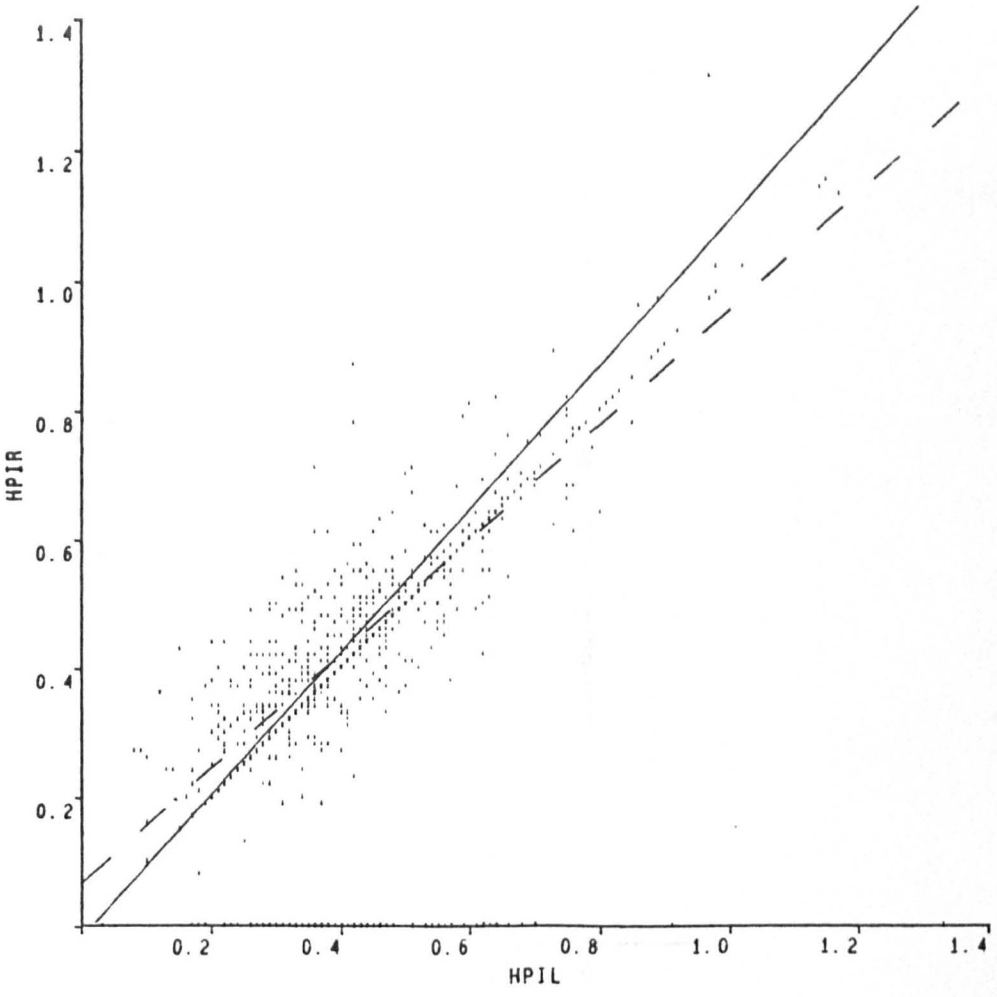

Figure 4.3 Plot of HPIR versus HPIL (800 studies). Solid line represents the estimation equation for missing values of HPIR, dashed line the estimation equation for mising values of HPIL.

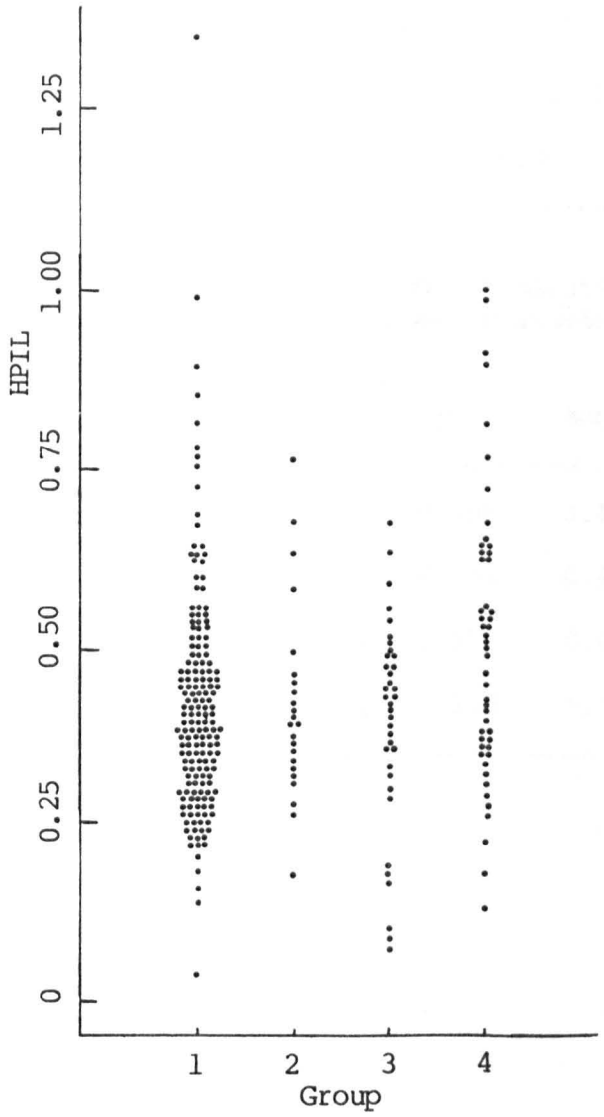

Figure 4.4 HPIL versus group for the first study (277 patients).

Table 4.3 Hepatic perfusion index at the first visit

(i) analysis of variance on HPIL (ii) analysis of variance on HPIR

Source	SS	df	MS	F	P	SS	df	MS	F	P
Group	0.382	3	0.127	4.540	0.004	0.416	3	0.139	4.952	0.002
Error	7.666	273	0.028			7.651	273	0.028		
Total	8.048	276				8.067	276			

(iii) Mean and standard deviation (SD) of hepatic perfusion indices (HPIL, HPIR) and number of studies (n)

Group	n	HPIL Mean	HPIL SD	HPIR Mean	HPIR SD
1	168	0.42	0.164	0.45	0.162
2	23	0.42	0.135	0.43	0.136
3	36	0.39	0.151	0.42	0.154
4	50	0.51	0.200	0.54	0.201

Table 4.4 Classification of patients using hepatic perfusion indices

(i) HPIL

Entries in each column are: number of patients in group with HPIL $\leq$ 0.39
percent group total ($\leq$ 0.39)
number of patients with HPIL > 0.39
percent group total (> 0.39)
total number of patients in group.

	Group 1	2	3	4
$\leq$ 0.39	85	12	16	17
	51	52	44	34
> 0.39	83	11	20	33
	49	48	56	66
Total	168	23	36	50

(ii) HPIR

Entries in each column are: number of patients in group with HPIR $\leq$ 0.42
percent group total ($\leq$ 0.42)
number of patients with HPIR > 0.42
percent group total (> 0.42)
total number of patients in group.

	Group 1	2	3	4
$\leq$ 0.42	83	14	17	13
	49	61	47	26
> 0.42	85	9	19	37
	51	39	53	74
Total	168	23	26	50

1987) and the equivalent cut-off for HPIL (0.39) derived from the estimation equations.

The best sensitivity for detection of occult metastases was 48%, the best specificity 51%, using HPIL, and the best sensitivity for detection of overt metastases was 74%, using HPIR.

4.3.2 Mean transit time

At the first visit, no values of the mean transit times were recorded for 81 of the 277 patients. Figures 4.5 and 4.6 show the values of MTT1 and MTT2, respectively, recorded at the first visit of the remaining patients plotted against group. Table 4.5 gives analysis of variance tables for these data, together with the means and standard deviations of MTT1 and MTT2 for each group for the first visit by each patient. No significant differences were seen between the group means for either of the two mean transit time measurements.

4.3.3 Discriminant function analysis

Since a single measurement of any of the four variables considered above failed to separate normal patients from those with occult metastases, a linear discriminant function was developed for this purpose. A linear discriminant function may be defined as a value, D, for each study such that:

$$D = \sum_{1} c(i).V(i) + \text{constant}$$

where the c(i) are coefficients derived by discriminant function analysis and the V(i) are the values of the measured variables (Norusis, 1985). Since a discriminant function analysis assumes a linear relationship between the measured variables and the classifications chosen, other variables were defined from HPIL, HPIR, MTT1 and MTT2 and also included in the analyses. The discriminant function analyses were performed by means of the SPSS-X software package (Norusis, 1985; SPSS

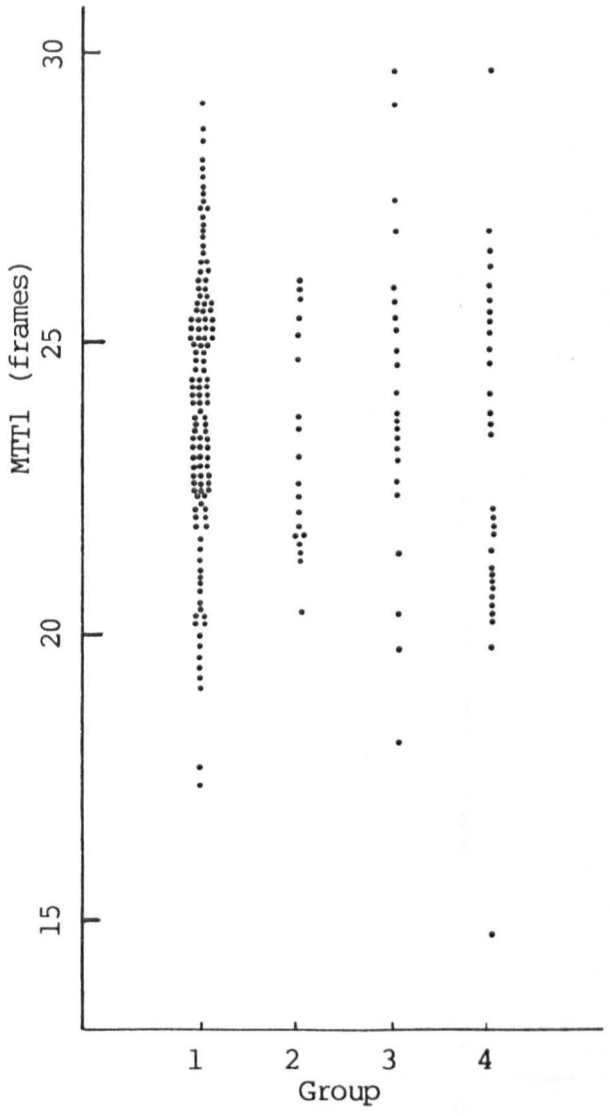

Figure 4.5 MTT1 versus group for the first study (196 patients).

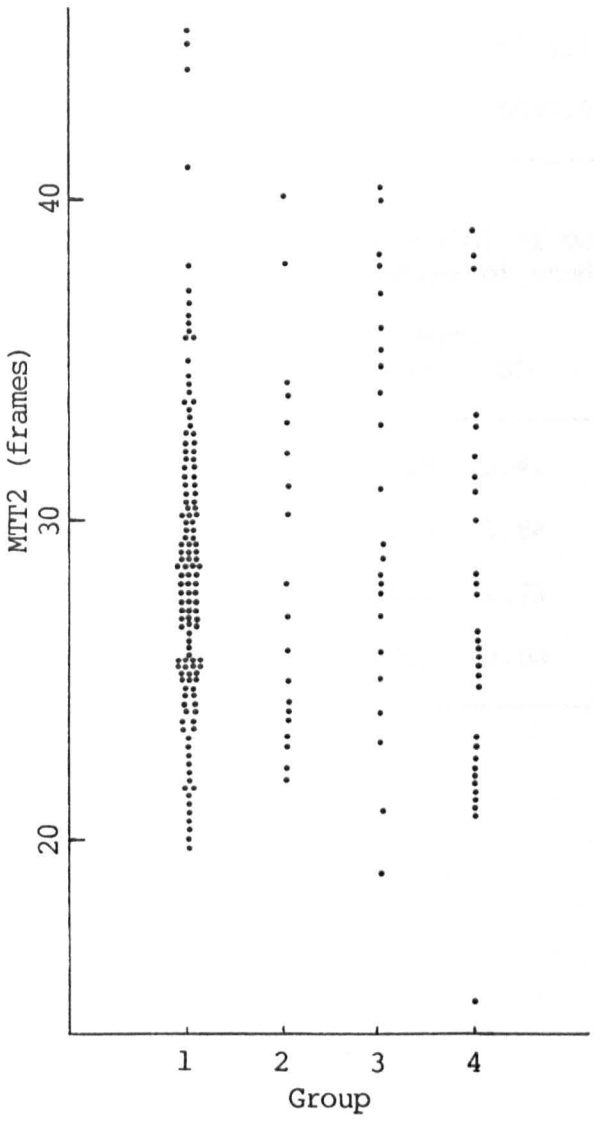

Figure 4.6 MTT2 versus group for the first study (196 patients).

Table 4.5 Mean transit time at the first visit

(i) analysis of variance on MTT1

Source	SS	df	MS	F	P
Group	27.37	3	9.127	1.460	0.227
Error	1200.12	192	6.251		
Total	1227.49	195			

(ii) analysis of variance on MTT2

Source	SS	df	MS	F	P
Group	192.84	3	64.28	2.424	0.085
Error	5505.12	192	28.67		
Total	5697.96	195			

(iii) Mean and standard deviation (SD) of mean transit times (MTT1, MTT2) and number of studies (n)

Group	n	MTT1 Mean	MTT1 SD	MTT2 Mean	MTT2 SD
1	124	23.9	2.41	28.6	5.10
2	19	23.2	1.86	28.4	5.45
3	36	24.1	2.73	30.6	6.07
4	50	23.1	3.00	26.7	5.77

Inc., 1986). Stepwise analyses were used throughout, with maximisation of Wilk's lambda as the inclusion criterion. The objective of the analyses was to derive a function of the variables which, after selection of a suitable cut-off value, would accurately classify a patient into either group 1 or group 2, when evaluated using data from that patient's studies.

For inclusion in the discriminant function analysis the following values were computed from HPIR for each study:

$$AR = 1/HPIR$$

$$BR = HPIR/(1-HPIR)$$

$$CR = 1/BR.$$

Analogous values AL, BL, CL were also computed from HPIL for each study.

In 189 (20%) of the studies mean transit time was not recorded. In order to perform a discriminant function analysis using all data the missing mean transit time values were estimated. Separate multiple linear regression equations for the transit times were derived from HPIR and its derived variables and from HPIL and derived variables. In both cases estimated values of HPIR, HPIL and derived variables were excluded from the analysis. This process was repeated for the following functions of the mean transit times:

$$M1 = 1/MTT1$$

$$M2 = 1/MTT2$$

$$MR = MTT1/MTT2$$

$$MR1 = 1/MR$$

$$MD = MTT2 - MTT1$$

$$MP = MTT1 + MTT2$$

$$MP1 = 1/MP$$

$$PHI = MD/MP.$$

These functions were also used in the discriminant function analysis. The optimal estimation equations were selected on the basis of the

coefficient of multiple correlation (R) and were:

M1 = .04059 + (.00303HPIL) + (.00138BL) + (.00022CL), R = .547;

M2 = .03205 + (.00819HPIL) + (.00141BL) + (.00014CL), R = .501;

M1 = .03242 + (.02078HPIR) + (.00027BR) + (.00111CR), R = .342;

M2 = .02125 + (.03033HPIR) + (.00022BR) + (.00132CR), R = .383.

Since HPIL and derived variables gave the highest values of R these were used for estimation of missing values of M1 and M2. The estimation equations using HPIR and derived variables were used to estimate M1 and M2 when no value of HPIL was recorded. The values of MTT1 and MTT2 were then obtained from the estimates using the equations above, as were the other derived variables MR,..,PHI. Figure 4.7 plots estimated values of MTT1 and MTT2 against measured values of MTT1 and MTT2 for the 741 studies in which these values were measured.

In view of the large number of unrecorded values of mean transit time, and the poor correlations of the estimation equations, the possibility of bias due to estimation was investigated. A variable, mgroup, was defined, with value 0 if mean transit time was recorded or 1 otherwise. Two way analysis of variance was performed, first on HPIR and also on HPIL. For both analyses the main effects were group and mgroup. The analyses are summarised in table 4.6 which also shows the means of HPIR, HPIL for each combination of group and mgroup. The results indicate that the inability to record mean transit time was associated with an increase in hepatic perfusion index. Therefore, the variable mgroup was included in the discriminant function analysis.

In addition to the variables listed above, the slopes of all variables (i.e. rates of change of the variables with time) were computed over sets of measurements made in successive visits of a patient by means of linear regression fitting. These slopes were associated with the most recent of the group numbers for each patient to avoid incorrect classification of patient groups 2 and 4. Variables

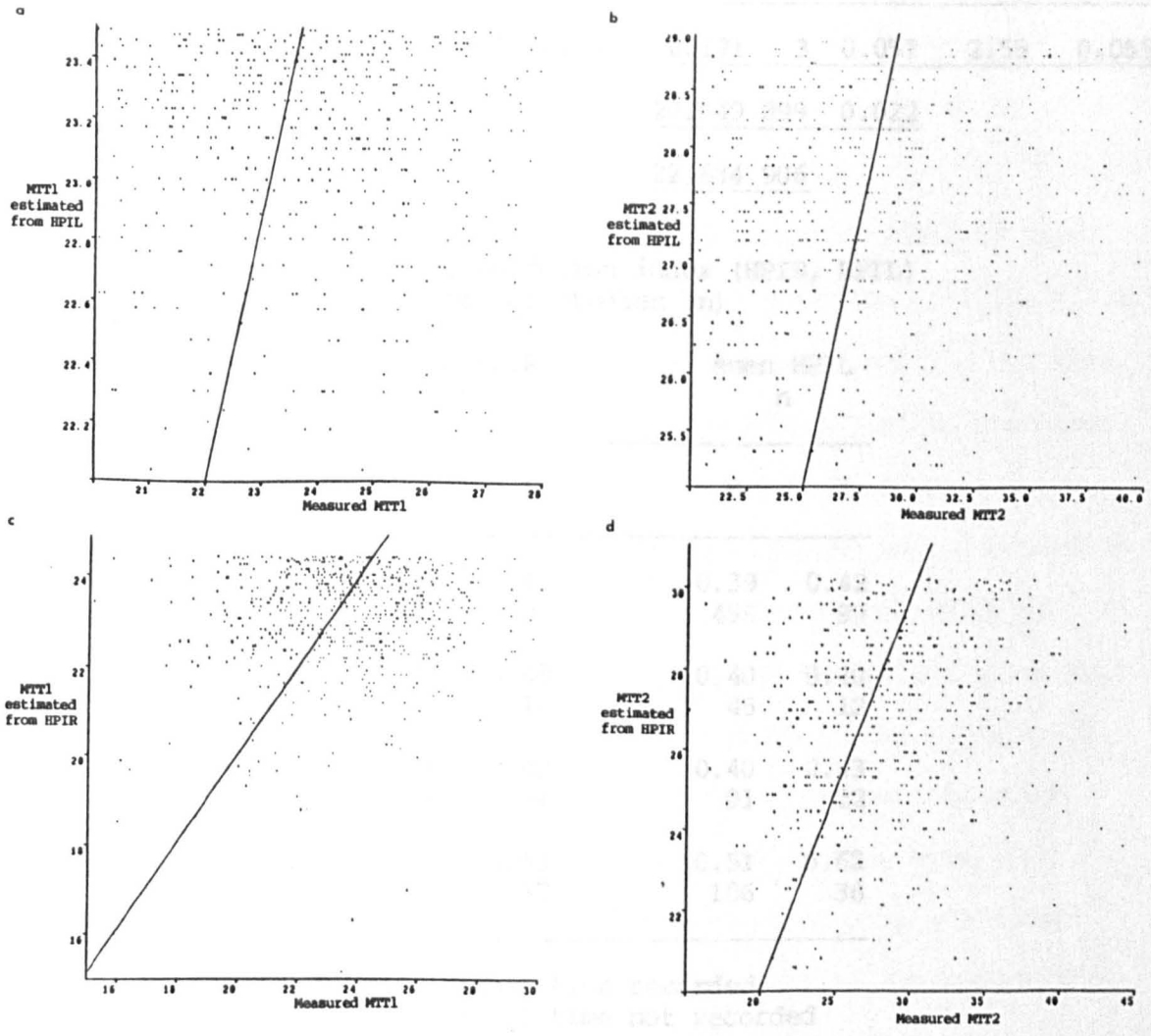

Figure 4.7 Estimated versus measured mean transit time (741 studies). MTT1 = 1/M1, MTT2 = 1/M2. Solid lines represent the line of identity.

a: M1 = .04059 + (.00303HPIL) + (.00138BL) + (.00022CL)

b: M2 = .03205 + (.00819HPIL) + (.00141BL) + (.00014CL)

c: M1 = .03242 + (.02078HPIR) + (.00027BR) + (.00111CR)

d: M2 = .02125 + (.03033HPIR) + (.00022BR) + (.00132CR)

Table 4.6 Effect of missing mean transit time value

(i) analysis of variance on HPIR (ii) analysis of variance on HPIL

Source	SS	df	MS	F	P	SS	df	MS	F	P
Group	1.474	3	0.491	20.953	<.001	2.151	3	0.717	32.148	<.001
Mgroup	0.351	1	0.351	14.982	<.001	0.199	1	0.199	8.918	0.003
Inter-action	0.111	3	0.037	1.575	0.194	0.171	3	0.057	2.55	0.055
Error	19.114	815	0.023			20.049	899	0.022		
Total	21.182	822				22.684	906			

(iii) Mean of hepatic perfusion index (HPIR, HPIL) and number of studies (n)

		Mean HPIR n		Mean HPIL n	
Mgroup =		0	1	0	1
Group	1	0.42 435	0.45 97	0.39 496	0.42 99
	2	0.41 42	0.48 10	0.40 45	0.40 12
	3	0.44 80	0.49 24	0.40 91	0.43 22
	4	0.52 98	0.63 37	0.51 106	0.62 36

Mgroup = 0 : Mean transit time recorded
1 : Mean transit time not recorded

Group = 1 : Normal
2 : Occult liver metastases (not yet diagnosed)
3 : Recurrence
4 : Liver metastases

representing slopes were denoted by the use of the letter B as the last character in the variable name, i.e. HPIRB is a slope of the variable HPIR. The number of successive measurements used in the computation of the slopes, the start time of the fit in relation to the time of resection, and the time interval over which the fit was performed, were investigated in the analyses. The length of the time intervals for fitting was limited by the need to include a sufficient number of studies in group 2 to allow useful estimates of sensitivity to be derived.

The function which gave the best classification was derived from those patients in whom there were two recordings such that (a) the first of the two recordings was within 5 months of resection and (b) the time interval between the two recordings was less than or equal to 6 months. There were 13 studies of group 2 patients which satisfied these criteria. Two additional variables derived from mgroup were included in this function. These were MEL, which was set equal to the value of mgroup for the first of the two recordings, and ME, which was equal to 1 if mgroup for both of the recordings was 1 and 0 otherwise. Table 4.7 gives both the standardized and unstandardized discriminant function coefficients for the variables. The standardized coefficients, s(i), relate to standardized variables, i.e. transformed to have a mean of zero and unit standard deviation, and therefore give an indication of the relative importance of the variables in the discrimination of groups 1 and 2. The unstandardized coefficients, c(i), are used in conjunction with the measured variables to compute the discriminant score, D, for each successive pair of studies in the same patient.

Four time bands (1-4) were defined from the time interval between two recordings (mondif) and from the time after resection at which the

Table 4.7 Discriminant function

Variable Number (i)	Variable Name *	Discriminant function coefficients Standardized s(i)	Unstandardized c(i)
1	MP1	2.494	948.811
2	MP	2.449	0.387
3	HPIR	1.595	12.380
4	HPIRB	-1.346	- 27.538
5	M2B	0.945	250.369
6	CRB	0.695	2.272
7	MEL	-0.682	- 1.707
8	ME	0.681	1.482
9	CONSTANT	-	- 44.341

* derivation of variables:
MP1, MP, HPIR, M2, CR : as text
HPIRB = slope of HPIR (over two successive measurments)
M2B = slope of M2 (")
CRB = slope of CR (")
MEL = 1 if mean transit time estimated on first measurement
= 0 otherwise
ME = 1 if mean transit time estimated on both measurements
= 0 otherwise

first recording was made (mnstrt). These were:

band 1 : mondif > 6 months and mnstrt > 5 months,

band 2 : mondif $\leq$ 6 months and mnstrt > 5 months,

band 3 : mondif > 6 months and mnstrt $\leq$ 5 months,

band 4 : mondif $\leq$ 6 months and mnstrt $\leq$ 5 months.

Therefore, time band 4 corresponds to those studies from which the discriminant function was derived. An analysis of variance was performed on the discriminant function scores from the studies in time band 4 (table 4.8).

This analysis showed that there were significant differences between the groups ($p < 0.001$). Figures 4.8-4.11 show the distribution of discriminant function scores for each group, for the different time bands. From these distributions cut-off values to separate groups 1 and 2 were examined and an optimal value, $D = 0.15$, selected by eye. Table 4.9 shows the results of classifying studies into patient groups, using this cut-off, separately for each time band. For the cases in time band 4 the sensitivity for the detection of occult metastases was 79% and the specificity 67%.

4.4 Discussion

To identify those patients with occult metastases, the best discriminant function found in the analyses required data to be recorded on more than two occasions within six months of each other with the first within five months of the time of resection of the primary malignancy. The inclusion of data derived from the deconvolution analysis of the liver uptake curve was required to derive the function. An examination of the discriminating variables and their standardized coefficients (s) yields results which contradict, in some respects, the assumptions of hepatic blood flow quantitation. First, both MPl (=1/MP) and MP are discriminating variables, with approximately equal s. This

Table 4.8 Discriminant scores (time band 4)

(i) Analysis of variance of discriminant scores by group
(i.e. those studies used in the derivation of the discriminant function)

Source	SS	df	MS	F	P
Group	46.788	3	15.596	12.422	<.001
Error	305.082	243	1.255		
Total	351.870	246			

(ii) Mean and standard deviation (SD) of discriminant score

Group	Mean	SD	Number of studies
1	-0.109	1.033	168
2	1.430	1.139	14
3	-0.049	0.774	36
4	0.793	1.785	29

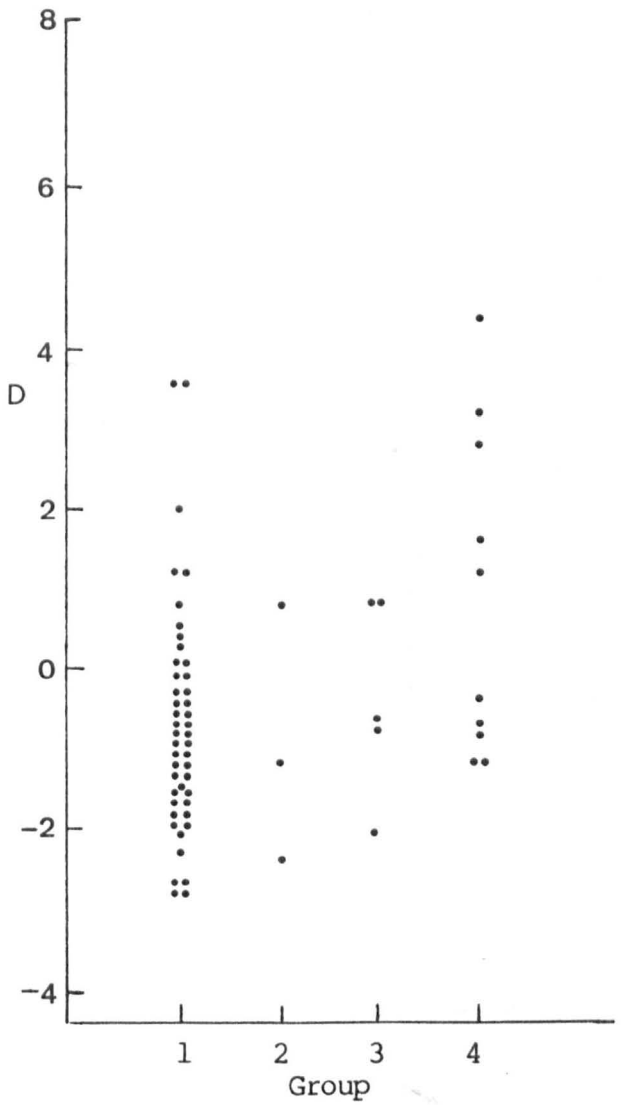

Discriminant function scores (D)
for time band 1

Figure 4.8 Discriminant function score versus group (time band 1).

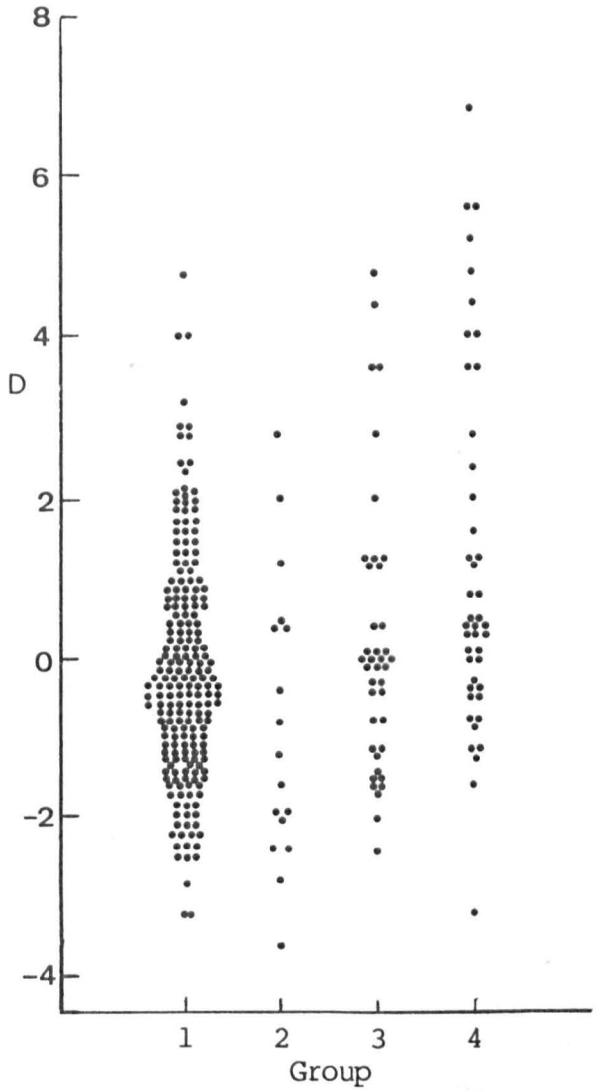

Discriminant function scores (D)
for time band 2

Figure 4.9 Discriminant function score versus group (time band 2).

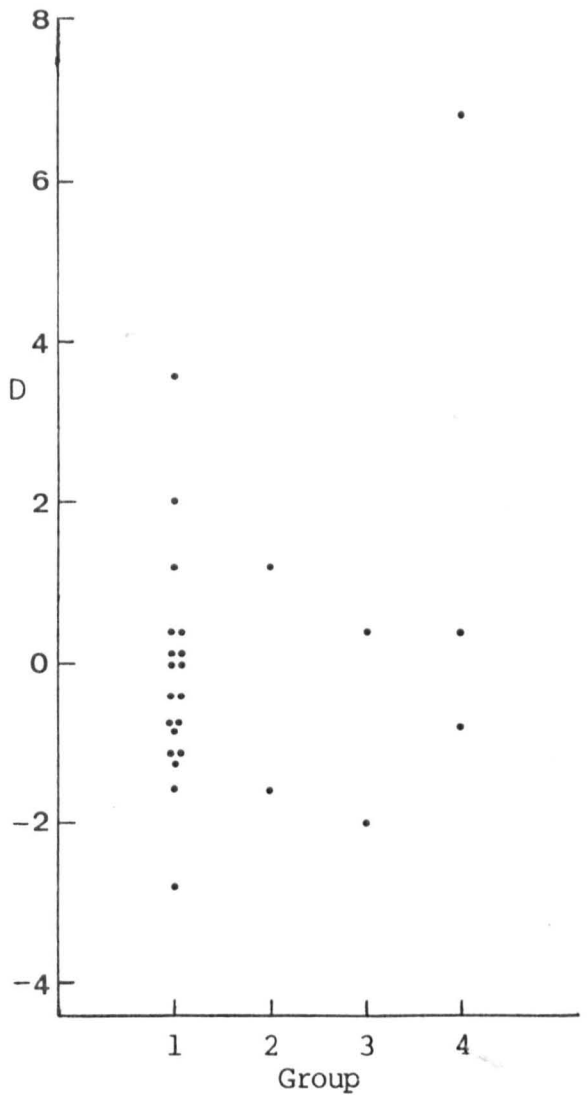

Discriminant function scores (D)
for time band 3

Figure 4.10 Discriminant function score versus group (time band 3).

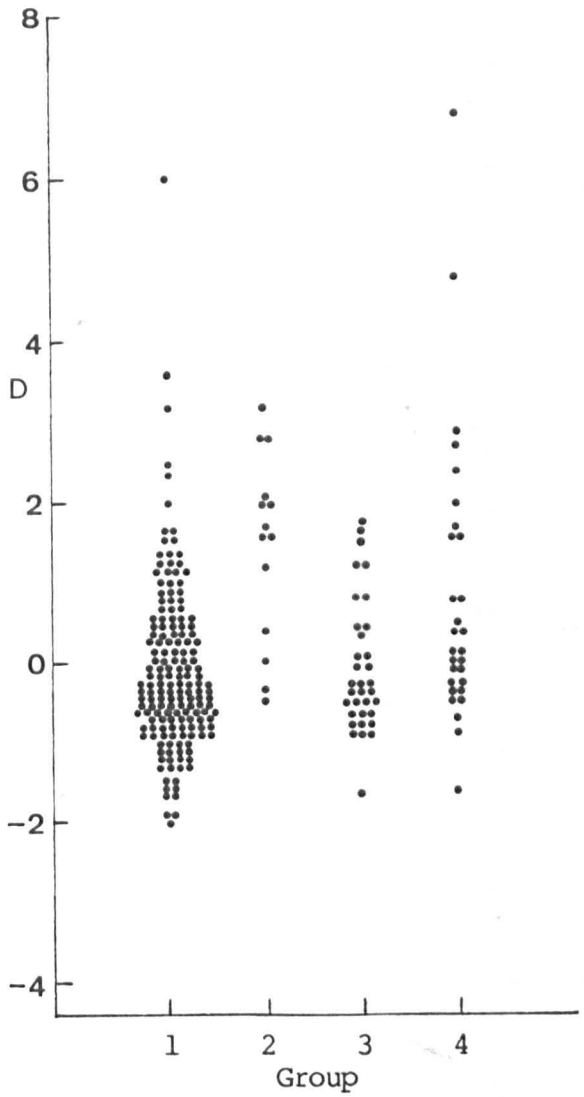

Discriminant function scores (D)
for time band 4

Figure 4.11 Discriminant function score versus group (time band 4).

Table 4.9 Discriminant function score (D)

Entries in each column are : number of studies in group with D≤0.15
percent group total
number of studies D>0.15
percent total
total in group

(i) Time band = 1*

		Group 1	2	3	4
D	≤0.15	36	2	3	5
		78	67	60	42
	>0.15	10	1	2	7
		22	33	40	58
	Total	46	3	5	12

(ii) Time band = 2*

		Group 1	2	3	4
D	≤0.15	129	11	27	18
		63	65	66	37
	>0.15	77	6	14	31
		37	35	34	63
	Total	206	17	41	49

(iii) Time band = 3*

		Group 1	2	3	4
D	≤0.15	14	1	1	1
		74	50	50	25
	>0.15	5	1	1	3
		26	50	50	75
	Total	19	2	2	4

(iv) Time band = 4*

		Group 1	2	3	4
D	≤0.15	113	3	24	14
		67	21	67	48
	>0.15	55	11	12	15
		33	79	33	52
	Total	168	14	36	29

* time bands are defined from mondif = time interval between two studies and mnstrt = time of recording of first study.

Time band 1 : mondif > 6 months and mnstrt > 5 months
Time band 2 : mondif ≤ 6 months and mnstrt > 5 months
Time band 3 : mondif > 6 months and mnstrt ≤ 5 months
Time band 4 : mondif ≤ 6 months and mnstrt ≤ 5 months

suggests that there may be a normal value for the sum of the two mean transit times, with deviations in either direction indicating occult metastases. A possible explanation of this is that when MTT1 and MTT2 are approximately equal, then arterial flow must be high, even when the mean transit time is long. Since a long mean transit time implies little shunting, in such cases the venous outflow of the micro-metastases may pass through normally functioning liver tissue where the colloid is trapped.

The positive contribution of HPIR to the discriminant score accords with the adoption of a single cut-off, values above which indicate the presence of occult metastases. The absence of HPIL from the function simply reflects its high correlation with HPIR and its choice as the estimator variable from which large numbers of mean transit times were derived.

The negative contribution of the slope of HPIR (i.e. HPIRB) to D is unexpected and implies that HPIR begins to fall after resection of the primary tumour in those patients with micro-metastases. A decrease in arterial flow after resection in this patient group is also implied by the positive contribution of the slope of CR (CRB), since CR is the ratio b/a in figure 4.2. However, the positive contribution of M2B implies that decreasing MTT2 is associated with occult metastases. A decrease in MTT2 may arise by reduced colloid retention in the liver or by increased arterial flow. A possible interpretation of the contributions of both HPIRB and CRB to the discriminant score is that decreased arterial flow occurs in micro-metastases during the period following resection of the primary malignancy. With this interpretation, it is reasonable to assume that the positive contribution of M2B is due to reduced colloid retention. This supports the finding that both MP and MP1 contribute positively to D.

The variables MEL and ME are dichotomous variables, with possible

values of 0 and 1, which are derived from mgroup, the variable which indicates whether or not estimation of mean transit time has taken place. Analysis of variance (Table 4.6) showed that the variable mgroup had a fixed treatment effect on HPIR, i.e. HPIR was higher when mean transit time was estimated than when it was measured. A possible explanation for this finding is that estimation of mean transit time took place only when it was not possible to define a region of interest around or within the left kidney entirely free from overlapping liver tissue. The presence of overlapping liver tissue may be taken to imply enlargement of the liver. Such enlargement is often associated with metastatic disease which is in turn associated with an increase in the value of HPIR.

Since MEL and ME may only take the values 0 or 1 the unstandardized coefficients may be used to assess their effects on the discriminant score, i.e. the effects of estimation of mean transit time. When MEL is 1 the effect is to reduce the value of D. For patients without occult metastases reduction in the value of D makes a correct classification more likely, whereas a reduction in D makes a correct classification of occult metastases less likely. When ME is 1, MEL must also be 1 by definition, and, therefore, the net contribution is in the same direction but of smaller magnitude. This suggests that the effect of mean transit time estimation is to reduce the weight given to MP and MPl in the discriminant score, which may be accounted for by the poor correlation between mean transit time and the estimators used (figure 4.7). The effect is small since deviations of MP and MPl are in opposite directions. Assuming patients classified by the discriminant function into group 2 receive intra-arterial cytotoxic drug infusions, the effect of estimation of mean transit time on the treatment received by patients would be to reduce the likelihood of administration of the drugs. This is, therefore, a reasonable outcome.

The discriminant scores obtained in those cases which fell into time bands 1-3 show good specificity but no evidence of successful identification of occult metastatic disease (figures 4.8-4.11, table 4.9). The number of cases in group 2 in time bands 1 and 3 is too low to allow any conclusions to be drawn, but in time band 2 there were 17 cases and a sensitivity of only 35%. This indicates that it is necessary to standardize the time of the first study in order to detect any initial fall in HPI.

The most recent report by the Leeds group (Cooke et al, 1987) indicated that a single measurement of HPIR prior to resection of primary gastrointestinal malignancy, with values >0.42 considered abnormal, gave a sensitivity for the detection of occult metastases of 87% in 31 patients followed for up to 4 years. The corresponding specificity was 67% in 49 patients without metastases. However, the results of the present study suggest that data from studies on two occasions, and including deconvolution analysis, are necessary to attain similar sensitivity and specificity in the classification of those patients with and without occult metastases. This may reflect differences in patient populations admitted to the studies. The distribution of 128 patients with follow up (in the groups used in this study) in the report of Cooke and colleagues was:

1, 36%; 2, 24%; 3, 1%; 4, 39%;

whereas, in the present study, the distribution of the 183 patients studied at the time of resection was:

1, 64%; 2, 5%; 3, 14%; 4, 17%.

These distributions are significantly different ($p \ll .001$, G test of independence). In particular, the lower proportions of patients with metastatic disease suggests that primary malignancies were detected earlier in the disease process in the present study.

In conclusion, a discriminant function has been developed from

hepatic blood flow studies using $^{99}Tc^{m}$-tin colloid on two occasions. The first measurement must be made at the time of, or shortly after, the time of resection of the primary malignancy and the second between three and six months later. The discriminant function then gives a sensitivity for the detection of occult liver metastases of 79%, with a specificity of 67%. The function is of limited value for general use since comparison with the results obtained by other workers indicates that hepatic blood flow study results are sensitive to differences in patient populations.

5.0 The heart

Chapters 6, 7 and 8 of this thesis describe experimental work relating to cardiac nuclear medicine. In Chapter 6 an edge detection algorithm to identify the left ventricular boundary in ECG gated images of the intra-cardiac blood pool is described. In Chapters 7 and 8 the selection of an optimum back-projection filter for myocardial perfusion tomography is described.

This chapter describes the structure and function of the heart and reviews the literature relating to nuclear medicine investigations of the heart.

5.1 Cardiac structure and function

The heart is a hollow organ situated centrally in the mediastinum between the lungs and consisting mainly of muscle tissue, the myocardium. It is conical in shape and normally positioned obliquely behind the sternum with its apex pointing anteriorly downwards towards the left. The size of the average adult heart is approximately 12 cm from apex to base and 8 cm transversely at the broadest part. The weight of the heart varies in males between 280 and 340 g and in females from 230 to 280 g.

The heart is divided into four muscularly-walled chambers, the right and left atria, and the right and left ventricles (figure 5.1a). By rhythmical contractions the heart provides the motive power for the circulation of the blood from the right heart through the lungs into the left heart and from the left heart through the systemic circulation (figure 5.2) and back to the right heart. The myocardium contains specially differentiated muscle fibres which form the conductive system of the heart. A wave of contraction (systole), initiated by electrical stimulation from the sinoatrial node, passes through the atrial walls to the ventricular apex via the atrioventicular node. The

a

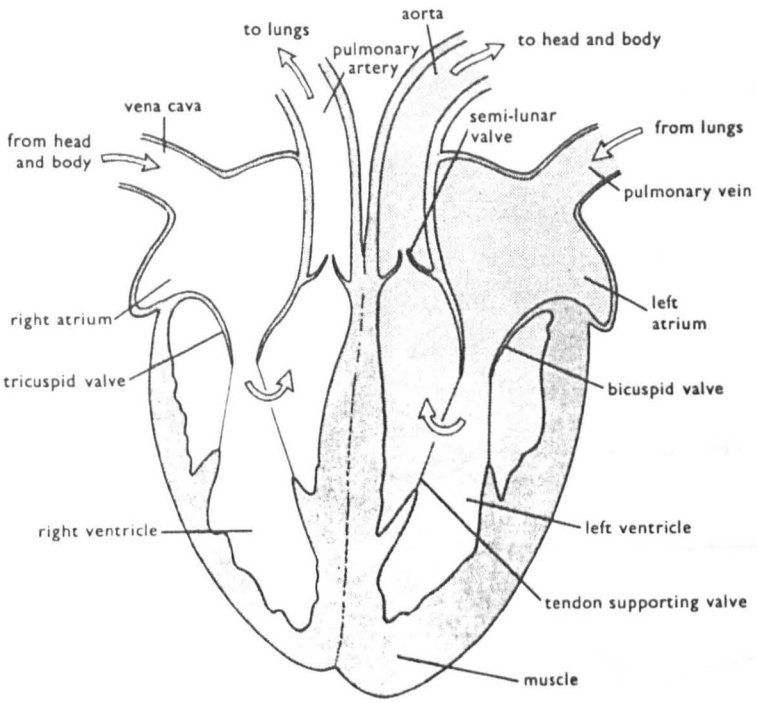

b

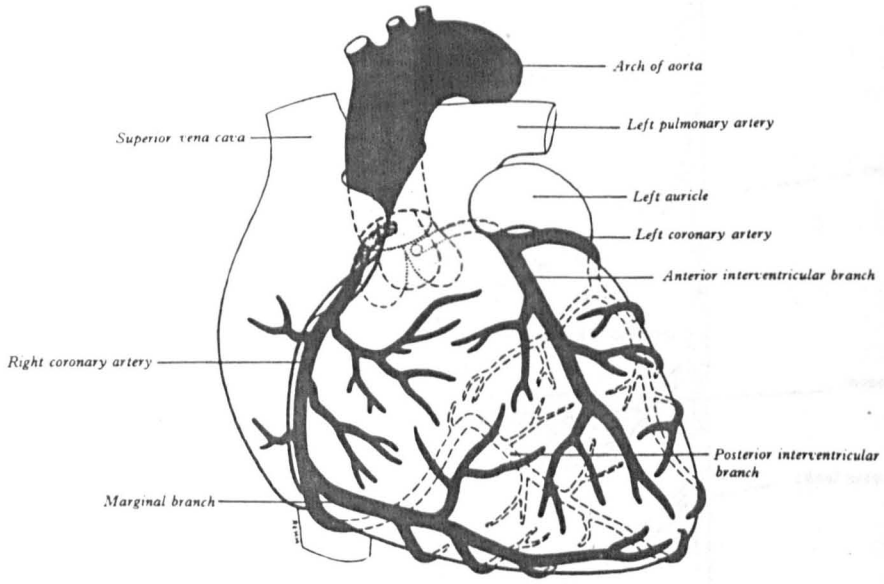

Figure 5.1 The structure of the heart. **a:** The valves and the direction of blood flow (longitudinal section). (Mackean DG, 1973. Introduction to Biology, p99. John Murray, London) **b:** The course and distribution of the coronary arteries. The broken outlines indicate where the aorta and the stems of the arteries are covered anteriorly and where their branches lie on the posterior or diaphragmatic surfaces of the heart. The dotted lines show the origin of the left coronary artery from the upper part of the left posterior aortic sinus. (Gray's Anatomy, 35th. edition, 1973, p618. Longman, Edinburgh)

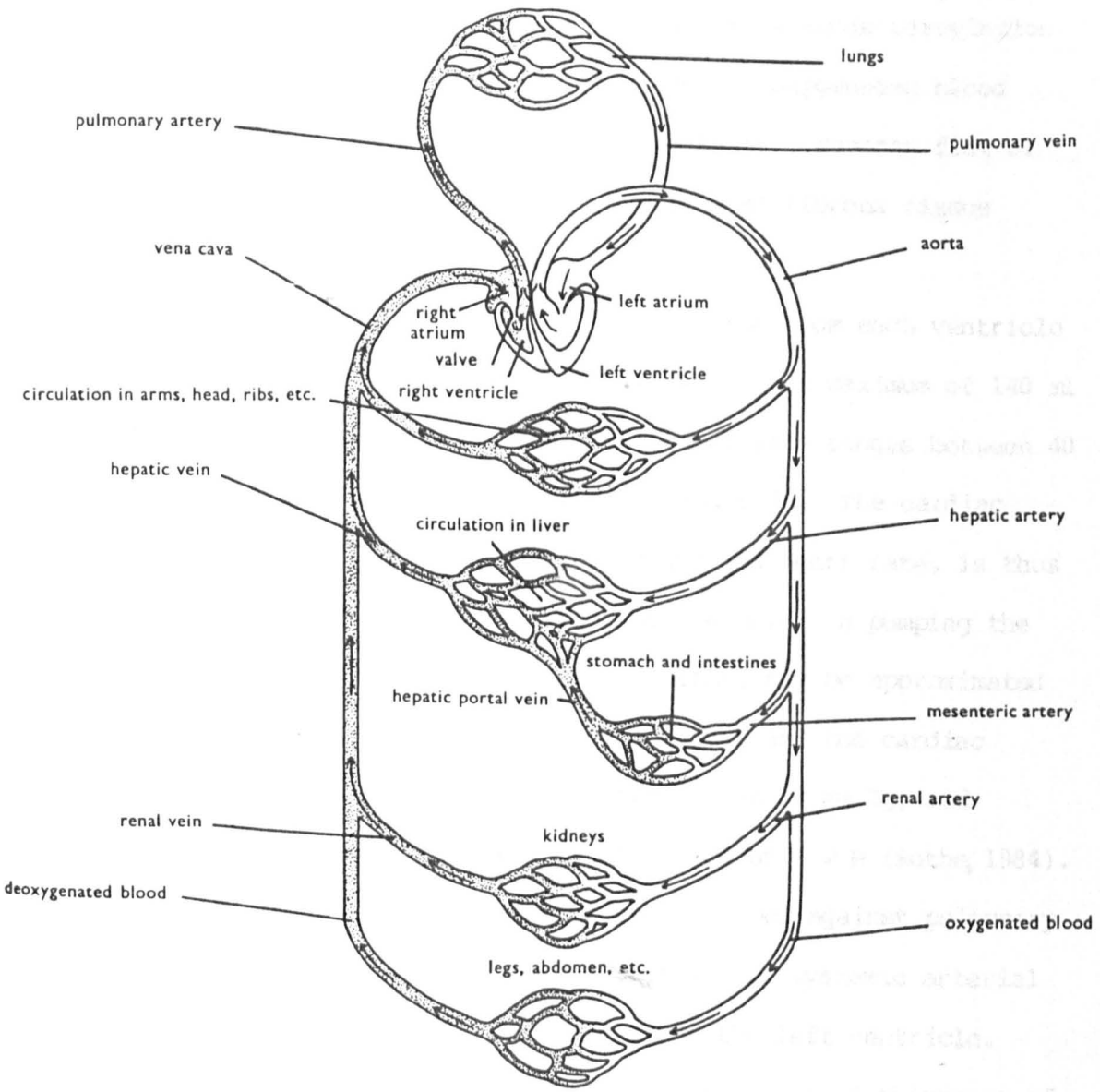

Figure 5.2 Diagram of the circulation of blood (Mackean DG, 1973. Introduction to Biology, p95. John Murray, London).

contraction causes the blood in each atrium to be forced into the corresponding ventricle. Ventricular contraction occurs slightly later and causes the blood in the ventricles to be expelled from the heart, that from the left ventricle passing into the systemic circulation via the aorta while the blood from the right ventricle passes into the pulmonary circulation. The chambers refill during diastole, after the contraction ceases. De-oxygenated blood from the systemic circulation flows through the vena cavae into the right heart, oxygenated blood passes from the pulmonary veins into the left heart. Reverse flow of blood within the chambers is prevented by valves of fibrous tissue (figure 5.1a).

Approximately 80 ml of blood is ejected from each ventricle per beat (stroke volume) when at rest, increasing to a maximum of 140 ml under extreme exercise. At rest, the adult heart rate ranges between 40 and 100 beats per minute, with an average of about 70. The cardiac output, defined as the product of stroke volume and heart rate, is thus approximately 5.5 l min^{-1}. The work done by the heart in pumping the systemic blood, the left ventricular power output, may be approximated by the product of the mean arterial blood pressure and the cardiac output. Typically, mean arterial blood pressure is 95 mm Hg, and therefore the left ventricular power output is about 1.2 W (Rothe, 1984). The right ventricle, pumping the same volume of blood against pulmonary arterial pressure, which is about one seventh of the systemic arterial pressure, performs only one seventh the work of the left ventricle. This difference in power output necessitates the increased thickness of the left ventricular wall compared with the right ventricular wall, as seen in figure 5.1a.

A network of coronary blood vessels on the outside of the heart provides the myocardial blood supply (figure 5.1b). The ability of the myocardium to perform work is limited primarily by the cardiac

oxygen supply, which is determined by coronary blood flow. In humans at rest the coronary blood flow is about 200 ml min^{-1} (about 70 ml per 100 g tissue), which corresponds to 4% of the cardiac output. Experiments in dogs indicate that the flow rate can increase by a factor of nine during severe stress. Sudden occlusion of one of the coronary arteries results in a drop in pressure distal to the occlusion to approximately 30 mm Hg with contractility of the affected myocardium decreasing considerably. Collateral flow is present but is usually low (<10% of normal) and takes several weeks to increase to adequate amounts (Rothe, 1984).

5.2 Cardiac disease

Diseases of the cardiovascular system are the commonest causes of death in England and Wales (table 5.1), a pattern typical for the Western world. Conditions most commonly encountered in cardiac nuclear medicine can be considered in four categories: myocardial disease, congenital flow abnormalities, abnormalities of ventricular performance and valvular disease.

5.2.1 Myocardial disease

Myocardial disease presents as two forms. First, irreversible ischaemia due to sudden occlusion of one or more coronary arteries, often by thromboembolism. This condition is also known as infarction and results in permanent damage to the myocardium in the form of an area of unperfused tissue, which becomes necrotic. Diagnosis of the condition may be made on the basis of clinical history, ECG changes (that is, S-T segment elevation in the first 24 hours followed by T wave inversion), and from a rise in the serum level of creatine kinase isoenzymes in the acute stage of the condition (within 12-24 hours from the onset of symptoms). However, these methods are not sensitive enough

Table 5.1 Mortality in England and Wales, 1987

Cause of death	Male	Female
Total (all causes)	280177	286817
Congenital abnormalities of the heart	728	572
Diseases of the circulatory system : total	132612	138471
Heart disease : total	97279	85266
Rheumatic fever	2	6
Chronic rheumatic heart disease	618	1797
Hypertensive disease	1637	2123
Acute myocardial infarction	56688	43084
Other ischaemic heart disease	30290	25173
Disease of the pulmonary circulation and other forms of heart disease	8044	13083
Non-heart circulatory disease : total	35333	53205
Cerebrovascular disease	26055	43401
Other circulatory disease	9278	9804
Malignant neoplastic disease : total	73557	67211
Disease of the colon	5063	6315
Diseases of the rectum, anus or rectosigmoid junction	3615	2510

Source: World Health Statistics Annual, 1988. WHO, Geneva, 1988.

to detect all cases of mycardial infarction and are insufficiently specific to exclude the large number of patients with non-cardiac causes of chest pain, such as oesophagitis or pleurisy.

The second major form of myocardial disease is coronary artery disease (CAD), which causes angina pectoris. This is due to stenosis of the coronary arteries such that an area of myocardium becomes under-perfused when increased blood supply is required. This commonly occurs in response to exercise stress and is known as transient ischaemia since the local blood supply is restored to its previous level when the extra load on the myocardium is removed. Diagnosis is made from symptomatic history (i.e. anginal chest pain) and S-T depression on exercise. Stenoses can be located by X-ray coronary angiography. Sites of stenosis may be amenable to vascular bypass surgery (coronary artery bypass graft, CABG). Again, diagnosis from history and ECG is neither sufficiently sensitive nor specific, while angiography is an highly invasive technique with a relatively high morbidity, having a complication rate of 4.4% (Harris, 1984).

5.2.2 Congenital cardiac abnormalities

Congenital cardiac abnormalities which lead to a distorted flow sequence are known as shunts. Two common types of shunt are right to left shunts in which flow of blood from the pulmonary into the systemic circulation occurs, and left to right shunts which consist of flow of systemic blood into the pulmonary circulation. Both types of shunt subject the heart to an extra compensatory load, in the first case because of reduced oxygenation of peripheral blood and in the second because fractional venous return of systemic blood into the lungs is reduced. The cause of shunting is the presence of a defect in the cardiac structure such as a ventricular septal defect (VSD), atrial septal defect (ASD) or patent ductus arteriosus (PDA) due to

embryological malformation. Diagnosis is made on the basis of the extent of oxygen saturation of blood samples and clinical history. Defects may be localised by contrast ventriculography or, more usually, by echocardiography. Doppler echocardiography gives further valuable information regarding volume and direction of blood flow.

5.2.3 Ventricular performance abnormalities

Abnormalities of ventricular performance may be due to physical damage to the myocardium, such as described above, to the load conditions imposed on the heart by other disease, or to incorrect timing of ventricular contraction caused by conduction abnormalities. Performance may be investigated indirectly by examining the ECG response to controlled exercise conditions but this requires considerable patient cooperation and gives only limited information. Quantitative estimates of ventricular performance may be obtained by contrast ventriculography following cardiac catheterisation. While catheterisation is relatively simple when examining the right heart, it is not without risk, and is much more difficult when used to examine the left heart since arterial catheterisation is necessary. The studies are performed by recording serial x-ray images, at rapid frame rates, of contrast medium introduced into the chambers of the heart via the catheter. The information from images is quantified by outlining the apparent boundaries of the ventricles at two or more stages in the cardiac cycle (Lewis et al, 1979). Assumptions are made regarding the shape of the ventricular chambers and the volumes of the chambers can then be estimated. Estimates of the mechanical behaviour of the ventricle may then be made. The images recorded may also be examined qualitatively to evaluate the regional behaviour of the ventricular wall during systole. Two-dimensional echocardiographic images may be similarly used to measure performance, again by assuming particular ventricular geometry,

while M-mode echocardiography allows estimation of wall motion.

5.2.4 Valvular disease

Valvular disease which results in regurgitant flow into a cardiac chamber through an incompetent (insufficient) valve may be assessed by contrast ventriculography or echocardiography. Doppler techniques are especially valuable as they allow simultaneous observation of the valvular movements and blood flow.

5.3 Nuclear imaging of cardiac disease

5.3.1 Myocardial imaging

The aim of myocardial imaging is to estimate the extent of myocardial tissue damage caused by local restrictions of blood flow and subsequent infarction or to assess metabolic changes secondary to cardiomyopathy. Additionally it is possible, by means of the dynamic cardiac blood pool imaging techniques described below, to evaluate the effect of disease on cardiac function. Non-invasive imaging of myocardial tissue has been achieved by means of three well-defined mechanisms of radiopharmaceutical localisation: (i) active uptake of metabolic substrates, (ii) binding of antibodies to intracellular proteins, and (iii) active transport of potassium and its analogues via cell membrane bound Na^+-K^+ ATPase. The uptake mechanisms of some myocardial agents are still poorly understood but these radiopharmaceuticals are nevertheless useful. Imaging is of particular value in the demonstration of modified uptake of the radiopharmaceuticals in ischaemic regions (Chervu, 1979; Holman, 1979; Hardy & Wilson, 1981).

Since the left ventricular workload is very much greater than that of any of the other cardiac chambers, the myocardiumm of the left ventricle is thicker than that around the other chambers and, therefore,

only here is uptake normally seen. However, as many of the most severe cardiac disorders are those associated with the left ventricle this is not an important limitation.

(a) Imaging metabolism

The distribution of regional myocardial metabolism may be imaged after the administration of radiolabelled free fatty acids or glucose derivatives. Fatty acids are oxidised by the myocardium under aerobic conditions, and may be labelled with carbon-11 (Weiss et al., 1976) or with isotopes of iodine (Bonte et al, 1973; Robinson & Lee, 1975). Under normal conditions, two-thirds of cardiac energy requirements are met by oxidation of free fatty acids, and so ischaemic regions are seen as areas of reduced uptake. A glucose derivative, 2-deoxy-2-fluoro-D-glucose, may be labelled with fluorine-18 (Phelps et al, 1978). Since glucose is oxidised by anoxic myocardial tissue, areas of the myocardium in which infarction is forming, or which are under-perfused due to angina, show increased labelled-glucose uptake (Schelbert, 1982). Both carbon-11 and fluorine-18 are cyclotron produced positron emitting nuclides (with physical half-lives of 20.3 and 109.7 minutes, respectively). The energy of positron annihilation photons (511 keV) is higher than is optimal for gamma camera imaging, and imaging is normally performed by specialised positron emission tomography (PET) equipment. Therefore, while these agents have been, and will continue to be, valuable tools in cardiac research, they are unlikely to have a place in routine clinical nuclear medicine in most centres for the foreseeable future.

(b) Infarct-avid imaging

All $^{99}Tc^{m}$-labelled skeletal imaging agents accumulate in acute myocardial infarcts (within 7-10 days of onset of symptoms). In

particular, the use of $^{99}Tc^{m}$-labelled pyrophosphate has been widely reported in this context (Bonte et al, 1974; Parkey et al, 1974; Holman et al, 1976). The amount of uptake into damaged myocardium is directly related to the degree of tissue damage, but also depends on the local blood flow since the radiotracer must first reach the site of infarction before uptake can occur. The highest concentration ratios between damaged and normal tissue occur when local blood flow is 20% to 40% of normal (Holman, 1979). As the blood flow decreases further the infarct uptake also decreases. The exact mechanism of uptake has yet to be fully elucidated. Many theories have been postulated, including affinity of the pyrophosphate complex for areas in the site of infarction with elevated calcium concentrations, and increased vascular permeability in the damaged area followed by binding to myocardial cell components (Chervu, 1979).

Infarct volume can be measured from images obtained by emission tomography (Section 2.3). This is of value since there is a relationship between tomographic infarct size and patient prognosis (Holman et al, 1982). Therefore the information gained from the imaging may be used to guide patient management. When SPECT imaging is performed, blood pool imaging at the same session is helpful since although skeletal uptake of the agent is seen this gives insufficient information to locate accurately the position of the infarct within the myocardium.

Antimyosin monoclonal antibody f_{ab} fragments labelled with indium-111 or iodine-131 can be used to demonstrate acute myocardial infarction, since the necrosis attendant upon infarction exposes myosin, a cardiac globulin, to the circulation (Khaw et al, 1976, Khaw et al, 1987). While the radiopharmaceutical is yet to be fully evaluated, it is expected to give images similar to those from $^{99}Tc^{m}$-labelled pyrophosphate without the complication of uptake by overlying bone and

to be more sensitive and more specific, given the uptake mechanism (Khaw et al, 1987).

(c) Imaging perfusion

The assessment of regional myocardial perfusion provides useful information in the detection and localisation of coronary artery disease. Thallium-201-thallous chloride is currently the agent of choice for myocardial perfusion imaging. Thallium ions can be regarded as analogous to potassium ions and are taken up by the Na^+-K^+ pump in functioning muscle. Ischaemic areas of myocardium are seen as areas of poor uptake of thallium, and their positions can be related to the distributions of the coronary arteries (Strauss et al, 1975). Transient ischaemia can be distinguished from infarction by injecting the radiopharmaceutical during stress (e.g. exercise) and recording images immediately and after a period of rest. On the initial images both transient and irreversibly ischaemic areas show reduced uptake. On the later images uptake of thallium may be seen in areas of transient ischaemia, due to reperfusion or reduced washout of thallium, whereas infarcted areas show no change in uptake. The time needed between the early and late images to allow detectable reperfusion of ischaemic myocardium may be as long as 24 hours (Strauss and Fischman, 1989). Quantitation of reperfusion and washout rates improves the sensitivity of the technique (Berger et al, 1981; Watson et al, 1981), as does SPECT imaging (Maublant et al, 1982; Ziada et al, 1986) and ECG gated imaging (Martin et al, 1987). However, the low energy X-ray emissions of thallium-201 are not optimum for gamma camera imaging and the cost and availability of thallium compare poorly with kit-based technetium-labelled radiopharmaceuticals.

For these reasons various technetium-labelled agents are being evaluated as suitable thallium replacements (Holman et al, 1984; Khalil

et al, 1985b; Gerundini et al, 1986; Holman et al,1987). Two of these agents are monovalent hexakis (alkyl isonitrile) technetium cations (figure 5.3). One has tertiary butyl isonitrile groups ($^{99}Tc^{m}$-tBIN), and the second has 2-methoxy isobutyl ether isonitrile groups ($^{99}Tc^{m}$-MIBI). $^{99}Tc^{m}$-tBIN gives a higher uptake in liver, spleen and lungs than $^{99}Tc^{m}$-MIBI, particularly when injected at rest, but only with $^{99}Tc^{m}$-tBIN can transient ischaemia be seen after a single injection (Holman et al, 1986). This is because, while neither agent shows significant myocardial washout, only $^{99}Tc^{m}$-tBIN exhibits significant lung clearance. This redistributing agent may be taken up in areas of reperfused myocardium. To detect transient ischamia with $^{99}Tc^{m}$-MIBI, a second injection with the patient at rest is necessary.

5.3.2 Cardiac blood pool imaging

Cardiac blood pool imaging has three main aims, which are first, the evaluation of changes in cardiac function secondary to myocardial injury or cardiomyopathy, secondly, the diagnosis of disease from observed functional abnormalities, and finally, the evaluation of blood flow abnormalities, either congenital or caused by valvular disease.

The earliest work in the field of nuclear cardiology was performed using external non-imaging scintillation probes to monitor the passage of radiolabelled materials through the heart and lungs (MacIntyre et al, 1952). The probes were connected to chart recorders and time activity curves were produced showing the changing concentrations of radioactivity at the sites monitored by the probes. These curves were similar to those obtained by dye dilution techniques and were used in the same manner to calculate cardiac output, chamber volumes, mean circulation times and shunts (Huff et al, 1957; MacIntyre et al, 1958; Carter et al, 1959; Schreiner et al, 1959; Folse and Braunwald, 1962; Glick et al, 1962; Spach et al, 1965). The principal disadvantage of

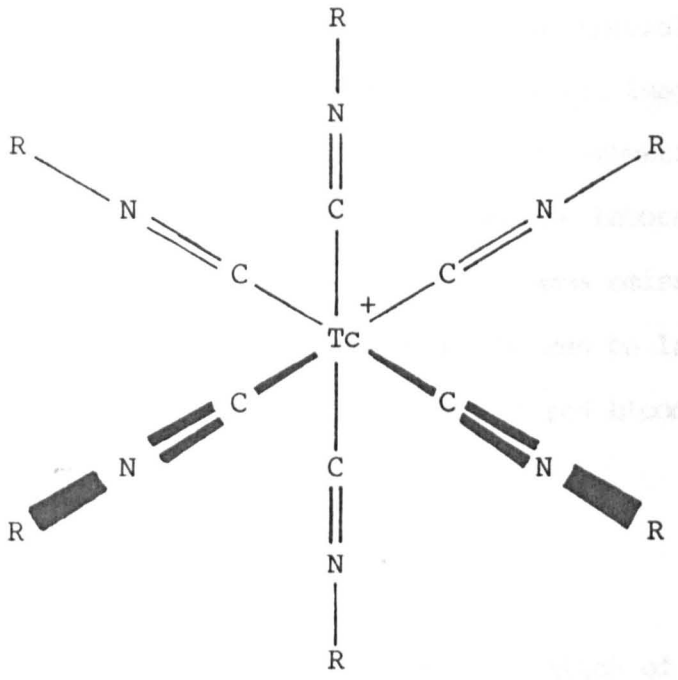

tBIN : R = t-butyl =

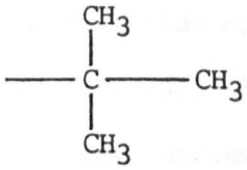

MIBI : R = 2-methoxy isobutyl =

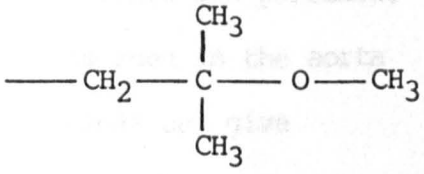

Figure 5.3 Structure of hexakis (alkyl isonitrile) technetium (I) cation.

the probe method was the difficulty of probe positioning. This has been overcome by the use of computer-interfaced gamma cameras, which allow accurate identification of regions for curve generation.

The cardiac blood pool may be visualised by either dynamic imaging of a bolus injection of radiopharmaceutical into a peripheral vein (normally the basilic vein), or by ECG-gated equilibrium imaging. The radionuclide most commonly used for these studies is technetium-99m since it is readily available in most nuclear medicine laboratories, has a short physical half-life (6 hours) and an ideal gamma emission (140 keV) for gamma camera imaging. Technetium-99m can be labelled to human serum albumin ($^{99}Tc^{m}$-HSA) or to the patients' red blood cells ($^{99}Tc^{m}$-RBC) (Holman, 1979).

(a) The analysis of cardiac shunts

(i) Right to left shunts. The detection and evaluation of right to left cardiac shunts is comparatively simple. After peripheral vein bolus injection it is possible, with frame times as long as 2 seconds, to visualise the early arrival of activity in the left side of the heart (Mason et al, 1969; Kriss et al, 1971; Treves et al, 1974). In cases of atrio-septal defect (ASD), activity is seen in the left atrium before or during right ventricular filling, whereas in ventrico-septal defects (VSD) activity is seen in the left ventricle as the lungs are perfused, and in cases of patent ductus arteriosus activity is seen in the aorta as the lungs are perfused. Observations of these kinds can give detailed information regarding the sites of the defects but cannot be used to determine accurately the volumes of shunted blood.

The magnitude of right to left shunts has been assessed by whole body and lung counting after the administration of particulates (such as $^{99}Tc^{m}$-labelled macro-aggregated albumin or albumin microspheres) into a peripheral vein (Gates et al, 1971). These particulates are trapped and

retained by fine arterioles and should, therefore, be almost entirely removed from the blood on the first lung passage. Hence, the activity recorded outside the lung fields can be used to assess the amount of blood passing directly from the right heart to the left. It is normal to estimate the shunt by comparing the ratio of the radioactivity in the head to that in the lungs with a previously established normal range for this value (Thomas et al, 1978). This eliminates the need to measure the whole body counts, which is difficult due to the differing geometries and attenuation characteristics of the different parts of the body and is time-consuming as multiple views may be required to image the whole body with a gamma camera. At the same time comparison with a normal range corrects the results for the small amount of activity normally seen outside the lungs. This activity is, in part, due to shunting within the lungs, even in normal subjects, and also to the distribution of the fraction of the injected activity which is not bound to the large particles.

Although the technique gives an accurate measure of shunted volume, the clinical value is small since, once the diagnosis is established, patient management tends to be guided by blood oxygen saturation data (Treves et al, 1974).

(ii) Left to right shunts. Although the appearance of left to right shunts on first pass blood flow images has been described (Mason et al, 1969; Kriss et al, 1971; Treves et al, 1974), flow from the left heart to the right heart may not always be correctly identified because there may be persistence of activity in the right heart. To evaluate left to right shunts it is necessary to show that recirculation of activity through the lungs occurs earlier than it would in the absence of a shunt, and to quantify the volume of blood seen in this early recirculation. Therefore, time-activity curves of bolus transit through a lung are formed, analogous to those obtained from probe detectors.

They are derived from a region of interest (ROI) positioned over a lung on an image composed of frames approximately 0.5s long.

Using a probe detector system, Folse and Braunwald (1962) calculated the ratio of the count (C_2) at time T_2 after the pulmonary peak activity to the count at the pulmonary peak count (C_1). T_2 was defined equal to T_1, the time between the first appearance of the bolus in the lungs and the pulmonary peak (figure 5.4). The ratio, denoted C_2/C_1 should be small in normal subjects and can be related to the size of the shunt. Unfortunately the technique is an unreliable indicator of shunt magnitude because it is sensitive to prolongation of cardio-pulmonary transit times due to valvular disease (Alderson et al, 1975).

Another technique used to evaluate left to right shunts is based on the knowledge that the area under the first pulmonary peak, extrapolated to the baseline, is proportional to the volume of the pulmonary circulation, Q_p. If this area is measured, and an estimation of the shunt volume, V, is derived from the same ROI, then the ratio of the pulmonary to the systemic flow, Q_p/Q_s, may be calculated (figure 5.5). The method of extrapolation of the pulmonary peak dictates the accuracy of the technique and attempts to fit exponential decay curves (Flaherty et al, 1967; Anderson et al, 1974; Treves et al, 1974; Alderson et al, 1975) to the downslope of the peak have been shown to be inferior to the fitting of gamma variates (Starmer & Clark, 1970; Maltz & Treves, 1973; Askenazi et al, 1976).

Gamma variates are curves of the form:

$$C(t) = k.(t^a).\exp(-t/b) \qquad 5.1$$

where C(t) is the count rate at time t, and k,a and b are arbitrary parameters determined by the fitting process. The use of gamma variates has proved successful because the fitting process makes use of data from the upslope of the pulmonary peak as well as the early downslope and,

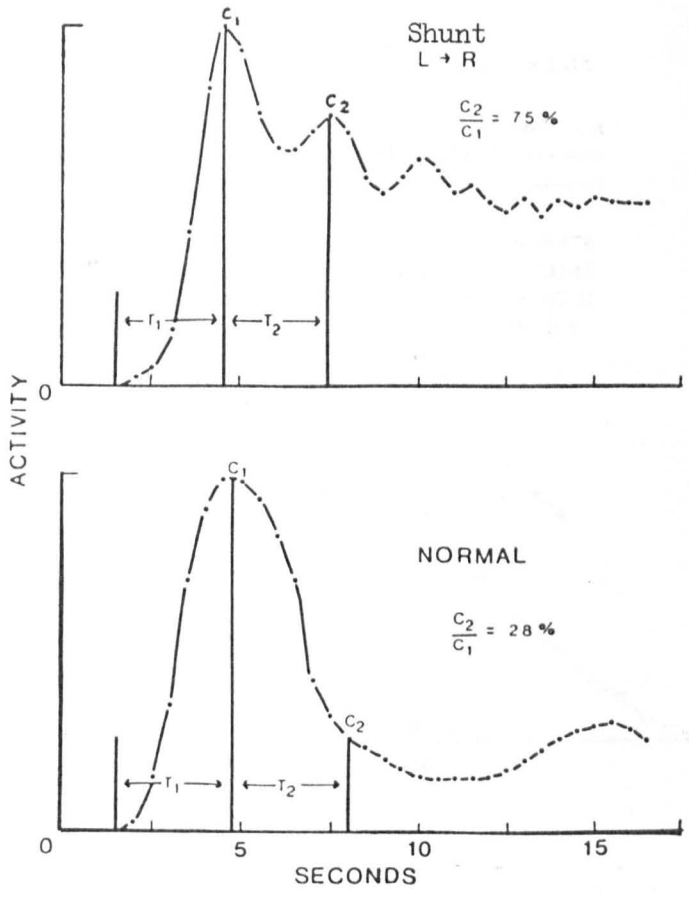

Figure 5.4 Shunt quantitation by C_2/C_1 ratios. C_1 is the peak count on the pulmonary curve. T_1 is defined as the time between first appearance of activity and the peak. T_2, the same time interval as T_1, is measured from the time of peak activity. C_2 is the count at $T_1 + T_2$ after the first appearance of the activity. (Treves et al, 1974)

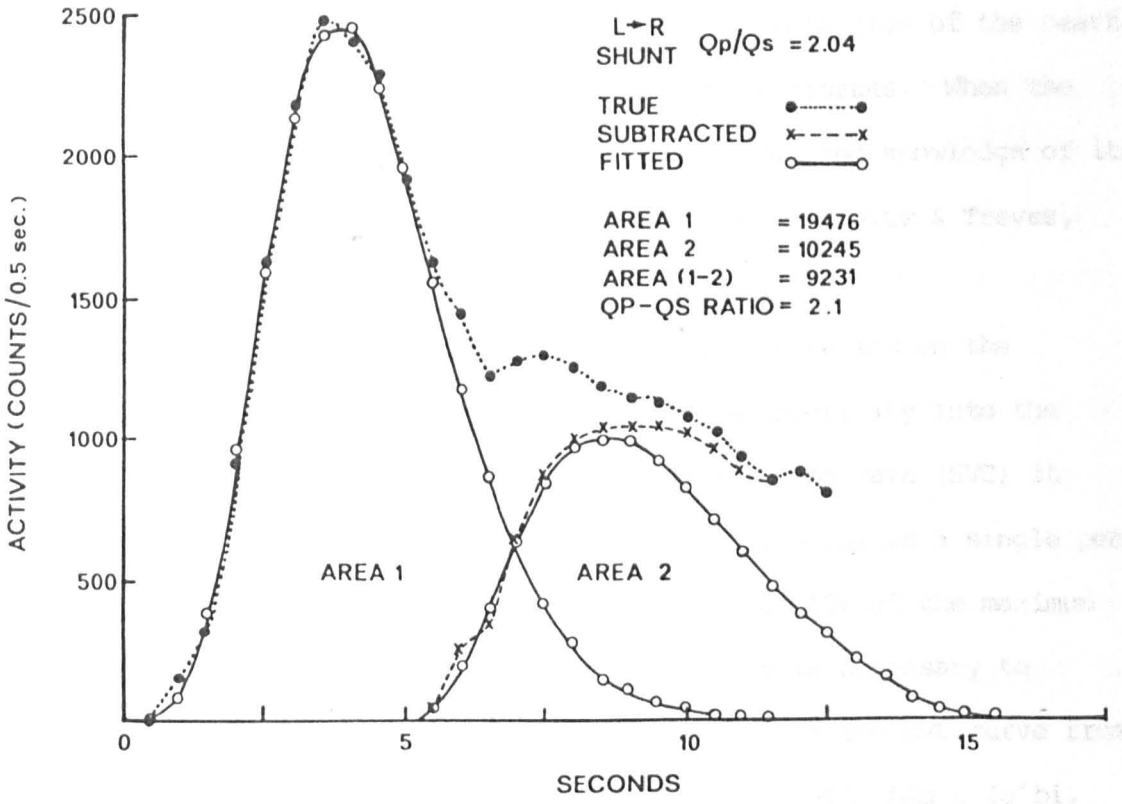

Figure 5.5 Estimation of the Q_p/Q_s ratio by means of the gamma function. A gamma function fitted to the pulmonary peak gives Area 1 (A_1). This function is subtracted from the original data and a second function fitted to the remainder gives Area 2 (A_2). Then Q_p A_1; and the shunt volume, V A_2; with the same constant of proportionality. Since $V + Q_s = Q_p$, $\frac{Q_p}{Q_s} = \frac{Q_p}{Q_p - V} = \frac{A_1}{A_1 - A_2}$ (Maltz and Treves, 1973).

therefore, gives a satisfactory fit. Comparison with values derived by oximetry at catheterization has shown good agreement when the value of Q_p/Q_s is in the range 1.2 to 3.0 (i.e. when the pulmonary circulation is 1.2 to 3.0 times the systemic circulation), particularly when the shunt is at the ventricular rather than the atrial level (Baker et al, 1985). Values of Q_p/Q_s between 1.0 and 1.2 have no clinical significance since the calculated value is an over estimate because the lungs have a blood supply (bronchial circulation) derived from the left side of the heart and there are counts derived from overlying soft tissues. When the Q_p/Q_s value is greater than 3.0 the shunt is large and knowledge of its exact value is not critical for patient management (Maltz & Treves, 1973; Treves et al, 1974; Askenazi et al, 1976).

Accurate area ratio quantification of shunts relies on the administration of a single compact bolus of radioactivity into the heart. By positioning an ROI over the superior vena cava (SVC) it should be possible to derive a curve showing the bolus as a single peak. When this peak is wider than 2.5 seconds between 10% of the maximum count on the upslope and 10% on the downslope it is necessary to compensate for the bolus spread by deconvolution of the SVC curve from the lung curve (Alderson et al, 1979; Ham et al, 1981; Lis & Zu'bi, 1982; Kuruc et al, 1983). Break up of the bolus, seen as multiple peaks on the SVC curve, can result from injections into the cephalic vein or from poor peripheral venous circulation. This effect can be corrected for by the application of the 'bolus cleaning' technique of Lis and Zu'bi (1982).

(b) Ventricular volume and ejection fraction

Radionuclide blood pool imaging of the heart provides essentially the same information as x-ray contrast ventriculography about the function of the ventricles. The principal advantage offered by

radionuclide imaging is that it is relatively non-invasive, involving only an intravenous injection, whereas contrast ventriculography cannot be performed without cardiac catheterisation. Radionuclide imaging may be performed either by first pass studies, with frame rates of the order of 40ms, or by multi-gated equilibrium blood pool acquisition (MUGA) (Schelbert et al, 1975; Ashburn et al, 1978; Holman, 1979). MUGA images of the heart are recorded by allowing the radiopharmaceutical to equilibrate in the circulation, and then acquiring frames, each about 40 ms long. Data acquisition is initiated by a signal generated by the patient's ECG R wave and must satisfy the condition $n.t \leq RR$, where n is the number of frames per beat, t the time per frame and RR the beat length. By repeatedly triggering on the R wave, images are recorded, with typically 16 to 32 frames, over several hundred heart beats (figure P5.6). The composite images produced have much greater count densities than can be given by first pass imaging.

When patients' heart rates vary, it is normal to exclude from the acquisition those beats whose lengths differ from the average by more than a predetermined time. However, Kalff et al (1982) have shown that measures of ventricular function are not significantly altered during ectopic beats.

MUGA imaging allows the imaging of the heart in many projections after a single dose of radiopharmaceutical, and thus produces more information on wall motion in different directions than is possible with first pass blood flow studies. This is because only a limited number of first pass studies using technetium-99m can be recorded at one visit by a patient, as circulating activity builds up to an unacceptable level and interferes with later studies. The long half-life of technetium-99m compared with the time taken to record a first pass flow study restricts the number of studies using $^{99}Tc^{m}$-labelled radiopharmaceuticals to a maximum of two per day (Holman, 1979). Other short lived radionuclides

such as tantalum-178 (Neirinckx et al, 1978; Holman et al, 1979) and gold-195 (Dymond et al, 1982a; Elliott et al, 1983) have been used for rapid sequential studies but high costs have restricted their use.

A disadvantage of MUGA studies is that there is no separation in time of the image of right and left heart, as there is in a first pass study. Since no positioning of gamma camera and patient will allow visualisation of the cardiac chambers without overlap, this means that some part of the image is always degraded by cross-talk when performing equilibrium studies. The amount of cross-talk must be minimised by careful positioning of camera and patient. On the other hand it is possible to perform a first pass study with $^{99}Tc^{m}$-RBC or HSA, wait for the activity to equilibrate, and then perform MUGA studies.

First pass and MUGA studies have been analysed by measuring areas in the images (as with images obtained by contrast angiography) to derive left ventricular volumes and ejection fractions (Mullins et al, 1969). However, time-activity curves may be dervied from ROIs over the left ventricle and it is more accurate to calculate the ejection fraction from the count rates rather than areas. Correction of the time-activity curve for radioactivity in the myocardium and overlying tissues within the ROI is required (background subtraction) and the assumption is made that the left ventricular count rate at any time is proportional to left ventricular blood volume. Many studies have shown this assumption to be valid (Van Dyke et al, 1972, Dymond et al, 1979; Van Aswegen et al, 1980; Harpen et al, 1983).

The left ventricular blood volume at end diastole (LVV_{ed}) and the end systolic volume (LVV_{es}) are given by:-

$$LVV_{ed} = k_{LV} \cdot LVC_{ed} \qquad \}5.2$$
$$LVV_{es} = k_{LV} \cdot LVC_{es}$$

where LVC_{ed} and LVC_{es} are the maximum and minimum count rates, respectively, on the background-corrected left ventricular time-activity

curve. The value of the constant k_{LV} is dependent on the activity per unit volume of blood, on the sensitivity of the system and on the attenuation of the radiation within the patient. It is assumed that these factors remain constant during the cardiac cycle and thus it follows that the left ventricular ejection fraction is given by:

$$LVEF = (LVC_{ed} - LVC_{es}) \; / \; LVC_{ed} \qquad 5.3$$

This value has been shown to correlate well with the quantitative results from contrast angiocardiography (Parker et al, 1972; Van Dyke et al, 1972; Marshall et al, 1977; Bianco & Schafer, 1978; Borer et al, 1978; Jengo et al, 1978; Dymond et al, 1982b; Kalff et al, 1982). For MUGA studies the LVEF can be calculated directly from the left ventricular time-activity curve, but in the case of first pass studies there are slight differences in the method. These arise because the left ventricular phase of a first pass study contains counts from several heart beats with high variability of counting statistics in each. It is therefore usual to average the estimate over a few beats, or to fit smooth curves to the original data, in order to reduce the effect of random noise.

The true volume of blood in the left ventricle may be established by normalisation of left ventricular activity for activity per unit volume of blood, in order to correct for variations in the size of the administered dose and the size of the vascular volume. However, this normalisation is not normally performed because of the requirement for blood sampling and equipment calibration.

In order to compute the LVEF accurately it is necessary to record MUGA and first pass images in such a way that a left ventricular ROI may be defined without overlap with the activity in other cardiac chambers. For MUGA using a parallel hole collimator, a 30^{o}-45^{o} left anterior oblique (LAO) projection, modified by 15^{o} caudal tilt, gives the required isolation of the left ventricle from the right ventricle and

left atrium in most patients, and this is the projection used for the images in figure 5.6. Similar MUGA images may be produced using the same projection with a 30^{o} caudal slant hole collimator and no caudal tilt. In first pass imaging, since there is time separation of the left and right ventricular activity, almost any projection from left posterior oblique (LPO) through LAO to right anterior oblique (RAO) will provide suitable images, so long as caudal tilt is applied in the LAO projections to separate the left ventricle and left atrium. The use of anterior or RAO projections is common when only a single view is recorded and has the advantage that lung ROIs may easily be defined if shunt evaluation is required.

The assumption that ventricular volume is proportional to counts recorded can be equally well applied to the right ventricle as to the left ventricle, (Van Dyke et al, 1972; Berger et al, 1978; Tobinick et al, 1978; Harolds et al, 1981; Sorensen et al, 1982). By analogy with equations 5.2 and 5.3 the right ventricular end diastolic and end systolic volumes are given by:

$$RVV_{ed} = k_{RV}.RVC_{ed} \qquad \}5.4$$

$$RVV_{es} = k_{RV}.RVC_{es}$$

and right ventricular ejection fraction:

$$RVEF = (RVC_{ed} - RVC_{es}) \; / \; RVC_{ed} \qquad 5.5$$

where k_{RV} is assumed to be constant, RVC_{ed} is the maximum value on the right ventricular time-activity curve and RVC_{es} is the minimum value on that curve. However, because of the relative positioning of the chambers of the heart, it is difficult to define a right ventricular ROI on a MUGA image which does not overlap other cardiac chambers, particularly the right atrium. This overlap can be partially overcome by defining different ROIs for end systole and end diastole (Maddahi et al, 1979), by the use of a 30^{o} caudal slant hole collimator (Gandsman et al, 1981), or by the use of parametric images, such as the Fourier

amplitude image, to aid in the definition of the ventricular ROIs and to estimate the ventricular stroke volumes (Makler et al, 1983).

(c) Regurgitant blood flow

The regurgitation of blood into a cardiac chamber due to incompetent (insufficient) valves can be treated surgically. The appearances of both first pass and MUGA images in the presence of regurgitant flow have been reported (Burke et al, 1968; Burke et al, 1969; Mason et al, 1969; Treves et al, 1970; Matin and Kriss, 1970; Kriss et al, 1971; Mishkin and Mishkin, 1974; Lumia et al, 1981). These appearances depend on the severity of the insufficiency and the duration of the condition. The usual appearance is of dilation of the chamber into which the regurgitant blood is flowing. In addition, the longer that mitral insufficiency remains untreated the more likely it is that, due to pressure increases in the left atrium, the left ventricle will also dilate, resulting in volume overload. However, visual assessment of the images gives scant information regarding the volume of regurgitant blood and it is knowledge of this volume which determines patient management. Therefore methods have been described to evaluate regurgitation quantitatively (Kirch et al, 1974; Baxter et al, 1980; Sorenson et al, 1980).

The volume of blood ejected by a chamber, per beat, is known as the stroke volume (SV) and is the sum of the blood volume which leaves the chamber and is not regurgitated (forward stroke volume, FSV) and the blood volume which is ejected and is then regurgitated (regurgitant flow, RF).

ie. $SV = FSV + RF.$ 5.6

Since the forward stroke volumes of all chambers must be equal then, by subtracting the stroke volume of a chamber with non-regurgitant valves (ie RF=0) from the stroke volume of another chamber, the regurgitant

flow in the second chamber is obtained. By measuring the volume of left and right ventricles at end systole and end diastole, using the methods outlined above, it is possible to derive the stroke volumes of these chambers since:

SV = (End diastolic volume) - (End systolic volume) 5.7

Therefore, it is possible to compare the stroke volumes of the left and right ventricles and, if it is known that one ventricle has normal valves, to evaluate the regurgitant flow in the other. When the left ventricular stroke volume (LVSV) is greater than the right ventricular stroke volume (RVSV) then the regurgitant flow is due to either mitral valve incompetence (between the left ventricle and the left atrium), or aortic valve incompetence (between the aorta and the left ventricle). Similarly, if RVSV > LVSV, regurgitant flow is between either the pulmonary artery and right ventricle, through the pulmonary valve, or the right ventricle and right atrium, through the tricuspid valve.

Knowledge of the values of the factors k_{LV} and k_{RV} in equations 5.2 and 5.4 is required to evaluate the true stroke volume. To obtain these values requires calibration with blood samples, and therefore it is usual to estimate the regurgitant flow by determining a 'regurgitant index'. This has been defined as follows:-

regurgitant index, RI = LVSC/RVSC 5.8

where LVSC = left ventricular stroke counts $= LVC_{ed} - LVC_{es}$ 5.9

and RVSC = right ventricular stroke counts $= RVC_{ed} - RVC_{es}$ 5.10

(Rigo et al, 1979; Gandsman et al, 1981; Lam et al, 1981; Taylor et al, 1982). It follows directly from equations 5.2, 5.4 and 5.7 that the ratio of the stroke volumes of the left and right ventricles (LVSV and RVSV), which is known as the regurgitant ratio, is:

$$\begin{aligned} LVSV/RVSV &= k_{LV}.(LVC_{ed} - LVC_{es}) \;/\; k_{RV}.(RVC_{ed} - RVC_{es}) \\ &= RI.(k_{LV}/k_{RV}) \end{aligned} \quad \} 5.11$$

Then, by assuming that the ratio k_{LV}/k_{RV} is a constant value for all

patients it follows that RI is proportional to regurgitant ratio (equations 5.8, 5.9, 5.10 and 5.11).

The normal value of RI (i.e. k_{RV}/k_{LV}) is system dependent and must be estimated for the particular instrument configuration in use. Values of RI for patients without regurgitation give a measure of k_{RV}/k_{LV} and have been reported (mean, SD) as 1.5, 0.15 (Rigo et al, 1979); 1.3, 0.2 (Taylor et al, 1982) and 1.06, 0.05 (Gandsman et al, 1981). This last result was obtained using 30^{o} caudal slant hole collimation and reflects the improved right ventricular ROI definition possible with such collimation.

If regurgitation from the right atrium into the inferior vena cava is suspected it may be quantified by the method proposed by Tumeh and colleagues (1982). This method involves recording an ECG gated study of the liver and examining the count rate in the liver during the cardiac cycle. If there is regurgitation, the liver count rate will rise during atrial contraction, rather than remain steady as in normals.

With a knowledge of the absolute value of the stroke volume it is possible to calculate the volume of blood entering the systemic circulation per unit time, the cardiac output (CO) since:

$$CO = SV.(\text{Heart rate}) \qquad 5.12$$

In order to determine an absolute value of a patient's stroke volume, in the absence of regurgitation, then it is necessary to measure the factor k_{LV} (or k_{RV}) directly for the system using blood samples or to obtain a calibration curve to predict the true stroke volume for a given value of stroke counts. This has been achieved by measuring patients' stroke volumes (by, for example, thermodilution) and performing linear regression between these values and the stroke counts measured from the images (Burow et al, 1982, Melin et al, 1985).

6.0 Left ventricular edge detection

The scintigraphic measurement of left ventricular ejection fraction (LVEF) provides a valuable, non-invasive assessment of cardiac function (Chapter 5). The images derived from multi-gated equilibrium blood pool acquisition (MUGA) studies permit the visualization of the blood in the heart chambers throughout the cardiac cycle. Under the conditions pertaining during MUGA imaging, changes in left ventricular count rate, after appropriate background correction, are caused by changes in left ventricular blood volume. Thus, the computation of LVEF requires the delineation of the left ventricular boundary and the definition of a region representing background activity. This may be achieved by manual tracing of the outlines or by means of an automated edge detection algorithm (Chang et al, 1980a; Goris et al, 1981; Reiber et al, 1983; Todd-Pokropek, 1983). Manual procedures may give rise to large inter- and intra-operator variations (Burow et al, 1977; Okada et al, 1980).

The use of an automated outlining algorithm removes observer dependent variation. There are two areas in which the improved reproducibility of an automated technique for LVEF measurements would be of particular value. The first is in long term follow up of patients after cardiac surgery, and the second is in the short term evaluation of patient response to exercise and/or drug administration.

Edge detection methods based purely on an isocount contour or on gradient or Laplacian operators (Davis, 1975; Chang et al, 1980a) were not considered to be sufficiently reliable to warrant further examination. This is primarily due to the higher count rate at the interventricular septum compared with that at the free wall of the left ventricle (Todd-Pokropek, 1983).

Hence, an original fully automatic edge detection software package was devised. The development of the algorithm for this package, and its validation with clinical data are described below.

Two semi-automatic methods of edge detection were first examined and compared. The first (Method 1) uses the interpolative background subtraction technique described by Goris et al (1976) to produce an image with reduced differences between septal and free wall count densities, by isolation of the left ventricle (Goris and Briandet, 1983). An isocount contour from this new image then defines the left ventricular edge. The second method (Method 2) uses a pseudo-Laplacian convolution operator to define the edges (Goris et al, 1981).

The fully automatic algorithm is a combination of Methods 1 and 2. Values of LVEF derived from MUGA images by the algorithm have been compared with those derived by a manual procedure and with those determined by left ventricular cineangiography.

6.1 Patients

The algorithms were evaluated using data acquired in a total of 89 patients randomly selected from those referred for routine left ventricular function studies. The age range of the patients was 24 to 68 years. The patients were divided into groups A and B of 33 and 56 patients respectively, for evaluation of the semi-automatic algorithms and the fully automatic algorithm.

Each patient in group A was assigned to one of two sub-groups, A1 (13 patients) and A2 (20 patients). The data from the first of these sub-groups were used to derive a value for the isocount contour that was used in semi-automatic Method 1 and subsequently in the fully automatic algorithm. The data from the second sub-group were used to compare the two semi-automatic methods applied by four trained observers and a standard 2-ROI manual method applied by a single observer.

The 56 patients in group B were each assigned to one of three sub-groups, B1, B2 and B3. The image data from group B1 (28 patients) were analysed by the fully automatic algorithm and manually by four

trained observers. Seventeen patients formed group B2; all patients in this group had their ejection fractions ($LVEF_1$) assessed radiographically by single plane left ventricular cineangiography (LVA) within 40 days of MUGA imaging. In all cases therapy remained unchanged between the two studies. Group B3 consisted of 11 patients referred consecutively. Each of these patients was imaged in the LAO and anterior projections, and was then repositioned by a different technician for a second LAO view. This view was recorded within 30 minutes of the first LAO view.

6.2 Acquisition and preprocessing

The patients' red blood cells were labelled in-vivo with 750 MBq technetium-99m (Pavel et al,1977).

MUGA data were acquired in the LAO projection using a 40 cm field of view gamma camera, with low energy general purpose parallel hole collimator, interfaced to a Nodecrest V76 minicomputer. Data were acquired as sixteen frames of matrix size 32 x 32, using a 2x software zoom. Data were accumulated for five minutes, resulting in a total of between 1 and 2 million counts in the images.

Prior to the manual or automatic definition of the left ventricular outline, the following preprocessing was applied to the images. First, a smoothed thresholded view (view A) was formed. The smoothing was by a filter of weights {1 2 1} applied in two-dimensions, once to each of the sixteen frames. Thresholding was achieved by an interpolative background subtraction algorithm (program CARDB, Nodecrest Ltd, Byfleet) based on the method described by Goris et al (1976), but using only the counts in the right hand column (column 32) and bottom row (row 1) of each frame. For each pixel P(x,y) the required threshold was computed as the mean of the counts in the pixels P(1,y) and P(x,32).

Secondly, parametric images were formed, including Fourier

amplitude and phase images and a residual volume image (view B) (programs FOU and PIMS, Nodecrest Ltd, Byfleet). Residual volume is here defined for each pixel, i, as

$$RV_i = ED_i - SV_i \qquad 6.1$$

where ED_i = end diastolic count rate in pixel i

SV_i = stroke volume of pixel i

$= ED_i - ES_i$, when $ED_i > ES_i$

$= 0$, when $ED_i < ES_i$

ES_i = end systolic count rate in pixel i.

Finally, a sixteen frame view (C) was formed by "back projection" of the Fourier amplitude and phase images.

6.3 Manual region of interest selection

A region of interest was defined encompassing the left ventricle on the first frame of view A, using the Fourier phase and amplitude images as a guide. A time-activity curve, C_{ed}, using this end-diastolic ROI, was generated from the raw data. The nadir of this curve defined the end-systolic frame. This frame of view A was displayed and an end-systolic ROI outlining the ventricle was defined. In addition, a background ROI below and to the right of the end-diastolic ROI was selected (figure P6.1).

Time-activity curves for the end-systolic and background ROIs were formed from the raw data (C_{es} and C_{bg} respectively), and curves C_{ed} and C_{es} were corrected for background using curve C_{bg}.

Left ventricular ejection fraction was then calculated as

$$LVEF_m = (C_{ed,max} - C_{es,min})/C_{ed,max} \qquad 6.2$$

where $C_{ed,max}$ = maximum count in corrected curve C_{ed}

and $C_{es,min}$ = minimum count in corrected curve C_{es}.

6.4 Semi-automatic edge detection

6.4.1 Method 1

Interpolative background subtraction (Goris et al, 1976) was used to isolate the left ventricle from surrounding structures. On the first frame of the Fourier "back projected" image, view C, a rectangular box was positioned by the operator such that the upper border of the box defined approximately the plane of the mitral and aortic valves and the left hand border defined the septum. The lower and right hand borders were positioned so that the left ventricle was completely enclosed by the box (figure P6.2a).

This box defined the area in which the interpolative background subtraction technique operated. The operation was as follows. First, all pixels outside the area defined by the box were set to a value of zero. Secondly, all pixels within the box had a background value subtracted from them. This value was calculated as the average of two linearly-interpolated values. The first interpolation was between the two pixels on the borders of the rectangle with the same horizontal coordinate as the pixel in question but with vertical coordinates corresponding to the upper and lower borders of the rectangular box. The second interpolation was between the two points with the same vertical coordinate as the pixel considered but with horizontal coordinates corresponding to the right and left hand borders of the box. Finally all pixels on the border of the box were given a value of zero. This results in an image like that shown in figure P6.2b.

The interpolative background subtraction was performed for each frame in the view, using the same box, and the left ventricular region of interest (LVROI) was defined as the isocount contour corresponding to ten per cent of the maximum count per pixel in the view (figure P6.2c,d). The corresponding LVROI, which is stored in the same 32*32 matrix format as the images, is shown in figure P6.3. Also shown is the

single blood background ROI which was automatically defined, 2 cells wide, 2 cells from the LVROI on the first frame, as an arc in the lower right quadrant of the image.

Total counts from the raw data for each of the 16 LVROIs were corrected for background counts and a time-activity curve formed. From this curve, left ventricular ejection fraction for Method 1 was directly calculated (figure 6.4) as:

$$LVEF_{M1} = (C_{max} - C_{min})/C_{max} \qquad 6.3$$

where C_{max}, C_{min} are the maximum and minimum count rate values. Figure P6.5 shows the LVROIs obtained in typical studies.

6.4.2 Method 2

Following the method described by Goris et al (1981), a convolution operator ('O') was applied to each frame of the image sequentially in the horizontal, vertical and two diagonal directions. The kernel of 'O' was {2,2,-2,-4,-2,2,2}. In order to speed computation, this process was only applied in the area of an operator specified box. This box was defined to completely enclose the left ventricle, and its centre approximately coincided with the centre of the left ventricle.

Following each convolution operator pass, negative values were set to zero, and a search was performed for local maxima, in the direction of the operator pass. If a pixel contained a local maximum in any pass, then the corresponding pixel of a binary image, originally set to zero, was reset to 1. On the completion of the fourth pass, the left ventricle was surrounded by a closed border of non-zero values. Non-zero values outside this border (surrounding other vascular structures) were eliminated by the following method. For each non-zero pixel, a profile of the binary image was constructed, the start point of which was the position of that pixel and the end point of which was the centre of the operator defined box. Moving along this profile, if any element

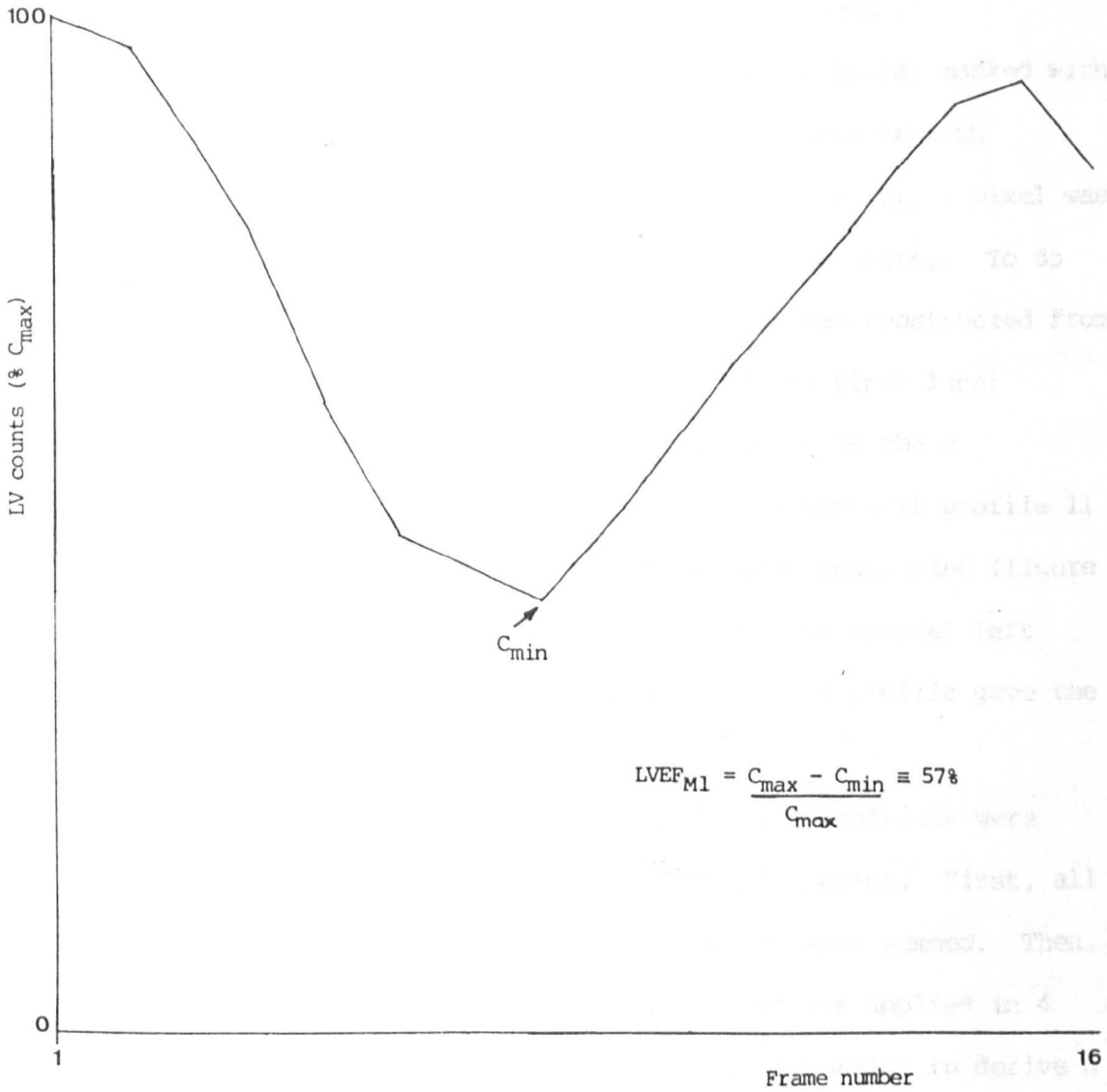

Figure 6.4 Background corrected left ventricular counts versus frame number.

encountered was non-zero, then the initial pixel was not a left ventricular edge, and its value was reset to 0. The remaining elements then defined the LVROI (figure P6.6).

A background ROI was defined and a left ventricular volume curve formed from the raw image data as in Method 1. Ejection fractions ($LVEF_{M2}$) were then calculated from equation 6.3.

6.5 Fully automatic edge detection

The edge detection algorithm operated in five stages.

(i) Using the residual volume image (view B, figure P6.7a) masked with the Fourier phase image (figure P6.7b) so that pixels with non-ventricular phase were set to zero (figure P6.7c), a pixel was identified approximately at the left ventricular centre. To do this, a horizontal profile through all pixels was constructed from this image (figure P6.7d). The position of the first local maximum, from the right of the image, was taken as the x coordinate of the left ventricular centre. A vertical profile 11 pixels wide, centred on the x coordinate, was constructed (figure P6.7e). (This width was chosen to encompass the typical left ventricle). The position of the maximum of this profile gave the y coordinate of the left ventricular centre.

(ii) The edges of a rectangular box around the left ventricle were identified, for interpolative background subtraction. First, all frames of the Fourier back projected view (C) were summed. Then, the pseudo-Laplacian convolution operator 'O' was applied in 4 directions (horizontal, vertical and the 2 diagonals) to derive a left ventricular edge from the summed view, using the ventricular centre determined in step (i).

(iii) An isolated left ventricle image of sixteen frames (view D) was then formed. The minimum and maximum x and y coordinates of the

edge determined in step (ii) defined the box limits for interpolative background subtraction which was applied as in semi-automatic Method 1.

(iv) A region of interest was generated from each frame of view D, from the isocount contour corresponding to 10% of the maximum count in view D. A background ROI was formed as in Method 1.

(v) A background corrected left ventricular time-activity curve was generated from the original unprocessed image data using the ROIs created in step (iv). From this curve the left ventricular ejection fraction $LVEF_a$ was computed from equation 6.3.

If the algorithm failed to produce an acceptable contour, as determined by inspection of the derived edges generated without operator intervention, a predetermined operator intervention took place. This consisted of the operator setting the left ventricular centre (step (i)) to be the left ventricular pixel with maximum counts in the first frame of the view. This pixel was selected by the operator using a TV display. If the contour produced after this intervention appeared unacceptable the automatic method was considered to have failed.

6.6 Results

6.6.1 Patient group A1

In order to derive an appropriate value for the isocount contours required by semi-automatic Method 1 and by the fully automatic algorithm, ejection fractions for the 13 patients of this group were measured by the manual method and compared with the results obtained using Method 1 with isocount contours of 10 and 20 per cent (table 6.1). All analyses were performed by the same observer, O1.

Using Wilcoxon's signed rank test (for paired samples) at the 5% level of significance, no significant differences were detected between the manual method and the 10 per cent contour method, while there were

Table 6.1 Patient group A1

Left ventricular ejection fraction (%) derived by observer O1

Patient	Manual method	Semi-automatic method 1	
		10% contour	20% contour
1	43	39	40
2	46	43	50
3	51	50	64
4	70	72	79
5	25	24	26
6	7	10	6
7	42	44	49
8	48	46	48
9	71	62	72
10	56	53	58
11	45	52	53
12	80	95	99
13	45	41	43

significant differences between the manual method and the 20 percent contour method.

Therefore, the 10% isocount contour was selected.

6.6.2 Patient group A2

The 20 patients of group A2 provided the source of data for the comparison of the two semi-automatic methods. Both methods failed to generate an outline in 4 cases. This was due to poor positioning of the patient, so that the interventricular septum was not visible.

The four observers (O1,O2,O3,O4) independently measured the LVEF using both methods for each of the 16 remaining patients. The results are presented in table 6.2, together with the ejection fraction value for each patient derived by the manual method by observer O1. Also shown are the means and standard deviations of the ejection fraction values obtained by the 4 observers for each patient and method.

In order to test the homoscedasticity of the data to allow parametric analysis of variance to be used to compare the methods, linear regression was performed between the mean and standard deviation of ejection fraction for each patient over the four observers for each method (figure 6.8). From figure 6.8 it is apparent that the standard deviation increases with increasing mean ejection fraction for Method 1, but that this is not the case for Method 2. Therefore, two two-way analyses were performed; the first on the data from the 4 observers using Method 1 and the manual ROI data, after a logarithmic transformation to produce homoscedasticity in the data; and the second on the Method 2 data and the manual ROI data, without transformation. The transformation used for Method 1 data was:

$$\text{transformed LVEF}_{M1} = \log_{10} (\text{LVEF}_{M1}).$$

The results of these analyses are summarised in figure 6.9 in the form of 95% confidence intervals between the 4 observers and the 2 ROI

Table 6.2 Patient group A2

Left ventricular ejection fraction (%)

	Observer	O1	O2	O3	O4		
Method	Patient	Manual (O1)				Mean	s.d.
1	1	16	10	10	11	11	10.50	0.577
	2	22	32	28	32	28	30.00	2.309
	3	69	82	81	66	81	77.50	7.681
	4	31	32	29	27	33	30.25	2.754
	5	25	29	21	22	21	23.25	3.862
	6	29	29	28	26	28	28.00	0.816
	7	6	9	9	7	8	8.25	0.957
	8	24	23	19	17	19	19.75	2.986
	9	58	60	52	42	47	50.25	7.676
	10	17	19	12	10	15	14.00	3.916
	11	52	75	66	52	64	64.25	9.465
	12	55	71	54	39	44	52.00	14.12
	13	37	30	32	25	22	27.25	4.573
	14	40	42	32	37	36	36.75	4.113
	15	15	12	5	8	10	8.75	2.986
	16	52	49	37	42	38	41.50	5.447
2	1	16	10	10	11	11	10.50	0.577
	2	22	35	34	34	34	34.25	0.500
	3	69	69	69	66	69	68.25	1.500
	4	31	32	32	28	33	31.25	2.217
	5	25	28	20	17	22	21.75	4.646
	6	29	26	27	26	26	26.25	0.500
	7	6	7	7	9	7	7.50	1.000
	8	24	21	23	25	21	22.50	1.915
	9	58	53	55	51	52	52.75	1.708
	10	17	15	14	13	12	13.50	1.291
	11	52	55	55	54	52	54.00	1.414
	12	55	47	45	47	45	46.00	1.155
	13	37	33	34	30	33	32.50	1.732
	14	40	39	35	35	35	36.00	2.000
	15	15	8	11	9	8	9.00	1.414
	16	52	40	41	43	37	40.25	2.500

manual method for each of the two semi-automatic methods, after extraction of patient variability. In figure 6.9, an observer's mean LVEF lies within the confidence interval of another observer when there is no significant difference between the two means ($p=0.05$).

It can be seen that there were no significant differences between the manual method (Man) and observer O1 or between the three observers O2,O3,O4 using Method 1, but that the ejection fractions measured by the observer set {Man,O1} were significantly greater than those measured by the set {O2,O3,O4}. For Method 2 there are no differences between the four observers {O1,O2,O3,O4} but the ejection fractions were significantly less than those measured by the manual method.

6.6.3 Patient group B1

The results of the analyses of this group of 28 patient studies by the four observers O1,O2,O3 and O5 are given in table 6.3. The mean and standard deviation of the four $LVEF_m$ values for each patient were computed (figure 6.10); the standard deviation of $LVEF_m$ was positively correlated with mean $LVEF_m$ (correlation coefficient = 0.59) and significantly greater than 0 ($p<0.01$). The $LVEF_m$ values derived by the four observers were assessed after logarithmic transformation by two-way analysis of variance; there were no significant differences between observers ($p>0.5$).

In order to compare the manual method with the fully automatic method, mean $LVEF_m$ was plotted against $LVEF_a$ (figure 6.11); the relationship was non-linear and indicated that the two methods correlated poorly when ejection fractions below 20% were considered.

In three cases no contour could be derived by the automatic method, and in a further five cases operator intervention was necessary.

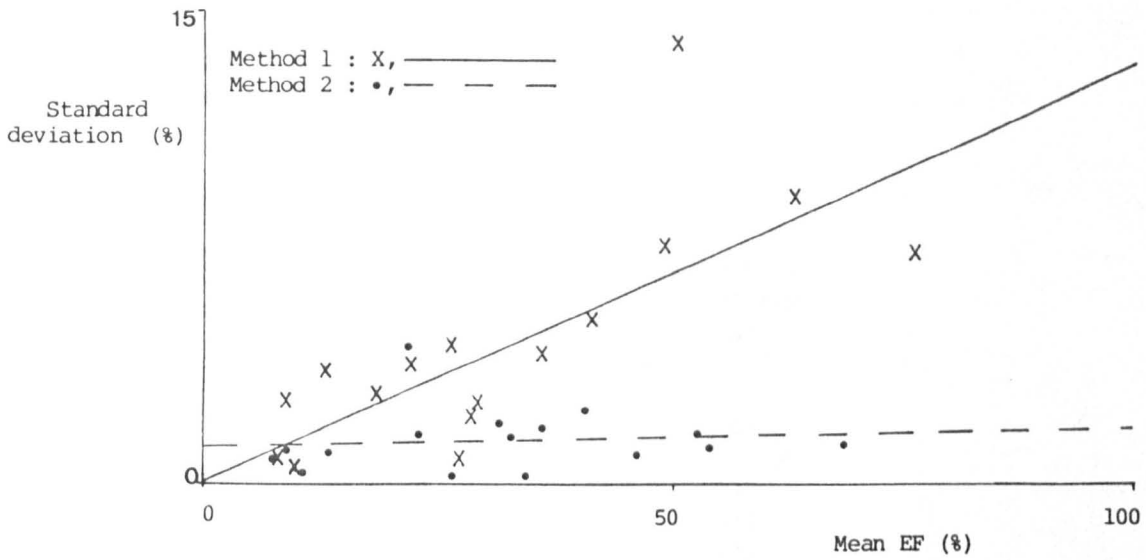

Figure 6.8 Mean LVEF versus standard deviation of LVEF (Semi-automatic methods, 4 observers, patient group A2).

Method 1 : slope of fitted line = 0.134, SE = 0.031.

Method 2 : slope of fitted line = 0.003, SE = 0.015.

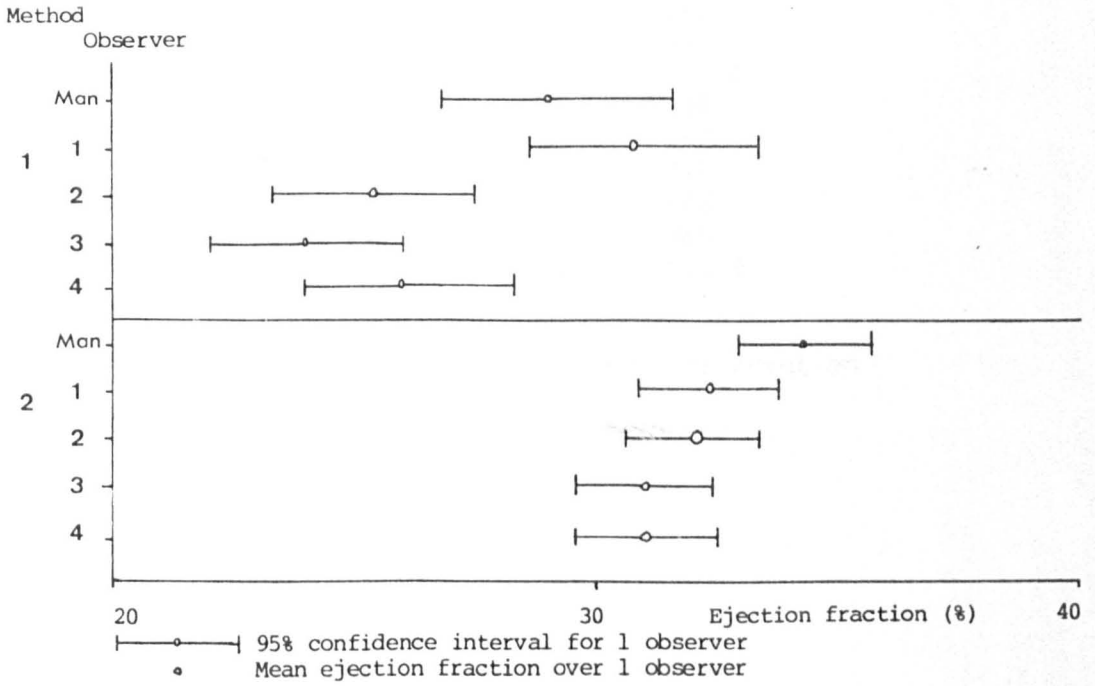

Figure 6.9 95% confidence intervals for LVEF. Derived from analysis of variance of LVEF data from patient group A2.

Table 6.3 Patient group B1

Left ventricular ejection fraction ($x10^3$)

Patient	Manual method: $LVEF_m$ Observer: O1	O2	O3	O5	s.d.	Mean	Automatic algorithm $LVEF_a$	
1	338	169	339	200	90	262	89	
2	154	215	121	165	39	164		F
3	659	539	712	571	79	620	697	
4	565	469	588	369	100	498	537	
5	351	387	390	332	28	365	376	
6	222	227	193	203	16	211	208	
7	204	300	232	210	44	237	130	+
8	241	313	208	264	44	257	203	
9	541	450	342	444	81	444	513	
10	378	339	347	432	42	374	352	
11	110	192	170	145	35	154	72	
12	371	406	382	369	17	382	425	+
13	249	269	271	245	13	259	124	+
14	630	424	417	352	122	456	515	+
15	233	242	285	211	31	243		F
16	234	154	223	273	50	221	197	
17	248	257	219	269	21	248	214	
18	276	290	283	271	8	280	237	
19	419	487	481	431	35	455	484	
20	245	261	256	254	7	254	219	
21	335	339	325	315	11	329	341	
22	129	181	142	165	23	154		F
23	319	338	346	354	15	339	258	
24	170	127	302	249	78	212	242	
25	258	200	236	189	32	221	211	
26	511	477	396	456	48	460	548	
27	161	221	309	234	61	231	265	
28	555	527	627	865	154	644	522	+

+ = $LVEF_a$ value obtained only after operator intervention

F = Automatic method failed even after intervention.

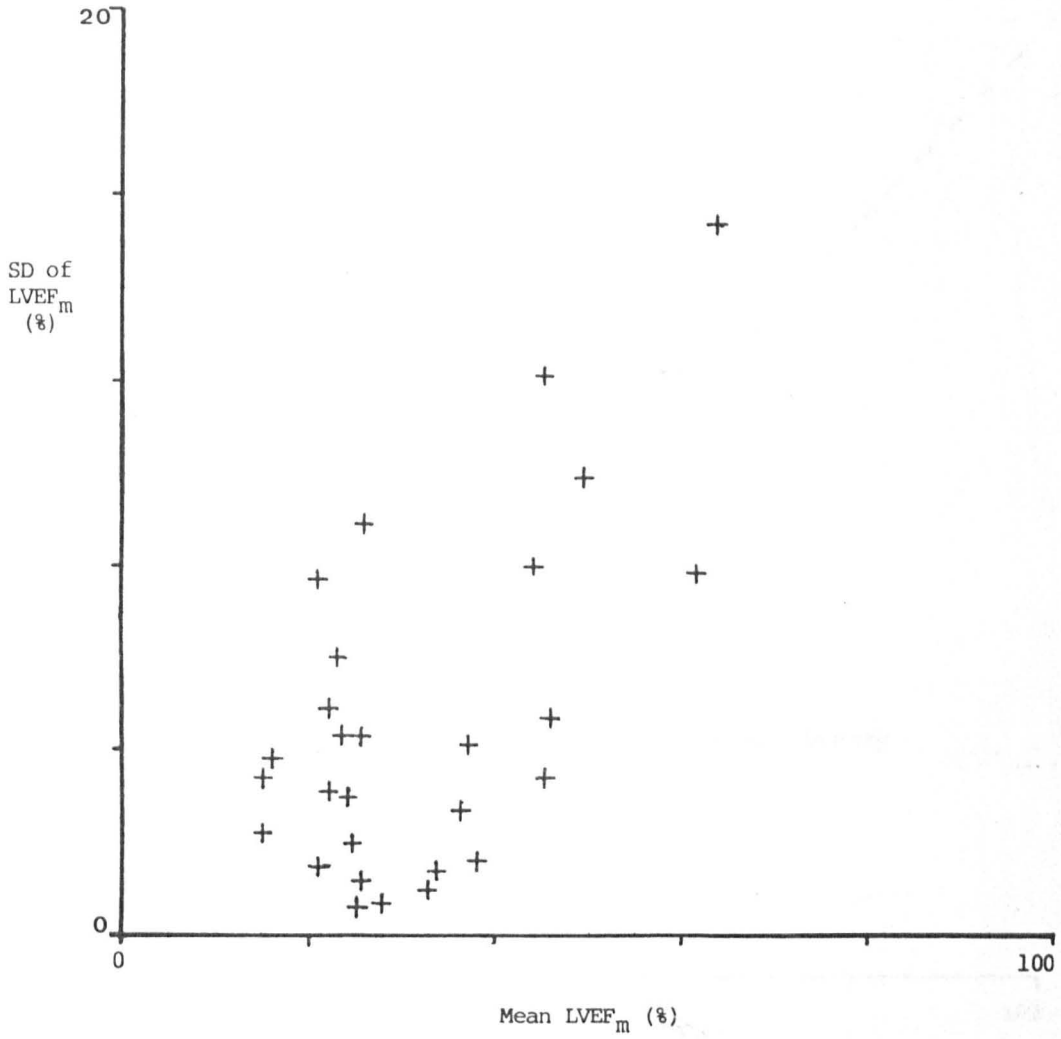

Figure 6.10 Comparison of standard deviation of $LVEF_m$ with mean $LVEF_m$ (manual method, 4 observers, patient group B1).

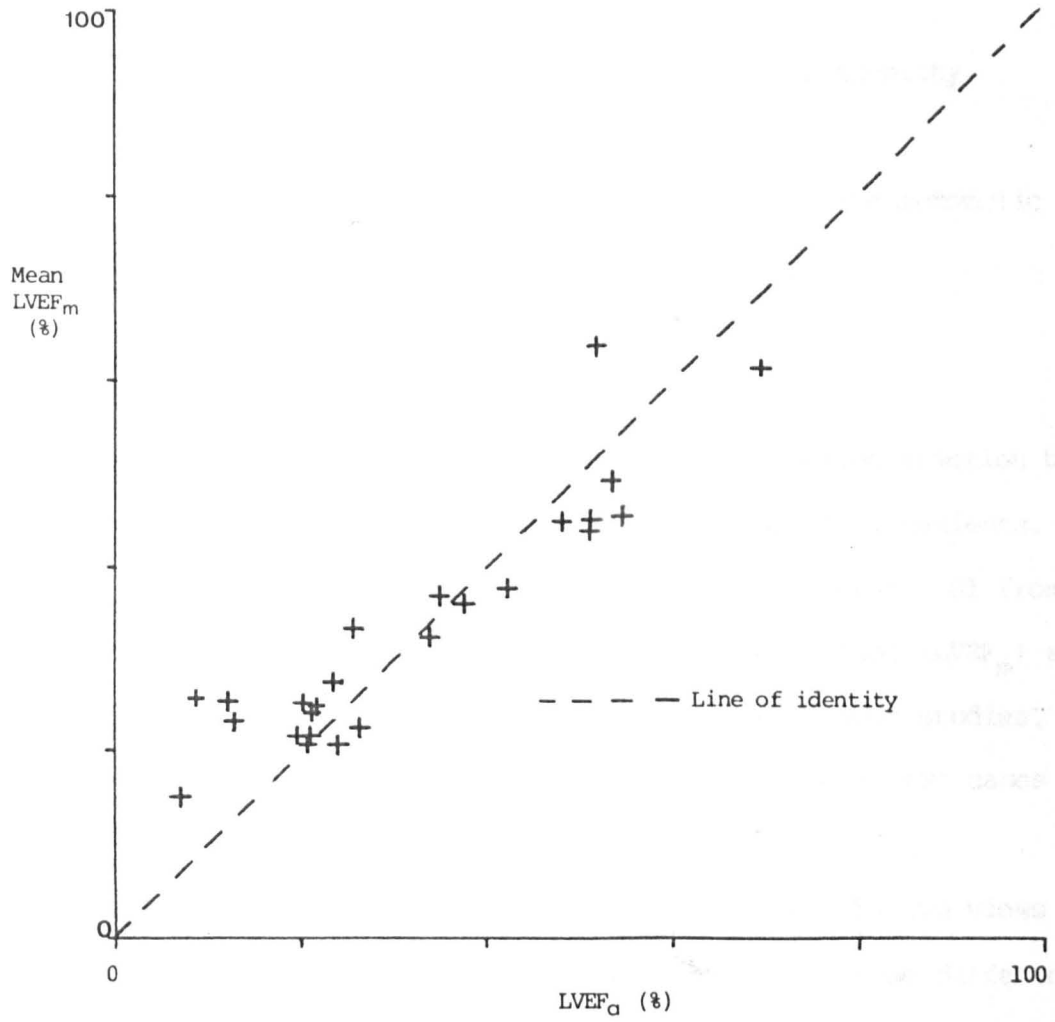

Figure 6.11 Comparison of ejection fractions derived by the automatic method ($LVEF_a$) with the mean of the four observers manual ejection fractions (mean $LVEF_m$), patient group B1.

6.6.4 Patient group B2

In order to compare the automatic method with an independent estimator of left ventricular ejection fraction, the automatic method was applied to a group of 17 patients whose ejection fraction ($LVEF_l$) was measured by single plane cineventriculography within 40 days of MUGA imaging (table 6.4). $LVEF_l$ was plotted against $LVEF_a$ (figure 6.12) and linear regression gave

$$LVEF_l = 0.95\ LVEF_a + 6.90\%$$

a line not significantly different from the line of identity (intercept; $p = 0.13$: slope; $p = 0.69$).

In one case a contour could not be produced by the automatic method, while in six cases intervention was necessary.

6.6.5 Patient group B3

The reproducibility of the measurement of ejection fraction by the fully automatic method was assessed in this group of 11 patients. Table 6.5 gives the ejection fractions derived by operator O1 from the two different LAO views (V1 and V2) by the manual method ($LVEF_m$) and the automatic method ($LVEF_a$) for each of 11 consecutive MUGA studies.

The automatic method failed on one occasion and in two cases intervention was necessary.

Differences between the ejection fractions for the two views were computed for each method (D_m and D_a). The means of these differences were not significantly different from zero (t-test) for either the manual method ($p>0.9$) or the automatic method ($p>0.6$). However, the standard deviation of D_a was significantly less than the standard deviation of D_m ($p<0.05$, F-test).

6.6.6 Failure rate

The failure rate of the fully automatic algorithm was assessed

Table 6.4 Patient group B2

Left ventricular ejection fraction (%) derived from the fully automatic algorithm ($LVEF_a$) and by single plane cineventriculography ($LVEF_l$).

Patient	$LVEF_a$	$LVEF_l$
1	21	29
2	24	20
3	17	14
4	67	77
5	22	34
6	59	76
7	56+	64
8	7	21
9	25+	40
10	58+	48
11	17	18
12	28	31
13	40	35
14	46+	42
15	90+	50
16	43+	65

+ = $LVEF_a$ value obtained only after operator intervention, in addition there was 1 study in which the algorithm failed after intervention.

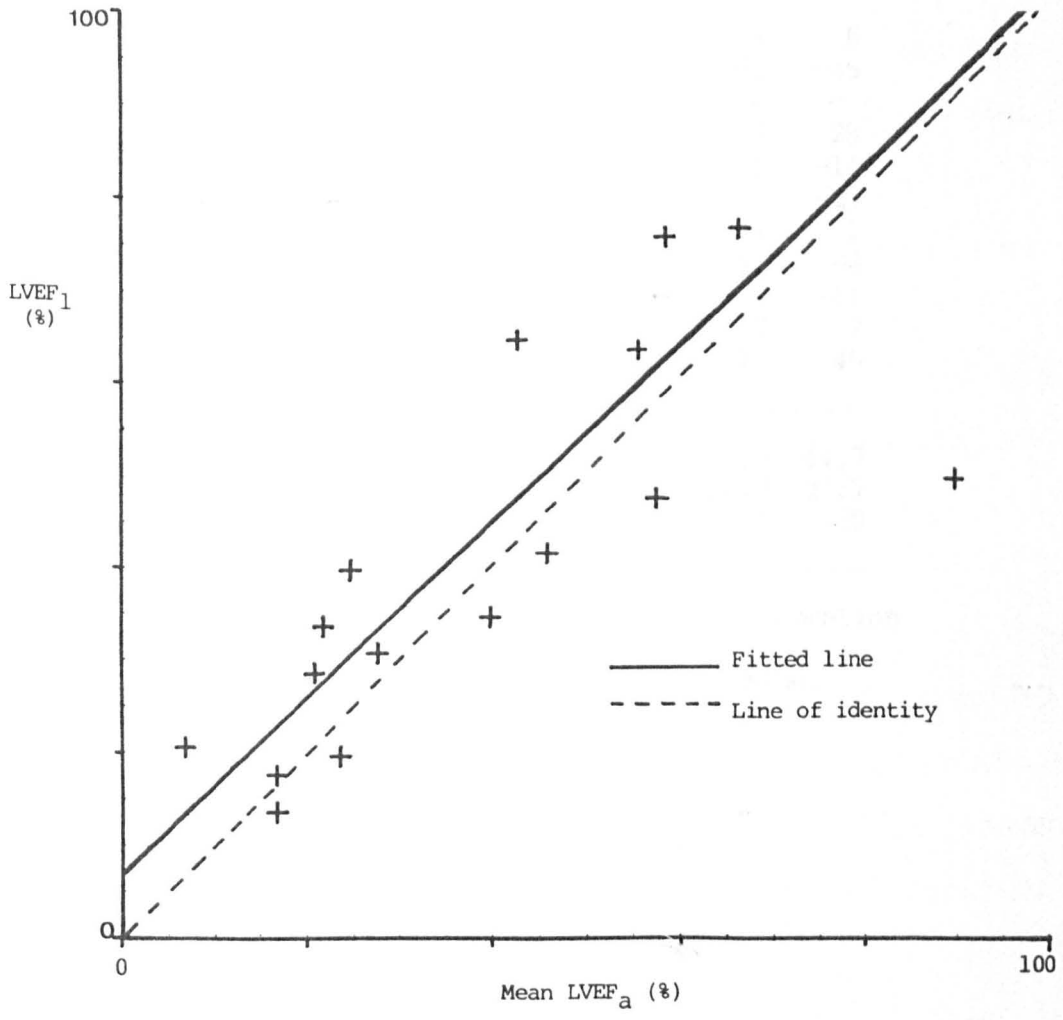

Figure 6.12 Comparison of ejection fractions derived by the automatic method ($LVEF_a$) and left ventricular contrast angiography ($LVEF_1$), patient group B2.

Table 6.5 Patient group B3

Left ventricular ejection fraction ($x10^3$) derived from two consecutive acquisitions (V1 and V2) using the manual method ($LVEF_m$) and the automatic algorithm ($LVEF_a$).

	$LVEF_m$		$LVEF_a$		Difference	
Patient	V1	V2	V1	V2	D_m	D_a
1	217	222	174	168	-5	6
2	204	285	141	186	-81	-45
3	249	197	156	F	54	-
4	353	247	240	212	106	28
5	286	305	251	265	-19	-14
6	269	228	216	241	41	-25
7	383	330	311	310	53	1
8	434	456	409	413	-22	-4
9	686	678	702+	763+	8	-61
10	207	214	184	177	-7	7
11	403	480	345	385	-77	-40
	mean of differences				4.6	-14.7
	s.d. of differences				56.5	27.7
				n	11	10

+ = $LVEF_a$ value obtained only after operator intervention

F = Automatic method failed even after intervention.

using the 56 patients of group B. A total of 67 LAO images were obtained from this group, since there were 11 repeated views (sub-group B3). There were only five failures after intervention (7.5%) and 13 successful interventions (19.4%).

6.7 Discussion

The position chosen for the background ROI relative to the ventricle for both the manual and automatic methods was that recommended by Taylor and colleagues (1980). This positioning was also similar to that automatically selected by the programs of Reiber et al (1983). In none of the patient studies was it necessary to reposition the background ROI to avoid prominent blood pool activity, such as the spleen.

In the present study the mean standard deviation of LVEF, when using the manual 2 ROI method, was 4.7% (ejection fraction units). This value was comparable with the results of other workers (Burow et al, 1977; Okada et al, 1980; Taylor et al, 1980; Hains et al, 1986).

Both the manual 2 ROI method and semi-automatic Method 1 showed a significant increase in standard deviation of LVEF with increasing LVEF. A correlation between ejection fraction and its variability has been previously reported for single and two ROI manual methods (Hawkins and Keavey, 1984) and for a semi automatic 'frame by frame' algorithm (Wackers et al, 1979).

Ejection fractions derived from Method 2 were not observer dependent, but were significantly smaller than the results obtained from the standard 2 ROI manual method. Since the primary aim of the algorithm was to produce reproducible estimates of LVEF, this reduction in LVEF value was not considered important.

Compared with LVEF derived from manually defined ROIs there was a reduction in LVEF when observers {02,03,04} applied Method 1 and for all

four observers using Method 2. In the case of Method 1, the ROIs defined by these observers were smaller at the free wall at end diastole than the manually drawn ROIs (figure 6.13), due to operator selection of smaller boxes for interpolative background subtraction. This gave rise to underestimation of the end diastolic count rate compared to the end systolic count rate. However, choice of a 20% isocount contour using the interpolative background subtraction resulted in a ROI which was smaller at both end diastole and end systole (figure 6.13e). This result was caused by the dependance of background ROI position on LVROI size, since the background ROI was placed a fixed distance from the ventricular free wall edge. That is, the background ROI was located further from the heart for a 10% isocount contour than for a 20% contour, with fewer counts per pixel, giving a larger LVEF (table 6.1). For Method 2, larger ROIs were produced (figure 6.13d) resulting in underestimation of background count rates and therefore a low LVEF. Furthermore, the binary edges produced by Method 2 gave very poor tracking of the left ventricular free wall boundary and could essentially be considered a single ROI (figure 6.14). Single left ventricular ROI methods for the computation of the ejection fraction, whether manual or automated, have been shown to give rise to consistent underestimation of LVEF (Taylor et al, 1980; Reiber et al, 1983; Hains et al, 1986).

A secondary purpose of the detection of the left ventricular edge was to examine regional left ventricular wall motion during the cardiac cycle. The contours derived from Method 1 by observer O1 were acceptable for this purpose, while those derived by observers {O2,O3,O4} were too large in the free wall area. The binary edges produced by Method 2 were of little value in the evaluation of wall motion.

Method 2 would be well suited to full automation since the only information required to start the edge detection process was an

approximate position for the centre of the left ventricle; the box described above was defined merely to speed computation. An approximate left ventricular centre may be derived automatically from functional criteria, such as the centre of gravity of counts in an amplitude image (Goris et al, 1981), or, as above, from the residual volume image. The results obtained from full automation of Method 2 should bear close resemblance to those from the methods described by Reiber and colleagues (1983) and by Todd-Pokropek (1983), as the second derivative operator used in these two methods has a similar effect to Goris's pseudo-Laplacian operator. However, the poor performance of Method 2 for regional wall motion evaluation and the underestimation of LVEF are significant drawbacks. Therefore, the pseudo-Laplacian edge detection operator was not tested in a fully automatic implementation, such as using the left ventricular edge found at step (ii) of the fully automatic algorithm, to form a single ROI for LVEF determination.

In order to fully automate Method 1, it was necessary to define the interventricular septum and valve plane accurately, and to approximate the free wall position. This has been achieved by using the pseudo-Laplacian operator of Method 2. The upper and lower limits, in the x and y directions, of the left ventricular edge thus found were then used as the limits of the rectangular box required for the interpolated background subtraction.

The algorithm implemented thus produced a left ventricular edge for each frame of the image data. Other 'frame by frame' algorithms have been described by Reiber et al (1983) and Todd-Pokropek (1983). Reiber and coworkers compared their algorithm with an automated two ROI method producing end diastolic and end systolic contours and found no statistically significant differences between the two measurements of LVEF. The two ROI method was recommended because of its speed of operation. However, Todd-Pokropek (1983) suggested that contours

determined on a frame by frame basis could be used to study regional wall motion. The contours derived by the present algorithm have been used for clinical evaluation of regional wall motion, in addition to their use in computation of LVEF.

The reproducibility of the analysis of two independent views in patient group B3 (table 6.5) was excellent, with standard deviation of differences of less than 3% (ejection fraction units), and mean difference of 1.5% (ejection fraction units) for the fully automated method. These values compare well with the results of similar studies (Pfisterer et al, 1979; Wackers et al, 1979; Reiber et al, 1983).

The algorithm produced ejection fraction values similar to those derived from the "gold standard" for LVEF measurement: left ventricular cineangiography. The scatter in the data seen in Figure 6.12 ($LVEF_l$ versus $LVEF_a$) may be attributed, at least in part, to the substantial variability in measurements by the radiographic technique (Chaitman et al, 1975; Rogers et al, 1979).

The failure rate of the algorithm of 7.5% was similar to the 8% failure rate achieved by the algorithm described by Goris et al (1981) under similar imaging conditions and without operator intervention. Failure of the algorithm appeared to be unrelated to either LVEF value or regional wall motion abnormalities.

The algorithm was implemented in FORTRAN IV and is therefore easily transportable. Approximately thirty minutes were required to produce a left ventricular volume curve, including the preprocessing time of 10 minutes. This could be considerably reduced on more modern computer systems, and by reducing the number of unnecessary disk operations required. For instance, the ROIs in step (iv) need not be stored as they were in the implementation described.

In conclusion, it has been shown that left ventricular ejection

fraction can be reliably determined from MUGA images by an automatic edge detection algorithm, overcoming the variability inherent in manual ROI definition. The fully automatic algorithm described produces highly reproducible LVEF values, it provides useful information relating to regional wall motion, and it may be implemented readily on most nuclear medicine computer systems.

7. Myocardial perfusion imaging with $^{99}Tc^{m}$-tBIN

Myocardial perfusion scintigraphy has become a widely accepted aspect of the clinical evaluation of patients with ischaemic heart disease. The agent of choice for such studies is currently ^{201}Tl-thallous chloride, for which the initial distribution reflects myocardial blood flow. There has, however, been interest in the development of technetium-99m labelled myocardial perfusion agents since technetium-99m offers significant advantages as a radiotracer compared with thallium-201. It is produced in commercially available generators, and is therefore cheaper and more readily available than thallium-201. It has a short half-life of 6 hours with a monoenergetic 140 keV photopeak, ideally matched to the characteristics of modern imaging devices, whereas thallium-201 has a half-life of 73.5 hours and its principal energies of emission are 69 and 83 keV. Such low photon energies are not optimal for imaging since attenuation and scatter within the patient result in significant image degradation.

For these reasons, various $^{99}Tc^{m}$-labelled myocardial perfusion agents have been developed (Holman et al, 1984; Khalil et al, 1985b; Gerundini et al, 1986; Holman et al, 1987). These agents were designed to be monovalent cationic complexes in order to mimic the in-vivo distribution of potassium and thallium ions. However, the low charge density within the large complex and the lipophilicity of the outer groups (figure 7.1) causes the distributions of these agents to differ from those of potassium and thallium ions. The exact mechanism of uptake of these agents has yet to be fully described. Since the outer groups are lipophilic the complexes are able to pass through the cell wall but there does not appear to be any intracellular binding mechanism. Significant interfering uptake occurs into the liver, spleen and lungs, partly due to accumulation in the cell walls, but also in the liver by active trapping followed by excretion. Relative uptakes in

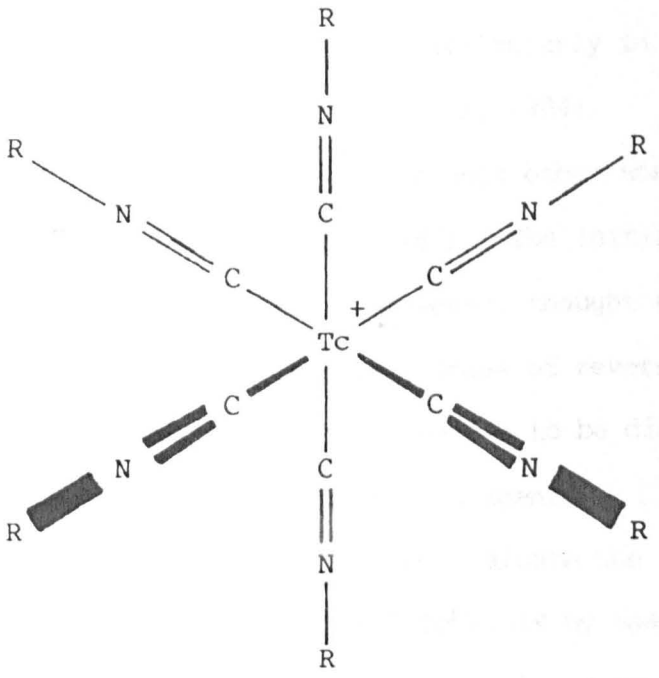

tBIN : R = t-butyl = 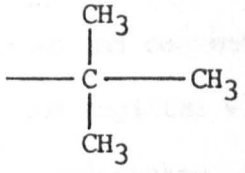

Figure 7.1 Structure of $^{99}Tc^{m}$-tBIN

these organs and the myocardium differs between compounds and is species dependant, reducing the value of animal models (Dudczak et al, 1983).

The distribution of the cationic technetium-99m complex hexakis (tertiary butyl isonitrile) technetium (I) ($^{99}Tc^{m}$-tBIN) reflects myocardial blood flow, and the myocardial uptake is sufficient to allow diagnostic imaging (Khalil et al, 1985a; Gerundini et al, 1986). Some workers have suggested that rapid redistribution of the initial lung uptake into the myocardium, combined with high liver uptake, may reduce the value of $^{99}Tc^{m}$-tBIN for stress studies, particularly in the diagnosis of inferior wall defects (Holman et al, 1984; Campbell et al,1986; Holman et al, 1987), although other workers disagree (Khalil et al, 1985a; Liu et al, 1987). The initial distribution of activity to the lungs is, however, thought to be a source of $^{99}Tc^{m}$-tBIN for redistribution into areas of reversible ischaemia (Holman et al, 1986), allowing ischaemia to be distinguished from infarction after a single injection of the agent.

The present study has been undertaken to evaluate the image quality obtainable in the clinical situation with $^{99}Tc^{m}$-tBIN by tomographic imaging with a rotating gamma camera. Experiment 1 was to examine whether the use of oblique angle tomographic reconstruction (Maublant et al, 1982; O'Brien and Gemmell, 1986; Ziada et al, 1986) would give improved diagnostic accuracy compared with planar and conventional tomographic imaging, i.e. transaxial, coronal and sagittal views. Experiment 2, using a larger patient group, was undertaken, in conjunction with phantom experiments (Chapter 8), to determine the optimum back projection filter for reconstruction of the tomographic data.

7.1 Patients

Twenty patients (18 male, 2 female), aged 35-66 years, formed the

study group, C. Fifteen patients, when admitted to the study, were suspected of having either myocardial infarction or angina. Two patients with old infarction were admitted to the study for investigation of angina pectoris. The remaining three patients had previously had coronary artery bypass graft surgery (CABG) and were experiencing recurrent anginal pain. The first twelve male patients without prior surgery formed sub-group C1, the group for which the comparison of imaging techniques was performed (Experiment 1). Data from all patients were used in the comparison of the back projection filters (Experiment 2).

The diagnosis for each patient was established independently of the radionuclide study by means of serial and exercise ECG (Bruce protocol), serum levels of cardiac enzymes and X-ray coronary angiography, as appropriate (table 7.1). Table 7.2 gives the clinical diagnosis of each patient. In total there were 9 patients with myocardial infarction, 2 with coronary artery stenosis and no infarct, and 9 patients with no infarct or coronary disease. The corresponding figures for patient sub-group C1 were 6, 2 and 4 respectively.

7.2 Imaging procedure

The $^{99}Tc^{m}$-tBIN complex was prepared by adding between 0.5 and 1.0 ml of technetium generator eluate to a vial containing: 0.1ml tBIN/ethanol solution, 6% w/v; 15mg sodium dithionate in 0.5ml 0.04M sodium hydroxide; 1.5ml Analar water; 0.4ml ethanol. After heating the vial to 100°C for 15 minutes the contents were cooled and then neutralized to pH7 with 0.02M aqueous hydrochloric acid (Khalil et al, 1985b). Radiochemical purity, assessed by silica gel chromatography, was greater than 95%.

At peak symptom limited bicycle exercise a bolus of 400MBq $^{99}Tc^{m}$-tBIN was administered intravenously. Exercise, at reduced load if

Table 7.1 Patient group C : diagnostic procedure

Clinical diagnosis of patients included in the evaluation of myocardial imaging with $^{99}Tc^{m}$-tBIN

Admission criterion	Tests used
Suspected myocardial infarction	serial ECG cardiac enzymes exercise ECG
Angina	exercise ECG cardiac catheter
Recurrent angina post CABG	cardiac catheter

Table 7.2 Patient group C : diagnoses

Clinical diagnoses of patients included in the evaluation of myocardial imaging with $^{99}Tc^{m}$-tBIN

Patient	Subgroup	Admission Criterion	Final Clinical Diagnosis
1	—	infarct	no heart disease
2	Cl	angina[1]	antero-apical infarct
3	Cl	angina	double vessel disease
4	Cl	angina	triple vessel disease
5	Cl	infarct	no heart disease
6	Cl	infarct	apical infarct
7	Cl	infarct	antero-apical infarct
8	—	infarct	no heart disease
9	Cl	angina	normal coronary arteries
10	Cl	infarct	no heart disease
11	Cl	infarct	inferior infarct
12	Cl	infarct	inferior infarct
13	Cl	infarct	no heart disease
14	—	CABG	inferior infarct
15	Cl	angina[2]	inferior infarct
16	—	infarct	no heart disease
17	—	CABG	inferior infarct
18	—	CABG	anterior infarct
19	—	angina	normal coronary arteries
20	—	infarct	no heart disease

infarct = suspected myocardial infarction
CABG = recurrent angina after CABG
1 = old infarct: normal coronary arteries
2 = old infarct: double vessel disease

necessary, continued for a further two minutes. Pulse, blood pressure and ECG were recorded during exercise and for 15 minutes after administration. Tomographic acquisition commenced 20 minutes after administration. During a 360^{o} rotation, image data were accumulated in 64*64 matrices for 15 seconds at each of 64 positions. Immediately following tomographic imaging, planar images of 500 kcounts were recorded in 128*128 matrices in anterior, left anterior oblique and left lateral (decubitus) orientations. Where possible, liver and spleen activity in these images was partially masked by the use of lead rubber sheets. Three to four hours after administration, redistribution images were obtained by repeating the acquisition procedure. Planar images were only recorded for patient sub-group C1. In one of these patients (patient 2) no planar redistribution images were recorded, due to technical failure.

7.3 Image processing and reporting

7.3.1 Experiment 1

All axial slices encompassing the heart were reconstructed using the sharp Shepp-Logan filter (filter 1, Chapter 2). The slices were smoothed once using filter weights of 1-2-1 in three dimensions (filter 1S), and only the smoothed slices were processed further and reported. The slices and planar images were then scaled so that the maximum display level corresponded to the maximum myocardial count. This allowed visualisation of the myocardium without distraction by liver and spleen activity. All possible coronal and sagittal slices were generated interactively from the axial slices when the images were reported (figure 7.2a). Oblique slices through the myocardium were generated from the axial data, prior to reporting; these slices were parallel to a plane through the short axes of the left ventricle and in two orthogonal planes (figure 7.2b). All possible slices

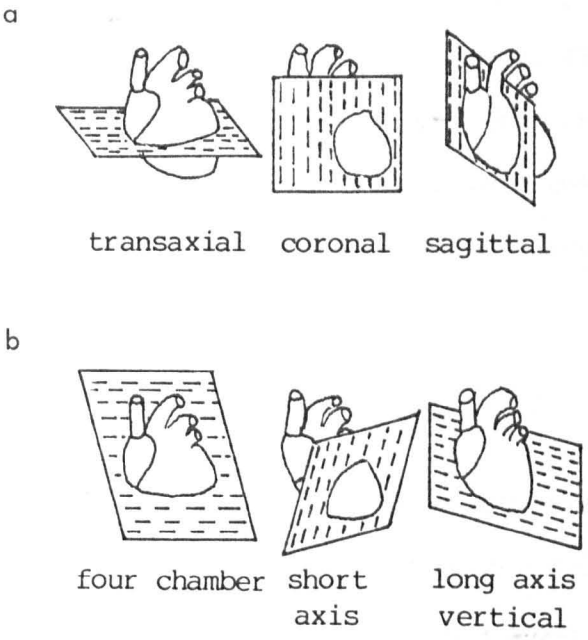

Figure 7.2 Orientations of the image planes. **a:** Transaxial reconstruction. **b:** Oblique reconstruction.

(approximately 9) in each of the three orientations were formed and viewed at reporting (table 7.3). No further processing of planar or reconstructed images was undertaken (figure P7.3).

The patient studies were displayed in a random order and independently reported by an experienced observer and by two other trained observers, without knowledge of the clinical assessment. A 'hot iron' colour scale was used (figure P7.4), with four images displayed on each 256*256 display page. Diagnoses were made from planar images only (p); from planar and conventional tomographic images (i.e. axial, coronal and sagittal slices) (t); and from examination of all images including the oblique slices (o). The diagnoses specified irreversible ischaemia (infarct), (I), or transient ischaemia, (T), within one of five left ventricular myocardial zones; or normal exercise and redistribution images, (N). The five zones were the apex and septum; and the anterior, inferior and postero-lateral (free) walls (figure P7.3).

7.3.2 Experiment 2

From each tomographic acquisition data set axial slices were reconstructed using each of five back projection filters. Four filters (2, 3, 5, and 8) were selected from those discussed in Chapter 2, in addition filter 1S was used. To generate filter 1S axial slices reconstructed using filter 1 were smoothed with a 1-2-1 weighted filter in three dimensions as in Experiment 1. The slices were scaled so that the maximum display level corresponded to the maximum myocardial count in any slice. Four uniformly spaced oblique slices through the myocardium were formed, in each of the three orientations described in figure 7.2b, giving a total of 12 exercise-rest image pairs for each of the filter-patient combinations (figures P7.5-P7.9).

These 100 studies were presented, in random order, to three

Table 7.3 Patient group C

Number of slices in oblique reconstructions

Patient	Exercise-Redistribution Short	Long	4 chamber
1	7 - 6	7 - 9	9 - 8
2	10 - 12	13 - 13	11 - 11
3	9 - 8	10 - 8	9 - 7
4	8 - 8	7 - 6	7 - 7
5	8 - 9	8 - 7	8 - 7
6	11 - 12	9 - 10	9 - 9
7	10 - 12	7 - 7	13 - 10
8	7 - 9	8 - 6	9 - 7
9	9 - 9	8 - 10	8 - 10
10	8 - 9	9 - 9	10 - 9
11	9 - 11	10 - 9	8 - 10
12	8 - 8	9 - 10	7 - 8
13	7 - 9	9 - 8	8 - 9
14	9 - 9	10 - 11	10 - 10
15	6 - 6	9 - 9	8 - 9
16	8 - 8	8 - 7	9 - 8
17	7 - 10	10 - 10	9 - 8
18	8 - 10	10 - 8	8 - 9
19	number of slices not recorded		
20	9 - 7	5 - 7	8 - 7

experienced observers using the 'hot iron' display. Reports were given as in Experiment 1.

7.4 Analysis of reports: Cohen's kappa

To measure the agreement between the imaging diagnoses and the clinical diagnoses the kappa statistic (Cohen, 1960) was used. This is defined as

$$\text{kappa, } \kappa = \frac{p_o - p_c}{1 - p_c} \qquad 7.1$$

where p_o = observed agreement (accuracy) = $\sum_{i=1}^{R} x_{ii}/n$

and p_c = expected agreement = $\sum_{i=1}^{R} n_{1i}n_{2i}/n^2$

for a square RxR contingency table with:

n = total number of observations

n_{1i} = number of observations in row i

n_{2i} = number of observations in column i

x_{ii} = number of observations in cell i,i.

Kappa is approximately normally distributed with standard error:

$$\sigma_\kappa = \sqrt{\frac{p_o(1-p_o)}{n.(1-p_c)^2}} \qquad 7.2$$

Therefore, 95% confidence limits for kappa are: $\sigma_\kappa \pm 1.96$.

To determine the best imaging technique (or filter) after the removal of inter-observer variation, a two way analysis of variance (anova) was performed. The analysis was performed as follows. First, a contingency table of clinical diagnosis (I,T or N) against observers report was drawn up for each imaging technique/observer combination, giving 24 tables. A table pooling all diagnoses was also constructed. Kappa and σ_κ were calculated for each table. Treating kappa as a mean of an arbitrary observation variable, y, for each patient within each table the following relations may be derived:

$$\Sigma(y) = n.\kappa \qquad 7.3$$

and $\Sigma(y^2) = n.\kappa^2 + n.(n-1).\sigma_\kappa^2$ 7.4

since variance(y) $= n.\sigma_\kappa^2$, 7.5

while n = the number of entries in the contingency table.

In effect treating the patients within each contingency table as the group of replicates necessary to compute the interaction term, (observers X techniques), all values needed for the analysis may be calculated. For each of the observer-technique tables the group total was given by $\Sigma(y)$ from equation 7.3, from which technique and observer totals were calculated. The sum of all y-squared terms was obtained from the overall pooled table using equation 7.4.

The statistical hypotheses tested by the anova were:

1. H_o: observers mean kappa scores were equal,
2. H_o: no method-filter X observer interaction,
3. H_o: mean kappa was equal for each imaging technique or filter.

Thus the tests were that the observers were equally good at lesion detection, that there was no change in the performance of any observer for a given filter compared with the other observers and that the different methods and filters gave images which were reported equally well.

Given the experimental design there were 14 planned comparisons of means in the event of rejection of hypothesis 3. These were comparison of the three means of techniques from Experiment 1 (3 comparisons) and comparison of the five means of filters from Experiment 2 (10 comparisons). The final comparison of interest was that between the means from oblique reconstructions using filter 1S in each of the experiments. This comparison was also expected to show a lower false negative reporting rate in Experiment 1 since more oblique slices were formed and planar and transaxial images were also viewed.

7.5 Results

Tables 7.4a-h give the observers diagnoses for each patient and the derived contingency tables. In every case in which a correct diagnosis of infarction or transient ischaemia was made, the location of the ischaemia was correctly identified. The contingency tables show the individual observer's performance and the observers' pooled performance for each imaging method or filter. Table 7.5 gives contingency tables pooled across methods and filters for each observer and the overall pooled table required for computation of the total error variance in the anova.

The kappa and σ_K values from each of the contingency tables were calculated (table 7.6). The homogeneity of variance required for anova was checked by Bartlett's test, after computing the variances from the σ_K values (eqn 7.5). No significant heteroscedasticity was present in the data ($p>0.995$), therefore the anova was performed (table 7.7).

No significant interaction between methods/filters and observers was detected ($p>0.75$) and there were no differences between the observers ($p>0.5$). However, there were significant differences between the imaging techniques-filters ($p=0.0192$).

To determine the least significant difference, LSD, between methods Sidak's multiplicative inequality was used to ensure that total probability of error (experimentwise error rate) was less than $p=0.0192$ (Sokal and Rohlf, 1981). This inequality, $p' \leq 1 - (1-p)^{1/14}$, implies that for $p=0.0192$ each comparison should be performed with $p'=0.0014$. The estimated standard error, SE, was computed from the interaction mean square from the anova.

Thus, $LSD = (t_{.0014,14}) \times (SE) = 0.0875$.

The specificity and separate sensitivities for the detection of infarction and transient ischaemia were calculated for each imaging technique and filter (table 7.8). This table also gives the accuracy,

Table 7.4a Patient group C1, observers' diagnoses and contingency tables

Planar imaging

Patient	Observer 1	2	3	Expected appearance
2	-	-	-	I ant/apex
3	I inf	T inf	I inf	T inf
4	N	N	N	T inf
5	T apex	N	N	N
6	I apex	I apex	I apex	I apex
7	I apex	I apex	I apex	I ant/apex
9	I apex/inf	N	N	N
10	N	N	N	N
11	T inf	I inf	N	I inf
12	I inf	N	N	I inf
13	N	N	N	N
15	N	N	N	I inf

Observer's diagnosis	Observer 1 Clinical diagnosis I	T	N	Observer 2 Clinical diagnosis I	T	N
I	3	1	1	3	0	0
T	1	0	1	0	1	0
N	1	1	2	2	1	4

Observer's diagnosis	Observer 3 Clinical diagnosis I	T	N	Pooled Clinical diagnosis I	T	N
I	2	1	0	8	2	1
T	0	0	0	1	1	1
N	3	1	4	6	3	10

I=irreversible ischaemia (infarct)
T=transient ischaemia
N=no abnormality
ant, apex, free, sept, inf; involvement of anterior, apical, free, septal and/or inferior walls of the left ventricle

Table 7.4b Patient group C1, observers' diagnoses and contingency tables

Transaxial tomography

Patient	Observer 1	2	3	Expected appearance
2	I ant/apex	I ant/apex	I ant/apex	I ant/apex
3	T inf	T inf	I inf	T inf
4	N	N	N	T inf
5	I apex/inf	N	N	N
6	I apex	I apex	I apex	I apex
7	I apex	I apex	I apex	I ant/apex
9	I apex/inf	N	N	N
10	N	N	N	N
11	T inf	T inf	I inf	I inf
12	I inf	I inf	N	I inf
13	N	N	N	N
15	I inf/free	N	T inf	I inf

Observer's diagnosis	Observer 1 Clinical diagnosis I	T	N	Observer 2 Clinical diagnosis I	T	N
I	6	0	2	4	0	0
T	0	1	0	1	1	0
N	0	1	2	1	1	4

Observer's diagnosis	Observer 3 Clinical diagnosis I	T	N	Pooled Clinical diagnosis I	T	N
I	4	1	0	14	1	2
T	1	0	0	2	2	0
N	1	1	4	2	3	10

I=irreversible ischaemia (infarct)
T=transient ischaemia
N=no abnormality
ant, apex, free, sept, inf; involvement of anterior, apical, free, septal and/or inferior walls of the left ventricle

Table 7.4c Patient group C1, observers' diagnoses and contingency tables

Oblique reconstructions

Patient	Observer 1	2	3	Expected appearance
2	I ant/apex	I ant/apex	I ant/apex	I ant/apex
3	T inf	T inf	T inf	T inf
4	N	N	N	T inf
5	I inf/apex	I inf/sept	I inf	N
6	I apex	I apex	I apex	I apex
7	I apex	I apex	I apex	I ant/apex
9	N	N	N	N
10	N	N	N	N
11	I inf	I inf/apex	I inf	I inf
12	I inf	I inf	I inf	I inf
13	N	N	N	N
15	I inf/free	I inf/sept	I inf	I inf

Observer's diagnosis	Observer 1 Clinical diagnosis			Observer 2 Clinical diagnosis		
	I	T	N	I	T	N
I	6	0	1	6	0	1
T	0	1	0	0	1	0
N	0	1	3	0	1	3

Observer's diagnosis	Observer 3 Clinical diagnosis			Pooled Clinical diagnosis		
	I	T	N	I	T	N
I	6	0	1	18	0	3
T	0	1	0	0	3	0
N	0	1	3	0	3	9

I=irreversible ischaemia (infarct)
T=transient ischaemia
N=no abnormality
ant, apex, free, sept, inf; involvement of anterior, apical, free, septal and/or inferior walls of the left ventricle

Table 7.4d Patient group C, observers' diagnoses and contingency tables

Filter 1S

Patient	Observer 1	2	3	Expected appearance
1	N	N	N	N
2	I ant/apex	I ant/apex	I ant/apex	I ant/apex
3	T inf	I inf	N	T inf
4	N	N	N	T inf
5	N	N	N	N
6	I ant/apex	I ant/apex	I ant/apex	I apex
7	I ant	I ant	I ant	I ant/apex
8	N	N	N	N
9	N	N	N	N
10	N	N	N	N
11	I inf	I inf	I inf	I inf
12	T inf	I inf/sept	T inf	I inf
13	N	N	N	N
14	I inf	I inf	I inf	I inf
15	T inf	T inf	N	I inf
16	N	N	N	N
17	I inf	I inf	N	I inf
18	I ant/apex	I apex	I ant/apex	I apex
19	N	N	N	N
20	N	N	T apex	N

Observer's diagnosis	Observer 1 Clinical diagnosis I	T	N	Observer 2 Clinical diagnosis I	T	N
I	7	0	0	8	1	0
T	2	1	0	1	0	0
N	0	1	9	0	1	9

Observer's diagnosis	Observer 3 Clinical diagnosis I	T	N	Pooled Clinical diagnosis I	T	N
I	6	0	0	21	1	0
T	1	0	1	4	1	1
N	2	2	8	2	4	26

I=irreversible ischaemia (infarct)
T=transient ischaemia
N=no abnormality
ant, apex, free, sept, inf; involvement of anterior, apical, free, septal and/or inferior walls of the left ventricle

Table 7.4e Patient group C, observers' diagnoses and contingency tables

Filter 2

Patient	Observer 1	2	3	Expected appearance
1	N	I sept	N	N
2	I apex/sept	I ant/apex	I apex	I ant/apex
3	T inf	I inf	T inf	T inf
4	N	T sept	N	T inf
5	T apex	N	T sept	N
6	I ant/apex	I apex	I apex	I apex
7	I ant/apex	I ant	I ant	I ant/apex
8	N	N	N	N
9	N	N	N	N
10	N	N	N	N
11	I inf	I inf	I inf	I inf
12	I inf	I inf	N	I inf
13	N	N	N	N
14	I inf	I inf	I inf	I inf
15	T inf	T sept	N	I inf
16	N	N	N	N
17	I inf	N	N	I inf
18	I apex/inf	I apex	I apex	I apex
19	N	N	N	N
20	N	N	N	N

Observer's diagnosis	Observer 1 Clinical diagnosis			Observer 2 Clinical diagnosis		
	I	T	N	I	T	N
I	8	0	0	7	1	1
T	1	1	1	1	1	0
N	0	1	8	1	0	8

Observer's diagnosis	Observer 3 Clinical diagnosis			Pooled Clinical diagnosis		
	I	T	N	I	T	N
I	6	0	0	21	1	1
T	0	1	1	2	3	2
N	3	1	8	4	2	24

I=irreversible ischaemia (infarct)
T=transient ischaemia
N=no abnormality
ant, apex, free, sept, inf; involvement of anterior, apical, free, septal and/or inferior walls of the left ventricle

Table 7.4f Patient group C, observers' diagnoses and contingency tables

Filter 3

Patient	Observer 1	2	3	Expected appearance
1	N	I sept	N	N
2	I apex	I ant/apex	I apex	I ant/apex
3	N	N	T inf	T inf
4	N	N	N	T inf
5	N	N	N	N
6	I apex	I apex	I apex	I apex
7	I ant	I ant	I ant	I ant/apex
8	N	N	N	N
9	N	N	T sept	N
10	N	I sept	N	N
11	I inf	I inf	I inf	I inf
12	I inf	N	T inf	I inf
13	T inf	N	N	N
14	I inf	I inf	I inf	I inf
15	T inf	T inf	T inf	I inf
16	N	N	N	N
17	T inf	N	T inf	I inf
18	I apex	I apex	I apex	I apex
19	N	N	N	N
20	N	N	N	N

Observer's diagnosis	Observer 1 Clinical diagnosis			Observer 2 Clinical diagnosis		
	I	T	N	I	T	N
I	7	0	0	6	0	2
T	2	0	1	1	0	0
N	0	2	8	2	2	7

Observer's diagnosis	Observer 3 Clinical diagnosis			Pooled Clinical diagnosis		
	I	T	N	I	T	N
I	6	0	0	19	0	2
T	3	1	1	6	1	2
N	0	1	8	2	5	23

I=irreversible ischaemia (infarct)
T=transient ischaemia
N=no abnormality
ant, apex, free, sept, inf; involvement of anterior, apical, free, septal and/or inferior walls of the left ventricle

Table 7.4g Patient group C, observers' diagnoses and contingency tables

Filter 5

Patient	Observer 1	2	3	Expected appearance
1	N	I sept	N	N
2	I ant/apex	I ant/apex	I ant/apex	I ant/apex
3	N	I inf	T inf	T inf
4	N	N	N	T inf
5	N	N	N	N
6	I apex	I apex	I apex	I apex
7	I ant/free	I ant	I ant	I ant/apex
8	N	N	N	N
9	N	N	N	N
10	N	T sept	N	N
11	I inf	I inf	I inf	I inf
12	I inf	I inf	N	I inf
13	N	N	N	N
14	I inf	I inf	I inf	I inf
15	T inf	T sept	N	I inf
16	N	N	N	N
17	N	N	N	I inf
18	I apex/inf	I apex	I apex	I apex
19	N	N	N	N
20	N	N	N	N

Observer's diagnosis	Observer 1 Clinical diagnosis I	T	N	Observer 2 Clinical diagnosis I	T	N
I	7	0	0	7	1	1
T	1	0	0	1	0	1
N	1	2	9	1	1	7

Observer's diagnosis	Observer 3 Clinical diagnosis I	T	N	Pooled Clinical diagnosis I	T	N
I	6	0	0	20	1	1
T	0	1	0	2	1	1
N	3	1	9	5	4	25

I=irreversible ischaemia (infarct)
T=transient ischaemia
N=no abnormality
ant, apex, free, sept, inf; involvement of anterior, apical, free, septal and/or inferior walls of the left ventricle

Table 7.4h Patient group C, observers' diagnoses and contingency tables

Filter 8

Patient	Observer 1	2	3	Expected appearance
1	T sept	T sept	T sept	N
2	I apex	I ant/apex	I apex	I ant/apex
3	T inf	I inf	N	T inf
4	T sept	T sept	N	T inf
5	T inf/sept	N	T sept	N
6	I apex	I apex/sept	I apex	I apex
7	I ant	I ant	N	I ant/apex
8	T sept	T sept	N	N
9	N	N	N	N
10	T sept	T sept	N	N
11	I inf	I inf	I inf	I inf
12	I inf	I inf/sept	T apex/sept	I inf
13	N	N	N	N
14	I inf	I inf/free	I inf	I inf
15	T inf	N	N	I inf
16	N	I sept	N	N
17	N	I inf	N	I inf
18	T apex	N	I ant/apex	I apex
19	N	N	N	N
20	N	N	N	N

Observer's diagnosis	Observer 1 Clinical diagnosis I	T	N	Observer 2 Clinical diagnosis I	T	N
I	6	0	0	7	1	1
T	2	2	4	0	1	3
N	1	0	5	2	0	5

Observer's diagnosis	Observer 3 Clinical diagnosis I	T	N	Pooled Clinical diagnosis I	T	N
I	5	0	0	18	1	1
T	1	0	2	3	3	9
N	3	2	7	6	2	17

I=irreversible ischaemia (infarct)
T=transient ischaemia
N=no abnormality
ant, apex, free, sept, inf; involvement of anterior, apical, free, septal and/or inferior walls of the left ventricle

Table 7.5 Patient group C, contingency tables

All methods/filters pooled

Observer's diagnosis	Observer 1 Clinical diagnosis			Observer 2 Clinical diagnosis		
	I	T	N	I	T	N
I	50	1	4	48	4	6
T	9	6	7	5	5	4
N	3	9	46	9	7	47

Observer's diagnosis	Observer 3 Clinical diagnosis			Pooled Clinical diagnosis		
	I	T	N	I	T	N
I	41	2	1	139	7	11
T	6	4	5	20	15	16
N	15	10	51	27	26	144

I=irreversible ischaemia (infarct)
T=transient ischaemia
N=no abnormality

Table 7.6 Kappa statistics

κ, σ_κ for all methods/filters for each observer. Values from contingency tables pooled over the three observers are given.

	Number of patients n	Observer 1	2	3	Pooled (number = 3n)
Method p	11	.13 , .239	.57 , .213	.26 , .246	.32 , .138
Method t	12	.56 , .220	.61 , .196	.45 , .223	.54 , .123
Method o	12	.71 , .184	.71 , .184	.71 , .184	.71 , .107
Filter 1S	20	.75 , .133	.74 , .141	.49 , .175	.66 , .088
Filter 2	20	.75 , .133	.66 , .153	.57 , .166	.66 , .087
Filter 3	20	.59 , .161	.38 , .188	.61 , .152	.53 , .097
Filter 5	20	.65 , .158	.49 , .175	.65 , .158	.59 , .095
Filter 8	20	.49 , .155	.44 , .175	.34 , .182	.42 , .098
Pooled over all methods/filters and observers (n=405):					κ = .56 σ_κ = .036

p = planar imaging
t = transaxial tomography
o = oblique reconstruction

Table 7.7 Anova table

Source	Model	SS	df	MS	F	P
Methods/filters	Fixed	5.4057	7	.7722	3.560	.0192
Observers	Random	0.6128	2	.3064	.562	.5<P<.75
Interaction		3.0370	14	.2169	.398	.75<P
Error		207.9012	381	.5457		
Total		216.9567	404			

Table 7.8 Reporting rates

Sensitivity and specificity are reported as percentages of totals in each clinical diagnosis category (I,T or N). Accuracy and false reporting rates are expressed as percentages of the total number of reports.

		Sensitivity (I)	(T)	Specificity (N)	Accuracy	False reports Positive	Negative
Method	p	53	17	83	58	30	12
	t	78	33	83	72	20	8
	o	100	50	75	84	8	8
Filter	1S	78	17	96	80	3	17
	2	78	50	89	80	7	13
	3	70	17	85	71	7	22
	5	74	50	93	77	5	18
	8	67	50	63	64	18	18

the false positive rate and the false negative rate for each imaging technique and filter. The values in table 7.8 were computed from the pooled contingency tables for each imaging technique and filter (tables 7.4a-h). Accuracy was defined, according to convention, as the number of reports falling on the leading diagonal expressed as a percentage of the total number of reports for each imaging technique or filter. False positive was defined as a report of one or more lesions at either exercise or rest when none was expected on clinical grounds, i.e. an entry above and to the right of the correct diagnosis diagonal. False negative studies were those in which an observer failed to report an expected lesion on either exercise or rest images, i.e. entered in contingency tables below and left of the diagonal. For example, if the clinical diagnosis for a particular patient was transient ischaemia then an observer's report of infarction meant that the observer falsely reported the presence of a lesion on the rest images.

7.5.1 Experiment 1

The pooled kappa values (across the three observers) were significantly greater than 0 and indicated moderate, good and excellent agreement between the clinical diagnosis and diagnoses from the imaging methods p, t and o, respectively. Comparison of the pooled kappa values (table 7.6) in pairs using the LSD indicated significant differences between the imaging methods. Reports from oblique reconstructions gave better agreement with the clinical diagnoses than either of the other two methods, while transaxial tomography (with coronal and sagittal images) was better than planar imaging. Furthermore, agreement between the observers' diagnoses was total when reporting from the oblique slices (table 7.4c).

In two cases the reports based on reconstructed oblique slices did not agree with the clinical diagnoses. Patient 5 (figure P7.10) was

admitted to the coronary care unit for investigation of chest pain. Serial and exercise electrocardiographic tests were normal, as were cardiac enzyme studies. There was no history of previous infarction. Oblique reconstruction tomography showed a transmural inferior wall defect with some slight involvement of the antero-apical wall and septum. Patient 4 (figure P7.11) had equivocal ST segment changes on exercise ECG, and was referred for coronary arteriography which demonstrated triple vessel disease. However, no ST changes were observed during the bicycle exercise of the nuclear medicine study and no abnormalities were seen in the myocardial images. This patient had a poor symptomatic response to subsequent coronary artery bypass graft surgery, suggesting that the pain which was the original cause of referral was unrelated to the stenoses.

Ignoring data from patient 4 with triple vessel disease, there were four cases of clinically diagnosed inferior wall disease (table 7.2) and, therefore, 12 reports were given for each imaging technique (table 7.4a-c). The number of correct diagnoses for planar imaging only was 3, for transaxial tomography 7, and for oblique reconstructions there were 12 correct diagnoses of inferior wall disease. Using McNemar's test with Yate's correction (Sokal and Rohlf, 1981) to compare the changes in diagnoses between imaging methods, no significant differences between planar imaging and transaxial tomography were found ($p>0.1$), but oblique reconstruction tomography was significantly better than transaxial tomography ($p<0.05$).

7.5.2 Experiment 2

The pooled kappa values were again significantly greater than 0. The kappa values indicated a range of agreement between the clinical diagnosis and the observer's diagnoses from the oblique slices using the different reconstruction filters. The rank order of the filters, in

order from poorest to best agreement, was 8,3,5,1S,2. Comparison of the pooled kappa values (table 7.6) in pairs using the LSD indicated significant differences between the following sets:

{8} {3,5} {5,1S,2}

The minimum LSD which separated filter 5 from filter 1S was 0.0651, corresponding to an experimentwise error rate of p=0.168.

Filter 2 gave a lower false negative rate than either filter 1S or filter 5, with a correspondingly higher false positive rate (table 7.8). In order to test whether filter 2 was significantly more conservative than filters 1 and 5 contingency tables were drawn up from the observers reports of the separate exercise and rest studies (table 7.9). McNemar's test was used to compare the changes in diagnoses between filters. No significant changes were found (p=0.14).

7.5.3 Comparison of applications of filter 1S

No significant difference between the mean kappa values obtained in each of the two experiments was observed for filter 1S (table 7.6). The minimum LSD required to separate the means was 0.0562, corresponding to an experimentwise error rate of p=0.313.

The use of filter 1S in experiment 2, without planar or transaxial data and with fewer oblique slices, gave a higher false negative rate and a lower false positive rate than in experiment 1 (table 7.8). Contingency tables were drawn up from the observers reports of the separate exercise and rest studies, for the 12 patients common to the two experiments (table 7.10). McNemar's test showed that there were significant changes in diagnoses between the two applications of the filter ($p<0.001$).

Table 7.9 Contingency tables from exercise and rest studies

Experiment 2

		Filter 2	
		Lesion	No lesion
Filter 1S	Lesion	46	4
	No lesion	7	63

		Filter 2	
		Lesion	No lesion
Filter 5	Lesion	47	1
	No lesion	6	66

		Filter 5	
		Lesion	No lesion
Filter 1S	Lesion	43	7
	No lesion	5	65

Table 7.10 Contingency tables from exercise and rest studies

Comparison of applications of filter 1S

		Experiment 1	
		Lesion	No lesion
Experiment 2	Lesion	32	1
	No lesion	13	26

7.6 Discussion

The assessment of myocardial perfusion with thallium-201 is a useful clinical tool in the management of patients with coronary artery disease. Technetium-99m labelled t-butyl isonitrile has been shown to share with ^{201}Tl the useful properties of distribution proportional to blood flow in hyperaemic, ischaemic and normal zones, and of redistribution following transient ischaemia (Holman et al, 1986). Therefore, $^{99}Tc^{m}$-tBIN will allow differentiation of reversible ischaemia from infarction and scar tissue following a single injection.

The disadvantages of $^{99}Tc^{m}$-tBIN are high initial lung uptake and high liver uptake of the agent (Holman et al, 1984; Gerundini et al, 1986; Holman et al, 1986). The initial distribution in the lungs causes a reduction in contrast in the early images but the use of emission tomography allows visualisation of the myocardial wall without major interference from surrounding lung activity. The high liver uptake has been reported as a possible source of error in the diagnosis of inferior wall defects (Campbell et al; 1986). Liu and colleagues (1987) have used an interpolative background subtraction algorithm to obtain clear separation of the inferior wall and the liver in planar images. Although no processing of planar images was performed, the present study has shown that inferior wall disease can be accurately diagnosed in the presence of high liver uptake by the oblique reconstruction of tomographic data.

In experiment 2 the effectiveness of five of the filters discussed in Chapter 2 was compared. Filters 1S and 2 gave approximately equal smoothing (suppression of high spatial frequencies), filter 5 gave slighly less smoothing, filter 3, the ramp, gave no smoothing, and filter 8 gave enhancement of low spatial frequencies without high frequency suppression. The results clearly show that smoothing of the data, rather than low frequency enhancement, is necessary for clinical

studies using $^{99}Tc^{m}$-tBIN (see Chapter 8).

In conclusion, $^{99}Tc^{m}$-tBIN offers a useful alternative to the use of thallium-201 in the diagnosis of regional impairment of myocardial perfusion. The myocardial perfusion of $^{99}Tc^{m}$-tBIN is best demonstrated by means of oblique reconstruction of transaxial tomograms.

8. Evaluation of back-projection filters using phantoms

In order to investigate the performance of different back-projection filters under conditions similar to those found in the clinical studies of myocardial perfusion with technetium-99m labelled tertiary butyl isonitrile ($^{99}Tc^{m}$-tBIN) described in Chapter 7, two phantoms were used.

The first, a rod phantom (figure 8.1), was constructed as a perspex cylinder of internal diameter 200 mm and internal length 100 mm. The walls of the phantom were 8mm thick. Eight hollow rods of differing internal diameters with walls 1mm thick were arranged axially within the phantom. Each of the eight rods and the main chamber could be filled with fluid independently of the others.

The second phantom (figure 8.2) was also a perspex cylinder, with internal diameter 200 mm, internal length 140 mm and wall thickness 14 mm. This phantom was divided internally into two large volumes and one small volume by an obliquely positioned elliptical chamber. This chamber had walls 1 mm thick and a constant wall separation of 11 mm. Within it were located five hollow cylinders of varying internal diameters, with walls 1 mm thick. These cylinders, the elliptical slice and each of the two larger volumes could be filled independently of the other chambers.

Clinical tomographic imaging with $^{99}Tc^{m}$-tBIN was performed using 400 MBq of the agent. Projections of 15 s at each of 64 angles in a 360^{o} rotation were acquired (Section 7.2). In order to simulate these conditions each phantom was filled with a solution containing $^{99}Tc^{m}$-pertechnetate. The activity concentration required in the section of each phantom simulating myocardial uptake was 310 kBq ml^{-1} for an acquisiition time of 1 s at each angle. Thus, if a concentration of 62 kBq ml^{-1} were used, projections were acquired for 5 s at each angle. This figure was derived from the areas of the phantoms relative to the gamma camera field of view and validated by examination of the counts in

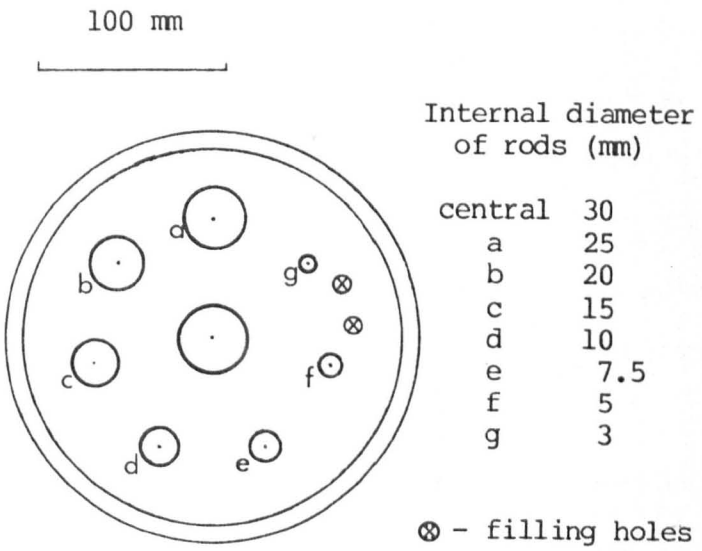

Figure 8.1 Plan view of rod phantom showing the disposition and sizes of the rods.

a

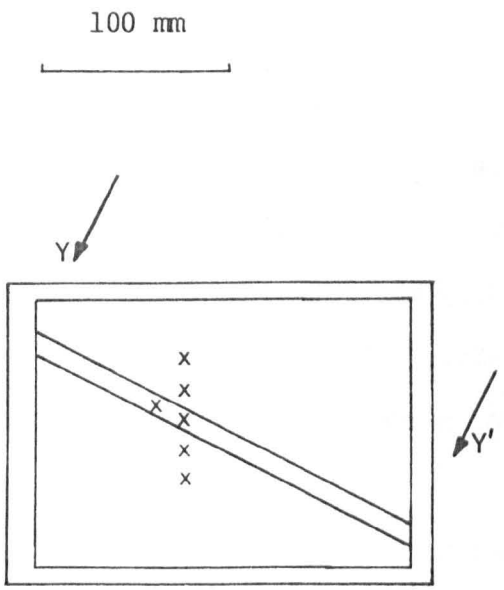

b

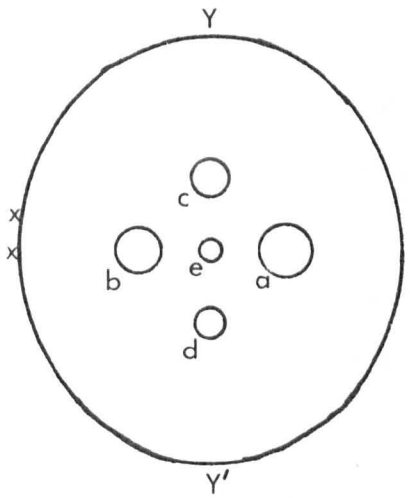

Internal diameter of lesions (mm)	
a	20
b	15
c	10
d	7.5
e	5

x - filling holes

Figure 8.2 The slice phantom. **a:** Elevation, showing slice orientation. **b:** Plan of the slice showing the disposition and sizes of the lesions.

projection images and the counts per pixel in reconstructed axial slices in phantom and patient studies.

8.1 Acquisition and processing: rod phantom

The largest volume of the phantom was filled as above to simulate myocardial uptake and five acquisitions of 64 projection images in 64*64 matrices were recorded. For each of the five acquisitions all rods were filled in turn with solutions containing 0.0, 0.0625, 0.125, 0.25 and 0.5 times the 'myocardial' activity concentration to simulate perfusion defects of varying severity.

The five raw data sets were reconstructed as axial slices using each of six back-projection filters (1,2,3,4,5,8) described in Section 2.6.1. A further filter (1S) was generated by three-dimensional 1-2-1 weighted smoothing of the axial slices from filter 1. There were, therefore, a total of 35 axial slice data sets. Following attenuation correction of the projection data (Bellini et al, 1979), a further 35 axial slice data sets were formed (figure P8.3).

The central slice of each of these 70 axial data sets was then processed to quantify lesion detectability for each filter - concentration combination. Three circular regions of interest (ROI) were defined. These ROIs were positioned so as to be concentric with each axial slice (figure P8.4). The radii of the ROIs were 5, 6 and 13 pixels (i.e. 31, 38 and 81 mm). A fourth region was defined as the difference between the two smaller ROIs. This ROI enclosed the volume of the phantom between the central rod and the circle of rods. The mean (M) and standard deviation (S) of the counts within this ROI in each slice were calculated. The counts in each pixel within the largest ROI were then normalised by subtracting M, dividing by S and taking the absolute value of the result. A 'deviation image' was formed in this way from the central slice of each data set. Each deviation image was

scaled so that the maximum display level (100%) was equal to 10 standard deviation (sd) units. Thus these images showed how far, in standard deviation units, any pixel count deviated from the mean count in the largest chamber of the phantom.

Each deviation image was examined and the sizes of the smallest rods in which at least one pixel deviated from the mean by more than one and two standard deviations were recorded. The peak deviation was also recorded for these rods as % maximum display level (equal to 10 times the deviation in sd units). The data were analyzed by Friedman's two way analysis of variance by ranks. Back-projection filters gave the 'treatment effects' while the concentrations in the rods were the 'experimental conditions'. Ranks were computed within concentrations by ordering the filters by smallest detected rod at each of the two cut offs chosen (1sd and 2sd). In cases where the size of the smallest detected rod was equal for two or more filters the peak deviation was used to rank these filters.

8.2 Results: rod phantom

Table 8.1 gives the size of the smallest detectable rod at each cut off and the peak deviation of that rod for each filter - concentration combination. For each filter, except 8, there was a clearly discernible increase in rod detectability with increasing concentration difference. Furthermore, rod detectability at a given cut off was improved by attenuation correction of the data.

The results of the analyses of variance are given in table 8.2. Filters are ordered from worst at the top to best at the bottom, with vertical lines to show sets of filters not differing significantly ($p > 0.05$). Also given are the probability values derived from the analyses.

There were no significant differences between the rank order of the

Table 8.1 Rod phantom: deviation images

Size of smallest rod (mm), peak deviation (%).

Peak deviation (%) = 10 * peak deviation (sd units).

Derived at cutoff levels of 1sd and 2sd from images not attenuation corrected (N) and corrected (A) with solutions at five concentrations in the rods.

Cutoff level	Attenuation correction	Filter	Concentration, Rod : 'Myocardial' 0:1	0.0625:1	0.125:1	0.25:1	0.5:1
1sd	N	1	10, 24	10, 28	10, 14	15, 19	15, 18
		1S	10, 15	10, 17	15, 34	15, 31	15, 15
		2	10, 21	10, 16	15, 35	15, 20	20, 23
		3	10, 23	10, 28	10, 14	15, 19	15, 19
		4	10, 23	10, 27	10, 14	15, 19	15, 17
		5	10, 20	10, 19	10, 11	15, 22	15, 13
		8	20, 24	15, 22	15, 11	15, 12	20, 26
	A	1	10, 33	10, 35	10, 27	15, 27	15, 31
		1S	7.5, 12	10, 49	10, 33	10, 17	10, 29
		2	5, 18	10, 30	10, 45	15, 40	10, 19
		3	10, 30	10, 35	10, 23	15, 25	15, 31
		4	10, 34	10, 36	10, 30	15, 28	15, 33
		5	5, 16	10, 34	10, 46	15, 37	15, 36
		8	10, 31	10, 34	10, 35	15, 33	15, 32
2sd	N	1	10, 24	10, 28	15, 29	20, 32	20, 34
		1S	15, 26	15, 46	15, 34	15, 31	20, 35
		2	10, 21	15, 40	15, 35	15, 20	20, 23
		3	10, 23	10, 28	15, 28	20, 29	20, 34
		4	10, 23	10, 27	15, 29	20, 33	20, 34
		5	10, 20	15, 37	15, 35	15, 22	20, 28
		8	20, 24	15, 22	20, 36	20, 26	20, 26
	A	1	10, 33	10, 35	10, 27	15, 27	15, 31
		1S	10, 37	10, 49	10, 33	15, 57	10, 29
		2	10, 42	10, 30	10, 45	15, 40	15, 33
		3	10, 30	10, 35	10, 23	15, 25	15, 31
		4	10, 34	10, 36	10, 30	15, 28	15, 33
		5	10, 40	10, 34	10, 46	15, 37	15, 36
		8	10, 31	10, 34	10, 35	15, 33	15, 32

Table 8.2 Rod phantom: analysis

Results of analysis of data in table 8.1 by Friedman's two way analysis of variance by ranks.

Attenuation correction	Cut off level: 1sd Filter+	p*	2sd Filter	p
N	8 2 1S 5 4 3	<0.025 >0.1	8 2 5 3 4 1S	>0.05
	1	<0.025	1	<0.01
A	3 1 8 4 5 2 1S	>0.35 <0.05 >0.1	3 1 8 4 2 5 1S	<0.025 >0.05

\+ filter numbers listed below from poorest to best rod detection. The vertical lines indicate those sets of filters within which there were no significant differences between filters (p>0.05).

* probability values within filter sets (>) and between sets (<).

filters at the two cut off levels, although as expected the smallest detectable rods were never larger at the 1sd cut off than at the 2sd cut off.

8.3 Acquisition and processing: slice phantom

Two experiments, 1 and 2, were performed with this phantom. For Experiment 1 the two large chambers and the slice were filled with solution at a concentration to simulate myocardium, as described above. The five cylindrical lesions were filled with water containing no radioactivity. The phantom was filled in this manner three times and after each filling two sets of projection images of 64 angles were acquired in 128*128 matrices.

For Experiment 2 the slice was filled to simulate myocardium. One large chamber, intended to simulate the intraventricular blood pool after clearance of the $^{99}Tc^{m}$-tBIN, and the lesions, were filled with water containing no activity. To simulate adjacent tissues, such as liver or lung, containing $^{99}Tc^{m}$-tBIN, the second large chamber was filled with solutions at 0.5, 1.0 and 2.0 times the 'myocardial' activity concentration. Two sets of projection images in 128*128 matrices were recorded at each concentration. Thus there was a total of six acquisitions of 64 projections in Experiment 2.

In both experiments a number of small sources of 3.0 times the slice concentration were positioned around the outside of the phantom as reference markers to indicate the location and orientation of reconstructed oblique slices.

The 128*128 matrices were packed to 64*64 matrices by summing groups of 4 pixels in both of the ways indicated in figure 8.5. This simulated offsetting the phantom by one 128*128 pixel (about 3 mm) along the axis of rotation. Thus, for each experiment, there were a total of 12 sets of 64 angle projection images in 64*64 matrices.

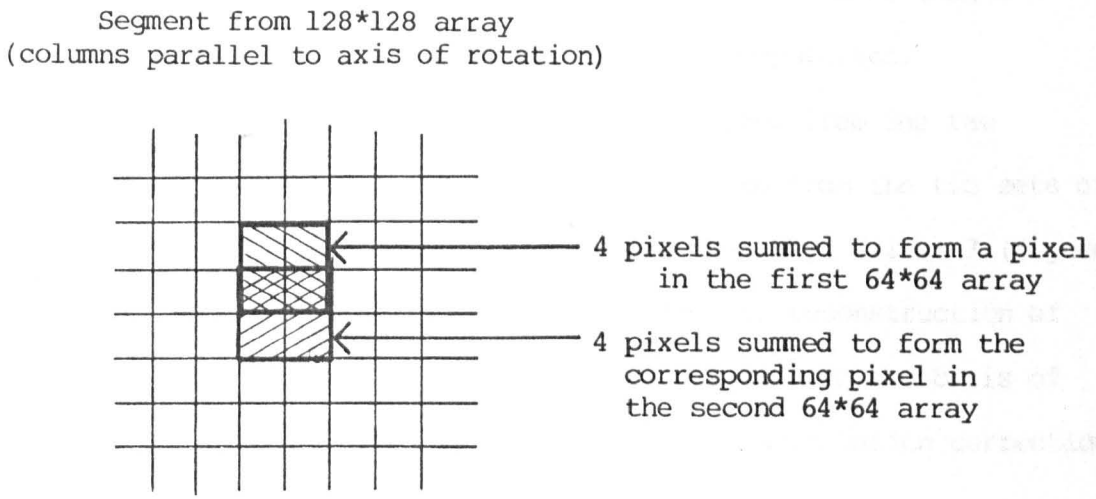

Figure 8.5 Packing a 128*128 matrix

These projection images were smoothed with a two-dimensional 1-2-1 weighted filter (SMTH) and with a variable smoothing filter (VSMO). The variable filter computes for each pixel, p(x,y), the average of the counts in the surrounding pixels such that:

(a) the distribution of pixels is circularly symmetrical about p(x,y) with maximum radius 3 pixels,

(b) the total count in the pixels used to compute the average is 3 times the maximum count in any pixel of the 64 projection images,

(c) pixels in which the count differs from p(x,y) by more than 4 standard deviations are excluded from the computation.

In experiment 1 axial slices were reconstructed from the raw projections using filters 1, 1S, 2, 3, 5 and 8, and from the two sets of smoothed projection images (SMTH, VSMO) using the ramp, filter 3 (figure P8.6). Filters 1, 1S, 2, 5, SMTH were selected for reconstruction of axial slices in experiment 2. The selection was made on the basis of the results of experiment 1. In both experiments attenuation correction was applied to all data (Bellini et al, 1979).

An oblique image in the plane of the lesions, as in figure P8.7, was formed from each axial slice data set and an elliptical ROI defined. The mean and standard deviation of the counts within the ROI were used to generate a normalised deviation image from each oblique image.

8.4 Results: slice phantom

8.4.1 Experiment 1

Noise, as peak deviation outside all lesions, was recorded for each image (table 8.3). The size of the smallest observable lesion and its peak deviation were also recorded (table 8.3). Using the data from each pair of deviation images derived from the same 128*128 matrix acquisition as replicates, a two way analysis of variance was performed on the noise values (table 8.4). The requirement for homoscedasticity in analysis of variance was tested by

Table 8.3 Slice phantom, experiment 1: deviation images

a) Size of smallest rod (mm) : peak deviation (%).

Derived at a cut off level of 1sd from attenuation corrected data.

Data acquired as 6 128*128 projection image sets and packed into 2 64*64 sets (a & b).

	Acquisition: 1		2		3		4		5		6	
Filter	a	b	a	b	a	b	a	b	a	b	a	b
1	15:19	15:12	15:35	10:24	+	20:20	15:19	15:20	15:17	20:24	15:20	+
1S	15:27	15:20	10:17	10:24	15:22	15:21	10:14	10:10	15:17	10:12	15:25	15:27
2	15:31	20:20	10:15	7.5:18	15:14	15:26	15:28	15:17	10:16	10:18	15:33	15:29
3	15:18	15:12	15:33	10:24	+	20:18	15:14	15:21	15:18	20:24	15:19	+
5	15:27	15:16	10:14	7.5:16	+	15:28	10:11	15:18	15:14	10:16	15:32	15:27
8	15:24	15:14	15:27	7.5:18	+	15:31	15:18	15:15	15:14	15:15	15:22	+
SMTH	15:31	15:24	7.5:14	10:27	15:20	15:21	10:14	10:14	15:15	10:12	10:18	10:12
VSMO	15:27	15:21	7.5:20	10:18	+	15:12	10:14	15:23	15:12	10:10	15:20	15:26

\+ no lesion deviating by 1sd or more

b) Noise as peak deviation not in any lesion (%)

	Acquisition: 1		2		3		4		5		6		
Filter	a	b	a	b	a	b	a	b	a	b	a	b	mean
1	30	28	30	25	28	30	26	35	38	28	26	31	29.58
1S	30	30	34	32	40	39	31	31	27	25	31	29	31.58
2	31	30	32	29	40	32	31	31	25	26	33	33	31.08
3	31	29	30	27	27	31	26	37	33	28	27	34	30.00
5	31	32	28	28	35	32	31	26	28	25	33	33	30.17
8	29	41	42	43	52	49	37	40	38	33	28	37	39.08
SMTH	29	33	33	31	41	36	31	30	30	28	31	28	31.75
VSMO	30	40	39	36	43	44	28	28	35	33	29	27	34.33
pooled mean	31.00		31.00		35.57		30.14		29.21		30.36		

Table 8.4 Slice phantom, experiment 1: peak noise analysis of variance

a) All filters

Source	Model	SS	df	MS	F+	p
Filters	Fixed	835.0	7	119.3	5.4	<.001
Acquisitions	Random	581.2	5	116.2	10.6	<<.001
Interaction		774.6	35	22.1	2.0	.025
Error		520.5	48	10.8		
Total		2711.2	95			

b) Excluding filter 8

Source	Model	SS	df	MS	F+	p
Filters	Fixed	184.8	6	30.8	1.6	>.1
Acquisitions	Random	349.4	5	69.9	7.6	<.001
Interaction		575.9	30	19.2	2.1	.025
Error		386.0	42	9.2		
Total		1496.1	83			

c) Excluding filters 8 and VSMO

Source	Model	SS	df	MS	F+	p
Filters	Fixed	48.6	5	9.7	0.7	>.1
Acquisitions	Random	223.3	5	44.7	4.9	<.005
Interaction		352.4	25	14.1	1.6	>.1
Error		327.0	36	9.1		
Total		951.3	71			

+ These were mixed model analyses. Therefore acquisition and interaction effects were tested against error, and the filter effects were tested against interaction.

Bartlett's test for equality of variance; this indicated that there were no significant differences between 'within pairs' variances ($p > 0.8$).

The analysis of variance showed that noise in oblique slices from filter 8 was significantly greater than that in slices from the other filters tested. Also, there was a significant interaction between filters and acquisitions when data from filters 8 and VSMO were included in the analysis.

Friedman's two way analysis of variance of lesion detectability gave the following ordering of filters with the poorest performing filter at left:-

{3 1 8 VSMO} {5 1S 2 SMTH}.

Filters within brackets {} did not differ significantly from each other, while between filters in different bracketed sets there were significant differences ($p > 0.05$).

8.4.2 Experiment 2

In this experiment the best filters from experiment 1 were assessed (ie. filters 5, 1S, 2 and SMTH). Filter 1 was also selected as a comparison of a sharp filter with the four soft filters. It was chosen in preference to filter 3 because the axial images were already computed in order to derive the filter 1S images. The elimination of filters 8 and VSMO removed the interaction effect detected in experiment 1 with the peak noise data.

In order to increase the statistical power of the test used in this experiment, lesion detectability was assessed as the peak deviation (%) of the smallest lesion seen in every deviation image derived from the oblique slices. The smallest lesion observed in all slices was 15 mm in diameter. Table 8.5 gives the peak deviation of the 15 mm lesion in the 6 pairs of acquisitions for each of the filters. Also shown is the two way analysis of variance table (without interaction) from these data.

Table 8.5 Slice phantom, experiment 2

a) Peak deviation in 15 mm lesion (%)

	Concentration, 'Tissue background' : 'Myocardium'												
	0.5 : 1				1.0 : 1				2.0 : 1				
Acquisition:	1		2		3		4		5		6		
Filter	a	b	a	b	a	b	a	b	a	b	a	b	mean
1	23	25	27	29	16	20	20	16	17	12	23	33	21.75
1S	35	42	38	40	22	21	27	21	17	15	20	24	26.83
2	29	33	23	39	19	27	27	16	16	14	22	22	23.92
5	26	33	25	39	19	27	25	18	14	15	22	21	23.67
SMTH	36	42	38	43	24	21	31	16	16	14	21	22	27.00
pooled mean	33.25				21.65				19.00				

b) Analysis of variance table

Source	SS	df	MS	F	p
Filters	242.4	4	60.6	3.8	0.01
Acquisitions	3091.9	11	281.1	17.7	<.001
Error	697.6	44	15.9		
Total	4031.9	59			

Lesion detectability increased significantly ($p < 0.05$) with each decrease in concentration in the chamber simulating liver/lung uptake. The rank order of the filters (poorest at left) with non-significant sets bracketed (least significant difference = 3.28, p=0.05) was:-

{1} {5 2 1S} {2 1S SMTH}.

The difference between the mean deviation for filters 2 and 1S was 2.91, corresponding to p=0.075.

8.5 Discussion

The two pre-reconstruction filters examined with the slice phantom were not applied to the data from the rod phantom, since the alignment of the rods axially within the phantom rendered two-dimensional filtering of the projection data superfluous. The superiority in rod detection of filter 1S, which gave axial and transaxial smoothing, supported this.

An almost exact reversal of filter ranking (ignoring filter 8) was seen in the rod phantom experiment when data from slices not corrected for attenuation effects were compared with data from corrected slices (table 8.2). This was ascribed to increasing noise power towards the centre of corrected slices (Todd-Pokropek and Jarritt, 1982), which therefore require more noise suppression compared with uncorrected slices. Hence, there was a relative gain in resolution when the sharper filters were applied to data uncorrected for attenuation, compared with corrected data, which required softer filters to compensate for increased noise power. It was apparent that count density decreased towards the centre of reconstructed slices through the phantom when no attenuation correction was applied (figure P8.3).

When performing SPECT of the thorax the attenuation coefficient along each projection ray is not constant, because of the differing

attenuation characteristics of lung, blood, other soft tissues and bone. For this reason no attenuation correction of tomograms has been reported for imaging myocardial perfusion with thallium-201 (Larsson, 1980; Maublant et al,1982; Tamaki et al, 1982, Ziada et al, 1986 and Stirner et al, 1986) or technetium labelled agents (Holman et al, 1984; Stirner et al, 1988). In studies of myocardial perfusion with $^{99}Tc^{m}$-tBIN reported in Chapter 7, lower count densities centrally in reconstructed slices were not seen.

Myocardial tomography phantom studies with thallium-201, comparing data with and without attenuation compensation, have shown improved axial slice uniformity and less distortion when attenuation correction was applied (Coleman et al, 1982), and no effect on image contrast (Myers et al, 1983). For these reasons, it was decided that the rod phantom studies that best simulated clinical conditions were those in which attenuation compensation was applied. Therefore, attenuation corrections were applied to all the slice phantom studies.

Deviation images from the rod phantom data were computed using means and standard deviations calculated in a small ROI representing the myocardial activity. Inspection of deviation images computed using the mean and standard deviation of counts in the ROI enclosing the phantom showed no differences in distribution (figure P8.8). The inclusion of the rods resulted in smaller deviation image values because the standard deviation was numerically larger. Since the intention of the experiments was to compare filter performance, rather than to assess the size of lesion which might be observable in patient studies, deviation images from the slice phantom were produced from a single ROI. This decision contributed to the poorer overall lesion detectability in the slice phantom compared with the rod phantom (tables 8.1 and 8.3a). However, it is likely that the higher scatter contribution to the counts in the short cylinders of the slice phantom and artefacts introduced by

the interpolation necessary to produce oblique images from axial slices were more significant causes of reduced detectability of the lesions in this phantom compared with rods of the same diameters.

The probabilities quoted in table 8.4b,c underestimate the true probabilities since filters 8 and VSMO were excluded from the analysis by a posteriori data inspection (Sokal and Rohlf, 1981). However, the conclusions from the analyses are unaffected since the filter and interaction terms are non-significant and the acquisition term was computed solely to estimate variance due to the acquisition process.

Filters 8 and VSMO performed relatively poorly when assessed by lesion detectability. In the slice phantom, filter 8 also gave significantly more noisy reconstructions than the other filters and VSMO was noisier than the remainder. These filters also gave rise to a significant interaction effect in the analysis of variance of the peak noise in the slice phantom. This can be explained, in the case of filter 8, by examination of the spatial frequency representation of the filter function (figure 2.10). Although this filter enhances low spatial frequencies (signal), high frequencies (noise) are not suppressed. Axial slices reconstructed after pre-filtering of projections with the variable smooth appeared similar to those produced by filter 8. Therefore, it may be presumed that the frequency responses of the two filters were similar. However noise was suppressed somewhat better by VSMO, since data from adjacent projections were used in computation of the filtered projection value, whereas filter 8 is convolved only with one dimensional projections.

In the experiment performed using VSMO the reconstructions were nearly uniform but in the myocardial perfusion studies this was not true. Figure P8.9 shows the effect of VSMO and SMTH on data from one of the patients studied in Chapter 7. The smoothed planar images are very similar in appearance. However, radial artefacts can be seen in the

transaxial slices reconstructed after pre-filtering with VSMO. These are caused by propagation of unsmoothed high count projection pixels through the axial slices. The radial artefacts were not seen in the axial slices through the phantom in Experiment 1, because of the overall uniformity, but would be expected to add more noise in those slices through the phantom formed following application of VSMO.

King and colleagues (1987) have suggested that a non-stationary Metz filter may be useful for most SPECT procedures, with the filter varying to suit local count variations in the projections. However, the foregoing suggests that any filter which differs in its convolution kernel between projection pixels could lead to poor lesion detectability, by generation of radial artefacts in axial slices. Use of a single Metz filter for each set of projection images, but tailoring the filter to suit the total counts (King et al, 1984; King et al, 1987), seems to be more appropriate. Since the Metz filter is an enhancement filter, like filter 8, the success obtained with this filter is presumably due, in part, to the fact that the convolution kernel is applied in two dimensions to the projection data, giving better noise suppression.

The experimental results in the present study clearly indicate that the softer filters, giving more smoothing, gave the best differentiation of lesions from the surrounding activity distributions. This was true whether the filtering was applied before, during or after the reconstruction. Similar results were obtained from the analysis of patient studies with $^{99}Tc^{m}$-tBIN described in Chapter 7.

Many workers have chosen to reconstruct myocardial perfusion tomography images using one dimensional filtration of the projections, most commonly using the Hann weighted ramp, i.e. filter 5 (Tamaki et al, 1982; Holman et al, 1984; Ziada et al, 1986). Other, similar, one dimensional filters have been used; the soft Shepp-Logan, filter 2

(Larsson, 1980) and the Hamming filter (Stirner et al, 1988). A disadvantage of one dimensional projection filtration is the generation of line artefacts in coronal and sagittal images, which can be avoided with other filtration techniques. An improvement in axial slice image quality has been reported from the use of a two dimensional rather than a one dimensional implementation of the Metz filter (King et al, 1987). Other filters which have been used with success include a two dimensional approximation of the Butterworth filter, applied to the projection images, prior to reconstruction with the ramp (Cerqueira et al, 1987) and ramp reconstruction followed by a three dimensional count dependent smooth (Maublant et al,1982).

In myocardial phantom studies using thallium-201, Eisner and colleagues (1986) used the Hanning filter (filter 5) after 1-2-1 smoothing of the projection images in the axial direction only. Reconstructing with a pure ramp (filter 3) and with the sharp Shepp-Logan (filter 1), Laird and Williams (1987) have compared no filtration, pre-filtration of projections with a two dimensional Metz filter tailored to the total counts and post filtration of axial slices with a two dimensional 1-2-1 weighted smooth. They found the best technique to be ramp reconstruction following Metz filtration and that the sharp Shepp-Logan filter, followed by a smooth, was the best compromise of processing speed and reconstruction quality in the absence of an array processor for the Metz pre-filtration.

Thus, the reconstruction filters selected by other workers for clinical myocardial tomography and phantom simulations have, in general, been smoothing filters similar to filters 5, 2, 1S and SMTH, both in spatial frequency represention (Chapter 2) and in the visual appearances of the processed images. However, neither the details of the acquisition procedure, nor the image viewing and reporting conditions, were standardised between the studies referred to above. Furthermore, King

and colleagues (1987) have reported that visual assessment of optimum image quality with varying filtration differs between observers.

In conclusion, therefore, there is no single 'best' reconstruction filter for myocardial perfusion tomography. Filter choice should be made by phantom studies which simulate the imaging conditions as closely as possible and by visual assessment of clinical images reconstructed with the soft filters discussed above, with the final selection of filter based on agreement with clinical diagnoses.

9. Conclusions

The experiments performed in the studies described in this thesis have investigated three aspects of nuclear medicine image processing. These are curve processing (hepatic perfusion imaging), feature extraction (left ventricular edge detection) and lesion detectability (myocardial perfusion tomography).

Hepatic perfusion imaging (Chapter 4) is of particular clinical importance because of the inability of other imaging modalities to identify those patients with hepatic micro-metastases. Early identification of these patients allows treatment with cytotoxic drugs in good time and is likely to lead to an improved survival rate among patients undergoing primary resection of carcinoma. The lack of agreement between the work presented here and that of the Leeds group (Cooke et al, 1987) indicates that more work is required to relate the blood flow analyses to diagnostic criteria. This result is an unfortunate but common finding in many areas of medical diagnosis and is mainly due to local differences in referral patterns and diagnostic criteria adopted.

The edge detection algorithm described in this thesis was developed in order to overcome a shortcoming in the computer software package supplied by Nodecrest. It has allowed the development of a reproducible, fully automatic method for determination of the left ventricular ejection fraction. The algorithm has subsequently been used successfully to identify the outline of the gall bladder in hepatobiliary imaging for the estimation of gall bladder ejection fraction (Reynolds et al, 1986).

The diagnosis of myocardial perfusion deficits by means of nuclear medicine techniques is likely to rapidly change in the near future. Studies performed using thallium-201 are likely to be replaced by those using $^{99}Tc^{m}$-labelled isonitrile complexes. The use of emission

tomography for thallium-201 imaging is widely accepted as superior to planar imaging but it was necessary to establish optimum imaging protocols for the new, technetium-99m-labelled agents. Since technetium-99m has different physical properties to those of thallium-201 an investigation of the choice of reconstruction filter was also necessary.

As newer imaging modalities (e.g. X-ray CT, magnetic resonance imaging) are able to provide ever more accurate anatomical information, the role of nuclear medicine moves more towards its origins in a description of the functional (physiological) significance of disease. Examples of this trend are the development of agents demonstrating regional cerebral blood flow for use with SPECT systems and the increase in the use of hepatobiliary agents and the interest in hepatic blood flow studies. As new radiopharmaceuticals are developed and used to elucidate the pathophysiology of disease, image processing techniques, particularly for accurate quantitation of image data, will also need to be established to fully realise the diagnostic potential of these agents.

Ackerman NB, Lien WM, Kondi ES and Silverman NA, 1969. The blood supply of experimental liver metastases. I. The distribution of hepatic artery and portal vein blood to "small" and "large" tumours. Surgery 66: 1067-1072.

Alderson PO, Jost RG, Strauss AW, Boonvisut S and Markham J, 1975. Radionuclide angiocardiography: improved diagnosis and quantitation of left-to-right shunts using area ratio techniques in children. Circulation 51: 1136-1143.

Alderson PO, Douglass KH, Mendenhall KG, Guadiani VA, Watson DC, Links JM and Wagner HN, 1979. Deconvolution analysis in radionuclide quantitation of left to right cardiac shunts. Journal of Nuclear Medicine 20: 502-506.

Anderson PAW, Jones RH and Sabiston DC, 1974. Quantitation of left-to-right cardiac shunts with radionuclide angiography. Circulation 49: 512-516.

Anger HO, 1958. The scintillation camera. Review of Scientific Instruments 29: 27-33.

Ansell G and Rotblat J, 1948. Radioactive iodine as a diagnostic aid for intrathoracic goitre. British Journal of Radiology 21: 552-558.

Ashburn WL, Schelbert HR and Verba JW, 1978. Left ventricular ejection fraction - a review of several angiographic approaches using the scintillation camera. Progress in Cardiovascular Diseases 20: 267-284.

Askenazi J, Ahnberg DS, Korngold E, LaFarge CG, Maltz DL and Treves S, 1976. Quantitative radionuclide angiocardiography: detection and quantitation of left to right shunts. American Journal of Cardiology 37: 382-387.

Axelsson B, Msaki P and Israelsson A, 1984. Subtraction of Compton-scattered photon emission computed tomography. Journal of Nuclear Medicine 25: 490-494.

Barber DC and Tindale WB, 1989. A new method of determining portal flow fraction in normal and diseased livers (abst). Nuclear Medicine Communications 10: 249.

Baxter RH, Becker LC, Alderson PO, Rigo P, Wagner HN and Weisfeldt ML, 1980. Quantification of aortic valvular regurgitation in dogs by nuclear imaging. Circulation 61: 404-410.

Bellini S, Piacentini M, Cafforio C and Rocca F, 1979. Compensation of tissue absorption in emission tomography. IEEE Transactions in Acoustics, Speecch and Signal Processing ASSP-27: 213-218.

Berger HJ, Matthay RA, Loke J, Marshall RC, Gottschalk A and Zaret BL, 1978. Assessment of cardiac performance with quantitative radionuclide angiocardiography: right ventricular ejection fraction with reference to findings in chronic obstructive pulmonary disease. American Journal of Cardiology 41: 897-905.

Berger BC, Watson DD, Taylor GJ, Craddock GB, Martin RP,Teates CD and Beller GA, 1981. Quantitative thallium-201 exercise scintigraphy for detection of coronary artery disease. Journal of Nuclear Medicine 22: 585-593.

Bianco JA and Shafer RB, 1979. Radionuclide methods in the assessment of left ventricular function. American Journal of the Medical Sciences 277: 244-254.

Bonte FJ, Graham KD and Moore JG, 1973. Experimental myocardial imaging with ^{131}I-labeled oleic acid. Radiology 108: 195-196.

Bonte FJ, Parkey RW, Graham KD, Moore J and Stokely EM, 1974. A new method for radionuclide imaging of myocardial infarcts. Radiology 110: 473-474.

Bradley SE, Ingelfinger FJ and Bradley GP, 1952. Hepatic circulation in cirrhosis of the liver. Circulation 5: 419-429.

Borer JS, Bacharach SL, Green MV, Kent KM, Henry WL, Rosing DR, Seides SF, Johnston GS and Epstein SE, 1978. Exercise-induced left ventricular dysfunction in symptomatic and asymptomatic patients with aortic regurgitation: assessment with radionuclide cineangiography. American Journal of Cardiology 42: 351-357.

Breedis C and Young G, 1954. The blood supply of neoplasms in the liver. American Journal of Pathology 30: 969-986.

Brooks RA and DiChiro G, 1976. Principles of computer assisted tomography (CAT) in radiographic and radioisotopic imaging. Physics in Medicine and Biology 21: 689-732.

Brown DW, Kirch DL, Trow RS, LeFree M and Steele PP, 1973. Quantification of the radionuclide image. Seminars in Nuclear Medicine 3: 311-325.

Burke G, Halko A and Goldberg D, 1968. Radiopulmonary cardiography with the scintillation camera and ^{99m}Tc-pertechnetate (abst). Journal of Nuclear Medicine 9: 306-307.

Burke G, Halko A and Goldberg D, 1969. Dynamic clinical studies with radioisotopes and the scintillation camera: IV. ^{99m}Tc-sodium pertechnetate cardiac blood flow studies. Journal of Nuclear Medicine 10: 270-280.

Burow RD, Strauss HW, Singleton R, Pond M, Rehn T, Bailey IK, Griffith LC, Nickoloff E and Pitt B, 1977. Analysis of left ventricular function from multiple gated acquisition cardiac blood pool imaging. Comparison to contrast angiography. Circulation 56: 1024-1028.

Burow RD, Wilson MF, Heath PW, Corn CR, Amil A and Thadani U, 1982. Influence of attenuation on radionuclide stroke volume determinations. Journal of Nuclear Medicine 23: 781-785.

Campbell S, Holman BL, Kirshenbaum JM, Antman EM, Lister-James J, Davison A, Kozlowski J, English RJ and Jones AG, 1986. The scintigraphic evaluation of myocardial infarction and regional ventricular peformance using technetium-99m hexakis (t-butyl isonitrile) technetium (I) (TBI): A new myocardial imaging agent. European Journal of Nuclear Medicine 12: 219-225.

Carter BL, Johnsen SE, Loeffler RK and Southard ME, 1959. A critical evaluation of external body surface counting in the determination of cardiac output with radioisotopes. American Journal of Roetgenology, Radium Therapy and Nuclear Medicine 82: 618-625.

Cassen B, Curtis L, Reed C and Libby R, 1951. Instrumentation for ^{131}I use in medical studies. Nucleonics 9: 46.

Cerqueira MD, Harp GD and Ritchie JL, 1987. Evaluation of myocardial perfusion and function by single photon emission computed tomography. Seminars in Nuclear Medicine 17: 200-213.

Chaitman BR, DeMots H, Bristow JD, Rosch J and Rahimtoda SH, 1975. Objective and subjective analysis of left ventricular angiograms. Circulation 52: 420-425.

Chang LT, 1978. A method for attenuation correction in radionuclide computed tomography. IEEE Transactions in Nuclear Science NS-25: 638-643.

Chang W, Henkin RE, Hale DJ and Hall D, 1980a. Methods for detection of left ventricular edges. Seminars in Nuclear Medicine 10: 39-53.

Chang W, Lin SL, Henkin RE and Salo BC, 1980b. A multisegmental slant hole tomographic collimator (MUST): a new tomographic gamma camera system (abst). Journal of Nuclear Medicine 21: P28.

Chervu LR, 1979. Radiopharmaceuticals in cardiovascular nuclear medicine. Seminars in Nuclear Medicine, 9: 241-256.

Chesler DA and Riederer SJ, 1975. Ripple suppression during reconstruction in transverse tomography. Physics in Medicine and Biology 20: 632.

Cohen J, 1960. A coefficient of agreement for nominal scales. Educational and Psychological Measurement 20: 37-46.

Coleman RE, Jaszczak RJ and Cobb FR, 1982. Comparison of 180^{o} and 360^{o} data collection in thallium-201 imaging using single-photon emission computed tomography (SPECT). Journal of Nuclear Medicine 23: 655-660.

Cooke DA, Parkin A, Wiggins P, Robinson PJ and Giles GR, 1987. Hepatic perfusion index and the evolution of liver metastases. Nuclear Medicine Communications 8: 970-972.

Corfield JR, 1975. Development of a fast image enhancement filter for routine use. Int. Jahrestagung der Gesellschaft fur Nuclear Medicine, 13, Copenhagen.

Davis LS, 1975. A survey of edge detection techniques. Computer Graphics and Image Processing 4: 248-270.

DeNardo GL, Stadalnik RC, DeNardo SJ and Raventos A, 1974. Hepatic scintiangiographic patterns. Radiology 111: 135-141.

DeNardo S, Bell GB, DeNardo GL, Carreta RF, Scheibe PO, Imperato TJ and Jackson PE, 1976. Diagnosis of cirrhosis and hepatitis by quantitative hepatic and other reticuloendothelial clearance rates. Journal of Nuclear Medicine 17: 449-459.

Dobson EL, Warner GF, Finney CR and Johnston ME, 1953. The measurement of liver circulation by means of colloid disappearance rate. I. Liver blood flow in normal young men. Circulation 7: 690-695.

Drum DE, 1982. Current status of radiocolloid hepatic scintiphotography for space-occupying disease. Seminars in Nuclear Medicine 12: 64-74.

Dymond DS, Jarritt PH, Britton KE and Spurrell RAJ, 1979. Detection of postinfarction left ventricular aneurysms by first pass radionuclide ventriculography using a multicrystal gamma camera. British Heart Journal 41: 68-78.

Dymond DS, Elliott AT, Flatman W, Britton KE, Spurrell RAJ, Bett R, Cuninghame JG, Sims HE and Willis HH, 1982a. Gold-195m: a new short half life radionuclide for first pass cardiac studies in adults (abst). Nuclear Medicine Communications 3: 120.

Dymond DS, Halama J and Schmidt DH, 1982b. Right anterior oblique first pass radionuclide ejection fractions: effects of temporal smoothing and various background corrections. Journal of Nuclear Medicine 23: 1-7.

Eisner RL, Nowak DJ, Pettigrew R and Fajman W, 1986. Fundamentals of 180^{o} acquisition and reconstruction in SPECT imaging. Journal of Nuclear Medicine 27: 1717-1728.

Elliott AT and Short MD, 1981. Image forming systems. In Physical Aspects of Medical Imaging (eds. Moore BM, Parker RP and Pullan BR) pp169-183. John Wiley & Sons, Chichester.

Elliott AT, Dymond DS, Stone DL, Flatman W, Bett R, Cuninghame JG, Sims HE and Willis HH, 1983. A $^{195}Hg^{m}$-$^{195}Au^{m}$ generator for use in first pass nuclear angiocardiography. Physics in Medicine and Biology 28:139-147.

Evans AL, 1981. The Evaluation of Medical Images. Adam Hilger Ltd., Bristol.

Finlay IG and McArdle CS, 1986. Occult hepatic metastases in colorectal carcinoma. British Journal of Surgery 73: 732-735.

Finlay IG, Meek DR and Gray HW, 1982. Incidence and detection of occult hepatic metastases in colorectal carcinoma. British Medical Journal 284:803-805.

Flaherty JT, Canent RV, Bineau JP, Anderson PAW, Levin AR and Spach MS, 1967. Use of externally recorded radioisotope-dilution curves for quantitation of left to right shunts. American Journal of Cardiology 20: 341-345.

Fleming JS, Humphries NLM, Karran SJ, Goddard BA and Ackery DM, 1981a. In vivo assessment of hepatic arterial and portal venous components of liver perfusion. Journal of Nuclear Medicine 22: 18-21.

Fleming JS, Humphries NLM, Karran SJ, Ackery DM, Goddard BA and Gallagher PJ, 1981b. The effect of progression of cirrhosis on radiocolloid dynamics in rats (abst). Nuclear Medicine Communications 2: 99.

Fleming JS, Ackery DM, Walmsley BH and Karran SJ, 1983. Scintigraphic estimation of arterial and portal blood supplies to the liver. Journal of Nuclear Medicine 24: 1108-1113.

Floyd CE, Jaszczak RJ, Greer KL and Coleman RE, 1985. Deconvolution of Compton scatter in SPECT. Journal of Nuclear Medicine 26: 403-408.

Folse R and Braunwald E, 1962. Pulmonary vascular dilution curves recorded by external detection in the diagnosis of left-to-right shunts. British Heart Journal 24: 166-172.

Gandsman EJ, North DL, Shulman RS and Bough EW, 1981. Measurement of the ventricular stroke volume ratio by gated radionculide angiography. Radiology 138: 161-165.

Gates GF, Orme HW and Dore EK, 1971. Measurement of cardiac shunting with technetium-labelled albumin aggregates. Journal of Nuclear Medicine 12: 746-749.

Gerundini P, Savi A, Gilardi MC, Margonato A, Vicedomini G, Zecca L, Hirth W, Libson K, Bhatia JC, Fazio F and Deutsch E, 1986. Evaluation in dogs and humans of three potential technetium-99m myocardial perfusion agents. Journal of Nuclear Medicine 27: 409-416.

Glick G, Schreiner BF, Luria MN and Yu PN, 1962. Determination of cardiac output by means of radioisotope dilution technic. Progress in Cardiovascular Diseases 4: 586-614.

Gliedman ML and Wilk PJ, 1982. A surgeon's view of hepatobiliary scintigraphy. Seminars in Nuclear Medicine 12: 2-4.

Goris ML, Daspit SG, McLaughlin P and Kriss JP, 1976. Interpolative background subtraction. Journal of Nuclear Medicine 17: 744-747.

Goris ML, McKillop JH and Briandet PA, 1981. A fully automated determination of the left ventricular region of interest in nuclear angiocardiography. Cardiovascular and Interventional Radiology 4: 117-123.

Goris ML and Briandet PA, 1983. A Clinical and Mathematical Introduction to Computer Processing of Scintigraphic Images. Raven Press, New York.

Gullberg GT, 1983. True three-dimensional reconstruction in single photon emission computed tomography (abst). Journal of Nuclear Medicine 24: P81.

Ham MR, Dobbeleir A, Viart P, Piepsz A and Lenaers A, 1981. Radionuclide quantitation of left-to-right shunts using deconvolution analysis. Journal of Nuclear Medicine 22: 688-692.

Hains ADB, Al-Khawaja I, Lahiri A and Raftery EB, 1986. Variations in methods for calculating ejection fraction: a note of caution (abst). Nuclear Medicine Communications 7: 270.

Hardy JG and Wilson CG, 1981. Radionuclide imaging in pharmaceutical, physiological and pharmacological research. Clinical Physics and Physiological Measurement 2: 71-121.

Harolds JA, Grove RD, Bowen RD and Powers TA, 1981. Right-ventricular function as assessed by two radionuclide techniques. Journal of Nuclear Medicine 22: 113-115.

Harpen MD, Duboisson RL, Head GB, Parmley LF, Jones TB and Robinson AE, 1983. Determination of left ventricular volume from first pass kinetics of labeled red cells. Journal of Nuclear Medicine 24: 98-103.

Harris JM, 1984. Coronary angiography and its complications. Archives of Internal Medicine 144: 337-341.

Hawkins T and Keavey PM, 1984. Gated cardiac imaging: manual calculations and observations of left ventricular ejection fraction. Physics in Medicine and Biology 29: 261-265.

Holman BL, Tanaka TT and Lesch M, 1976. Evaluation of radiopharmaceuticals for the detection of acute myocardial infarction in man. Radiology 121: 427-430.

Holman BL, 1979. Cardiac imaging in nuclear medicine. Radiology 133: 709-716.

Holman BL, Neirinckx RD, Treves S and Tow DE, 1979. Cardiac imaging with tantalum-178. Radiology 131: 525-526.

Holman BL, Kirsch C-M and Zielonka JS, 1982. The heart. In Computed Emission Tomography (eds. Ell PJ and Holman BL) pp475-494. Oxford University Press, Oxford.

Holman BL, Jones AG, Lister-James J, Davison A, Abrams MJ, Kirshenbaum JM, Tumeh SS and English RJ, 1984. A new Tc-99m labeled myocardial imaging agent, hexakis (t-butylisonitrile)-technetium (I) [Tc-99m TBI]: initial experience in the human. Journal of Nuclear Medicine 25: 1350-1355.

Holman BL, Campbell CA, Lister-James J, Jones AG, Davison A and Kloner RA, 1986. Effect of reperfusion and hyperemia on the myocardial distribution of technetium-99m t-butylisonitrile. Journal of Nuclear Medicine 27: 1172-1177.

Holman BL, Sporn V, Jones AG, Sia STB, Perez-Balino N, Davison A, Lister-James J, Kronauge JF, Mitta AEA, Camin LL, Campbell S, Williams SJ and Carpenter AT, 1987. Myocardial imaging with technetium-99m CPI: initial experience in the human. Journal of Nuclear Medicine 28: 13-18.

Houston AS, 1981. Signal Processing. In Physical Aspects of Medical Imaging (eds. Moore BM, Parker RP and Pullan BR) pp203-216. John Wiley and Sons, Chichester.

HPA, 1978. The Theory, Specification and Testing of Anger Type Gamma Cameras: Topic Group Report 27. The Hospital Physicists' Association, London.

Huff RL, Parrish D and Crockett W, 1957. A study of circulatory dynamics by means of crystal radiation detectors on the anterior thoracic wall. Circulation Research 5: 395-400.

Izzo G, DiLuzio S, Guerrisi M, Favella A and Magrini A, 1983. On the interpretation of the early part of the liver time-activity curve: double tracer experiment. European Journal of Nuclear Medicine 8: 101-104.

Jaszczak RJ, Coleman RE and Whitehead FR, 1981. Physical factors affecting quantitative measurements using camera-based single photon emission computed tomography (SPECT). IEEE Transactions in Nuclear Science NS-28: 69-80.

Jaszczak RJ, Greer KL, Floyd CE, Harris CC and Coleman RE, 1984. Improved SPECT quantitation using compensation for scattered photons. Journal of Nuclear Medicine 25: 893-900.

Jengo JA, Mena I, Blaufuss A and Criley JM, 1978. Evaluation of left ventricular function (ejection fraction and segmental wall motion) by single pass radioisotope angiography. Circulation 57: 326-332.

Kalff V, Rabinovitch MA, Chan W, O'Neill W, Stewart J, Walton J, Pitt B and Thrall JH, 1982. Baseline left-ventricular function during frequent ventricular or atrial ectopic beats. Journal of Nuclear Medicine 23: 1076-1079.

Kenny RW, Ackery DM, Fleming HS, Goddard BA and Grant RW, 1975. Deconvolution analysis of the scintillation camera renogram. British Journal of Radiology 48: 481-486.

Keyes JW, 1982. Instrumentation. In Computed Emission Tomography (eds. Ell PJ and Holman BL) pp243-262. Oxford University Press, Oxford.

Khalil MN, Patel KM, Early MY, Hartley G, Thornback J and Berry JM, 1985a. The use of ^{99m}Tc tertiary butyl isonitrile (BIN) as a myocardial imaging agent in man (abst). European Journal of Nuclear Medicine 11: A22

Khalil MN, Thornback J, Early MY, Morton DB, Berry JM and Hubner PJB, 1985b. Technetium-99m isonitrile complex as a potential myocardial imaging agent. Nuclear Medicine Communications 6: 615-622.

Khaw BA, Beller GA, Haber E and Smith TW, 1976. Localisation of cardiac myosin-specific antibody in myocardial infarction. Journal of Clinical Investigation 58: 439-446.

Khaw BA, Yasuda T, Gold HK, Leinbach RC, Johns JA, Kanke M, Barlai-Kovach M, Strauss HW and Haber E, 1987. Acute myocardial infarct imaging with indium-111-labelled monoclonal antimyosin F_{ab}. Journal of Nuclear Medicine 28: 1671-1678.

King MA, Schwinger RB, Doherty PW and Penney BC, 1984. Two-dimensional filtering of SPECT images using Metz and Wiener filters. Journal of Nuclear Medicine 25: 1234-1240.

King MA, Schwinger RB, Penney BC, Doherty PW and Bianco JA, 1986. Digital restoration of indium-111 and iodine-123 SPECT images with optimized Metz filters. Journal of Nuclear Medicine 27: 1326-1336.

King MA, Glick SJ, Penney BC, Schwinger RB and Doherty PW, 1987. Interactive visual optimization of SPECT prereconstruction filtering. Journal of Nuclear Medicine 28: 1192-1198.

King MA, Miller TR, Doherty PW and Schwinger RB, 1988. Stationary and nonstationary spatial domain Metz filtering. Nuclear Medicine Communications 9: 3-10.

Kirch DL, Metz CE and Steele PP, 1974. Quantitation of valvular insufficiency by computerized radionuclide angiocardiography. American Journal of Cardiology 34: 711-721.

Kriss JP, Enright LP, Hayden WG, Wexler L and Shumway NE, 1971. Radioisotopic angiocardiography: wide scope of applicability in diagnosis and evaluation of therapy in diseases of the heart and great vessels. Circulation 43: 792-808.

Kuruc A, Treves S and Parker JA, 1983. Accuracy of deconvolution algorithms assessed by simulation studies. Journal of Nuclear Medicine 24: 258-263.

Laird EE and Williams ED, 1987. The optimum technique for ^{201}Tl tomography of myocardium: an investigation using phantoms. Physics in Medicine and Biology 32: 985-999.

Lam W, Pavel D, Byrom E, Sheikh A, Best D and Rosen K, 1981. Radionuclide regurgitant index; value and limitations. American Journal of Cardiology 47: 292-298.

Larsson SA, 1980. Gamma camera emission tomography. Acta Radiologica, Supplementum 363: 1-75.

Leveson SH, Wiggins PA, Giles GR, Parkin A and Robinson PJ, 1985. Deranged liver blood flow patterns in the detection of liver metastases. British Journal of Surgery 72: 128-130.

Lewis SE, Buja LM, Dehmer GJ, Bonte FJ, Parkey RW and Willerson JT, 1979. Nuclear Cardiology - 1980. Upjohn, Kalamazoo.

Lis GA and Zu'bi SM, 1982. Removal of bolus fragmentation artifacts from pulmonary curves as applied to Q_p/Q_s shunt determination. Journal of Nuclear Medicine 23: 930-933.

Liu XJ, Shi RF, Wang YQ, Guo XZ, He ZX, Wang XB and Liu BL, 1987. Clinical evaluation of the ^{99m}Tc-labeled myocardial imaging agent, hexakis (t-butylisonitrile)-technetium. European Journal of Nuclear Medicine 13: 171-173.

Lumia FJ, Patil A, Germon PA and Mavanhao V, 1981. Tricuspid regurgitation by radionuclide angiography and contrast right ventriculography: a preliminary observation. Journal of Nuclear Medicine 22: 804-809.

MacIntyre WJ, Storaasli JP, Krieger H, Pritchard W and Friedell H, 1952. I^{131}-labeled serum albumin: its use in the study of cardiac output and peripheral vascular flow. Radiology 59: 849-857.

MacIntyre WJ, Pritchard WH and Moir TW, 1958. The determinatin of cardiac output by the dilution method without arterial sampling: I. Analytical concepts. Circulation 18: 1139-1146.

Maddahi J, Berman D, Matsuoka D, Charuzi Y, Gray R, Pantaleo N, Swan HJC, Forrester J and Waxman A, 1979. Right ventricular ejection fraction at rest and during exercise in normals and in coronary artery disease patients: assessment by multiple gated equilibrium scintigraphy (abst). Journal of Nuclear Medicine 20: 625.

Makler PT, McCarthy DM, Velchik MG, Goldstein HA and Alavi A, 1983. Fourier amplitude ratio: a new way to assess valvular regurgitation. Journal of Nuclear Medicine 24: 204-207.

Maltz DL and Treves S, 1973. Quantitative radionuclide angiocardiography: determination of Q_p:Q_s in children. Circulation 47: 1049-1056.

Marshall RC, Berger HJ, Costin JC, Freedman GS, Wolberg J, Cohen LS, Gottschalk A and Zaret BL, 1977. Assessment of cardiac performance with quantitative radionuclide angiocardiography: sequential left ventricular ejection fraction, normalized left ventricular ejection rate, and regional wall motion. Circulation 56: 820-829.

Martin W, Tweddel AC, McGhie AI and Hutton I, 1987. Gated thallium scintigraphy in patients with coronary artery disease: an improved planar imaging technique. Clinical Physics and Physiological Measurement 8: 343-354.

Mason DT, Ashburn WL, Harbert JC, Cohen LS and Braunwald E, 1969. Rapid sequential visualization of the heart and great vessels in man using the wide-field Anger scintillation camera. Circulation 39: 19-28.

Matin P and Kriss JP, 1970. Radioisotopic angiocardiography: findings in mitral stenosis and mitral insufficiency. Journal of Nuclear Medicine 11: 723-730.

Maublant J, Cassagnes J, Le Jeune JJ, Mestas D, Veyre A, Jallut H and Meyniel G, 1982. A comparison between conventional scintigraphy and emission tomography with thallium-201 in the detection of myocardial infarction. Journal of Nuclear Medicine 23: 204-208.

McIndoe AH, 1928. Vascular lesions of portal cirrhosis. Archives of Pathology 5: 23-42.

Melin JA, Wijns W, Robert A, Nannan M, De Coster P, Beckers C and Detry JM, 1985. Validation of radionuclide cardiac output measurements during exercise. Journal of Nuclear Medicine 26: 1386-1393.

Mena I and Fain J, 1981. Usefulness of phase analysis in nuclear medicine (abst). Nuclear Medicine Communications 2: 93.

Metz CE, 1970. On the differential method of image focussing. Journal of Nuclear Medicine 11: 142-143.

Minford JE, Hardy JG, Johnston DI and Wastie ML, 1984. The investigation of neonatal obstructive jaundice using 123I rose bengal. British Journal of Radiology 57: 213-216.

Mishkin FS and Mishkin ME, 1974. Documentation of tricuspid regurgitation by radionuclide angiocardiography. British Heart Journal 36: 1019-1022.

Moore SC, 1982. Attenuation compensation. In Computed Emission Tomography (eds. Ell PJ and Holman BL) pp339-360. Oxford University Press, Oxford.

Muellhener G, 1971. A tomographic scintillation camera. Physics in Medicine and Biology 16: 87-95.

Mukai T, Links JM, Douglass KH and Wagner HN, 1988. Scatter correction in SPECT using non-uniform attenuation data. Physics in Medicine and Biology 33: 1129-1140.

Mullins CB, Mason DT, Ashburn WL and Ross J, 1969. Determination of ventricular volume by radioisotope-angiography. American Journal of Cardiology 24: 72-78.

Myers MJ, Busemann Sokole E and de Bakker J, 1983. A comparison of rotating slant hole collimator and rotating camera for single photon emission tomography of the heart. Physics in Medicine and Biology 28: 581-588.

Neill GBS and Hutchinson F, 1971. Computer detection and display of focal lesions on scintiscans. British Journal of Radiology 44: 962-969.

Neirinckx RD, Jones AG, Davis MA, Harris GI and Holman BL, 1978. Tantalum-178 - a short lived nuclide for nuclear medicine: development of a potential generator system. Journal of Nuclear Medicine 19: 514-519.

Norusis MJ, 1985. SPSS-X Advanced Statistics Guide. McGraw-Hill, New York.

O'Brien AR and Gemmell HG, 1986. Effectiveness of oblique section display in thallium-201 myocardial tomography. Nuclear Medicine Communications 7: 609-616.

Okada RD, Kirschenbaum HD, Kushner FG, Strauss HW, Dinsmore RE, Newell JB, Boucher CA, Block PC and Pohost GM, 1980. Observer variance in the qualitative evaluation of left ventricular wall motion and the quantitation of left ventricular ejection fraction using rest and exercise multigated blood pool imaging. Circulation 61: 128-136.

Parker JA, Secker-Walker R, Hill R, Siegel BA and Potchen EJ, 1972. A new technique for the calculation of left ventricular ejection fraction. Journal of Nuclear Medicine 13: 649-651.

Parkey RW, Bonte FJ, Meyer SL, Atkins JM, Curry GL, Stokely EM and Willerson JT, 1974. A new method for radionuclide imaging of acute myocardial infarction in humans. Circulation 50: 540-546.

Parkin A, Robinson PJ, Baxter P, Leveson SH, Wiggins PA and Giles GR, 1983. Liver perfusion scintigraphy - method, normal range and laparotomy correlation in 100 patients. Nuclear Medicine Communications 4: 395-402.

Pavel DG, Zimmer AM and Patterson VN, 1977. In vivo labeling of red blood cells with 99mTc: A new approach to blood pool visualization. Journal of Nuclear Medicine 18: 305-308.

Perkins AC, Whalley DR, Ballantyne KC and Hardcastle JD, 1987. Reliability of the hepatic perfusion index for the detection of liver metastases. Nuclear Medicine Communications 8: 982-989.

Pfisterer ME, Battler A, Swanson SM, Slutsky R, Froelicher V and Ashburn WL, 1979. Reproducibility of ejection-fraction determinations by equilibrium radionuclide angiography in response to supine bicycle exercise: Concise communication. Journal of Nuclear Medicine 20: 491-495.

Phelps ME, Hoffman EJ, Selin C, Huang SC, Robinson G, MacDonald N, Schelbert H and Kuhl DE, 1978. Investigation of (^{18}F)2-fluoro-2 deoxyglucose for the measure of myocardial metabolism. Journal of Nuclear Medicine 19: 1311-1319.

Pizer SM and Todd-Pokropek AE, 1978. Improvement of scintigrams by computer processing. Seminars in Nuclear Medicine 8: 125-146.

Ramachandran GN and Lakshminarayanan AV, 1971. Three-dimensional reconstruction from radiographs and electron micrographs: application of convolutions instead of Fourier transforms. Proceedings of the Mational Academy of Science, USA 64: 2236-2240.

Reiber JHC, Lie SP, Simoons ML, Hoek C, Gerbrands JJ, Wijns W, Bakker WH and Kooij PPM, 1983. Clinical validation of fully automated computation of ejection fraction from gated equilibrium blood-pool scintigrams. Journal of Nuclear Medicine 24: 1099-1107.

Reynolds JR, Whalley D, Blamey RW and Doran J, 1986. Gallbladder function in patients with a positive cholecystokinin (CCK) provocation test (abst). Nuclear Medicine Communications 7: 279.

Rigo P, Alderson PO, Robertson RM, Becker LC and Wagner HN, 1979. Measurement of aortic and mitral valve regurgitation by gated cardiac blood pool scans. Circulation 60: 306-312.

Robinson GD and Lee AW, 1975. Radioiodinated fatty acids for heart imaging: iodine monochloride addition compared with iodide replacement labeling. Journal of Nuclear Medicine 16: 17-21.

Robinson PJ, Parkin A, Leveson SH, Wiggins PA, Nasiru TA and Giles GR, 1983. Perfusion scintigraphy improves the detection of liver metastases (abst). Nuclear Medicine Communiations 4: 139.

Rogers WJ, Smith LR, Hood WP, Mantle JA, Rackley CE and Russell RO,1979. Effect of filming projection and interobserver variation on angiographic biplane left ventricular volume determination. Circulation 59: 96-104.

Rothe CF, 1984. Cardiodynamics. In Physiology (ed Selkurt EE), pp261-277. Little, Brown and Company, Boston.

Sarper R, Fajman WA, Tarcan YA and Nixon DW, 1981a. Enhanced detection of metastatic liver disease by computerized flow scintigrams. Journal of Nuclear Medicine 22: 318-321.

Sarper R, Fajman WA, Rypins EB, Henderson JM, Tarcan YA, Galambos JT and Warren WD, 1981b. A non-invasive method for measuring total portal venous/total hepatic blood flow by hepatosplenic radionuclide angiography. Radiology 141: 179-184.

Sarper R and Tarcan YA, 1983. An improved method of estimating the portal venous fraction of total hepatic blood flow from computerized radionuclide angiography. Radiology 147: 559-562.

Schelbert HR, Verba JW, Johnson AD, Brock GW, Alazraki NP, Rose FJ and Ashburn WL, 1975. Non traumatic determination of left ventricular ejection fraction by radionuclide angiocardiography. Circulation 51: 902-909.

Schelbert HR, 1982. The heart. In Computed Emission Tomography (eds. Ell PJ and Holman BL) pp91-133. Oxford University Press, Oxford.

Schreiner BF, Lovejoy FW and Yu PN, 1959. Estimation of cardiac output from precordial dilution curves in patients with cardiopulmonary disease. Circulation Research 7: 595-601.

Shosa DW, O'Connell JW and Hattner RS, 1980. Motivation for the rotating slant hole approach to scintillation camera tomography. Journal of Nuclear Medicine 21: 27.

Sokal RR and Rohlf FJ, 1981. Biometry. WH Freeman and Company, New York.

Sorensen SG, O'Rourke RA and Chaudhuri TK, 1980. Noninvasive quantitation of valvular regurgitation by gated equilibrium radionuclide angiography. Circulation 62: 1089-1098.

Sorensen SG, Starling MR, Chaudhuri TK and O'Rourke RA, 1982. Noninvasive quantitation of right ventricular volume overload in adults by gated equilibrium radionuclide angiography. Journal of Nuclear Medicine 23: 957-964.

Spach MS, Canent RV, Boineau JP, White AW, Sanders AP and Baylin GJ, 1965. Radioisotope-dilution curves as an adjunct to cardiac catheterization. 1. left to right shunts. American Journal of Cardiology 16: 165-175.

SPSS Inc., 1986. SPSS-X Users Guide, 2nd. edition. McGraw-Hill, New York.

Stadalnik RC, DeNardo SJ, DeNardo GL and Raventos A, 1975. Critical evaluation of hepatic scintiangiography for neoplastic tumors of the liver. Journal of Nuclear Medicine 16: 595-601.

Starmer CF and Clark DO, 1970. Computer computations of cardiac output using the gamma function. Journal of Applied Physiology 28: 219-220.

Steinberg M, Marner I-L and Waever Rasmussen J, 1974. Hepatography patterns following rectal administratin of radioiodine as seen in chronic liver disease and other liver disorders. Scandinavian Journal of Gastroenterology 9: 73-79.

Stirner H, Bull U and Kleinhans E, 1986. Three-dimensional ROI-based quantification of stress/rest ^{201}Tl myocardial SPECT: presentation of method. Nuclear Medicine 25: 128-133.

Stirner H, Buell U, Kleinhans E, Bares R and Grosse W, 1988. Myocardial kinetics of ^{99}Tc^{m} hexakis-(2-methoxy-isobutyl-isonitrile) (HMIBI) in patients with coronary artery disease: a comparative study versus ^{201}Tl with SPECT. Nuclear Medicine Communications 9: 15-23.

Strauss HW, Harrison K, Langan JK, Lebowitz E and Pitt B, 1975. Thallium - 201 for myocardial imaging: relation of thallium-201 to regional myocardial perfusion. Circulation 51: 641-645.

Strauss HW and Fischman AJ, 1989. Cardiovascular nuclear medicine: the next step (editorial). Journal of Nuclear Medicine 30: 1123-1128.

Tamaki N, Mukai T, Ishii Y, Fujita T, Yamamoto K, Minato K, Yonekura Y, Tamaki S, Kambara H, Kawai C and Torizuka K, 1982. Comparitive study of thallium emission myocardial tomography with 180° and 360° and data collection. Journal of Nuclear Medicine 23: 661-666.

Tanaka E and Iinuma TA, 1970. Approaches to optimal data processing in radioisotope imaging. Physics in Medicine and Biology 15: 683-694.

Taylor DN, Garvie NW, Chir B, Harris D, Sharratt GP, Goddard BA and Ackery DM, 1980. The effect of various background protocols on the measurement of left ventricular ejection fraction in equilibrium radionulicde angiography. British Journal of Radiology 53: 205-209.

Taylor DN, Harris DNF, Condon B, Ogilvie B, Ackery DM, Fleming J and Goddard B, 1982. Radionuclide evaluation of valvular regurgitation. British Journal of Radiology 55: 204-207.

Thomas JL, Scherer J, Kahl FR, Watson N and Cowan R, 1978. Differential shunting in the diagnosis of patent ductus arteriosus with Eisenmenger physiology by radionuclide angiography. Radiology 127: 733-734.

Tobinick E, Schelbert HR, Henning H, LeWinter M, Taylor A, Ashburn WL and Karliner JS, 1978. Right ventricular ejection fraction in patients with acute anterior and inferior myocardial infarction assessed by radionuclide angiography. Circulation 57: 1078-1084.

Todd-Pokropek AE and Jarritt PH, 1982. The noise characteristics of SPECT systems. In Computed Emission Tomography (eds. Ell PJ and Holman BL) pp361-389. Oxford University Press, Oxford.

Todd-Pokropek A, 1983. Edge detection and wall motion: an intercomparison of different algorithms in nuclear cardiology. In Physical Techniques in Cardiological Imaging, pp 125-141. Adam Hilger, Bristol.

Treves S, Lange RC and Freedman GS, 1970. Study of cardiopulmonary hemodynamics using a gamma camera and a computer (abst). Journal of Nuclear Medicine 11: 369-370.

Treves S, Maltz DL and Adelstein SJ, 1974. Intracardiac shunts. In Pediatric Nuclear Medicine (eds James AE, Wagner HN and Cooke RE), pp231-246. WB Saunders, Philadelphia.

Tumeh SS, Tracy DA, Wynne J, Konstam MA, Kozlowski JF, Neumann AL and Holman BL, 1982. Scintigraphic diagnosis of tricuspid regurgitation. Radiology 145: 463-466.

Van Aswegen A, Alderson PO, Nickoloff EL, Householder DF and Wagner HN. 1982. Temporal resolution requirements for left ventricular time activity curves. Radiology 135: 165-170.

Van Dyke D, Anger HO, Sullivan RW , Vetter WR, Yano Y and Parker HG, 1972. Cardiac evaluation from radioisotope dynamics. Journal of Nuclear Medicine 13: 585-592.

Vogel RA, Kirch D, LeFree M and Steel PC, 1978. A new method of multiplanar emission tomography using a seven pinhole collimator and an Anger gamma camera. Journal of Nuclear Medicine 19: 648-654.

Wackers FJTh, Berger HJ, Johnstone DE, Goldman L, Reduto LA, Langou RA, Gottschalk A and Zaret BL, 1979. Multiple gated cardiac blood pool imaging for left ventricular ejection fraction: validation of the technique and assessment of variability. American Journal of Cardiology 43: 1159-1166.

Watson DD, Campbell NP, Read EK, Gibson RS, Teates CD and Beller GA, 1981. Spatial and temporal quantitation of plane thallium myocardial images. Journal of Nuclear Medicine 22; 577-584.

Waxman AD, Apau R and Siemsen JK, 1972. Rapid sequential liver imaging. Journal of Nuclear Medicine 13: 522-524.

Waxman AD, 1982. Scintigraphic evaluation of diffuse hepatic disease. Seminars in Nuclear Medicine 12: 75-88.

Webb S, Flower MA, Ott RJ and Leach MO, 1983. A comparison of attenuation correction methods for quantitative single photon emission computed tomography. Physics in Medicine and Biology 28: 1045-1056.

Webb S, Long AP, Ott RJ, Leach MO and Flower MA, 1985. Constrained deconvolution of SPECT liver tomograms by direct digital image restoration. Medical Physics 12: 53-58.

Weiss ES, Hoffman EJ, Phelps ME, Welch MJ, Henry PD, Ter-Pogossian MM and Sobel BE, 1976. External detection and visualization of myocardial ischemia with 11C-substrates in vitro and in vivo. Circulation Research 39: 24-32.

Weissman HS, Badia J, Sugarman LA, Kluger L, Rosenblatt R and Freeman LM, 1981. Spectrum of 99m-Tc-IDA cholescintigraphic patterns in acute cholecystitis. Radiology 138: 167-175.

Williams ED, 1985. An Introduction to Emission Computed Tomography: Report 44. The Institute of Physical Sciences in Medicine, London.

Witek JT and Spencer RP, 1985. Clinical correlation of hepatic flow studies. Journal of Nuclear Medicine 16: 71-72.

Wraight EP, Barber RW and Ritson A, 1982. Relative hepatic arterial and portal flow in liver scintigraphy. Nuclear Medicine Communications 3: 273-279.

Ziada G, Hayat N, Mohammed M, Abdel-Dayem HM, Bahar R, Salman H and Hassan I, 1986. Quantitative analysis of stress thallium-201 studies: comparison of SPET and planar imaging in the detection of CAD. Nuclear Medicine Communications 7: 427-435.